Modelling of Wireless Channels and Validation using a Scaled MM-Wave Measurement System

by

Farshid Aryanfar

A dissertation submitted in partial fulfillment
of the requirements for the degree of
Doctor of Philosophy
(Electrical Engineering)
in The University of Michigan
2005

Doctoral Committee:
Professor Kamal Sarabandi, Chair
Professor Anthony W. England
Professor Gabriel M. Rebeiz
Professor Wayne E. Stark

To the spirit of my Dad

ACKNOWLEDGEMENTS

I'd like to acknowledge for professor Kamal Sarabandi's help, courage and support in last few years as my advisor. It was a great opportunity for me to work with him. I also wish to thank professor Tony England, professor Gabriel Rebeiz, and professor Wayne Stark for honoring me by being a member of my dissertation committee and their helpful comments and suggestions.

Many thanks to professor Amir Mortazawi, Professor Dimitris Peroulis, Brett Lyons, Luke Lee, Dr. Adib Nashashibi, Dr. Yongshik Lee and Kevin Buell who helped me on this research and other RADLAB members for their friendship.

My best wishes and appreciations to my mother and the spirit of my father who were supportive in this long journey of education. At last but not least I'd like to thank my wife for her patient in last four years and her efforts for keeping up with me in all up and downs.

TABLE OF CONTENTS

LIST OF TABLES

Table

LIST OF FIGURES

Figure

LIST OF APPENDICES

Appendix

CHAPTER 1

Introduction

1.1 Motivation

Wireless systems have become prevalent for a wide range of commercial and military applications. The third generation (3G) of wireless communications is currently being developed and will reach full development by 2005. The 3G systems will provide multimedia services and satisfy the desired “anytime and anywhere” requirement [1]. The 4G systems which are currently being discussed [2] will provide an all-IP network that integrates several services available at present and provides new ones, including broadcast, cellular, cordless, wireless local area network (WLAN), and short-range communication systems. In future defense systems, the integration and interdependent operation of military ground, surface, air, missile, and space-based radar and communication systems for enhanced overall defense effectiveness will be very critical. Instead of autonomous platforms, future collector systems, processors, and users will share information via networks. During operations, the engagement systems will have the ability to reach back for information that will enable them to provide more adaptable quick-reaction forward “footprints” (presence). Ground forces will also contribute to the total situation awareness with improved communications and sensor systems. Soldiers’ positions will be known accurately via global positioning system (GPS) satellite receivers, and they will be able to access secure spread-spectrum cellular-like systems with voice and data links. Data from night-vision, spectrum-scanning, and video sensors will be linked back to headquarters over cellular systems or directly to satellites. Throughout the entire system configuration, many images per second will be collected, processed, and the information shared in real time. In addition to improved radar and communication capabilities, this environment will demand significantly increased signal and information processing capabilities [3]. Hence the general trend in the development of future wireless communication is the use of higher data rates (broader frequency band) and propagation in more complex environments.

One of the most critical aspects in designing a wireless system is the accurate characterization of the propagation channel. Accurate channel modelling in wireless communication allows for: 1) improved system performance (bit error rate, battery life, etc.), 2) reduced interference, to ensure proper operation of other commercial systems and provide secure communication for military purposes.

Numerous methods and techniques have been developed to predict the effect of the channel, and these can be divided to two categories: 1) Statistical or empirical models like Okumara [4], Hata [5] and Longley-Rice [6], and 2) Deterministic or analytical models like ray-tracing based models [7–12]. Statistical models are based on measured data. Therefore to develop these models, many measurement data sets are required. A draw-back of these empirical models is that they are only applicable to environments which have similar geometry to the measurement bases. Therefore to build a general and accurate model an exorbitantly large number of measurement sets are required.

Deterministic methods are based on the physics of the environment and wave propagation phenomena such as reflection, transmission, and diffraction. These methods are generally applicable to any arbitrary environment especially especially useful for micro- and pico-cellular environments where statistical models fail. In these cases the wave propagation phenomena is highly the site specific. One major task in the development of deterministic models is to verify the accuracy of the predicted results. This can be done by careful measurements where besides the signal parameters, all physical details of the environment are determined and ported to the simulator. In addition, dielectric properties of the actual materials and their spatial variations must be measured and considered in the model, where is practically very difficult if not impossible.

An alternate approach to the time consuming and expensive outdoor measurements is the proposed scaled measurement system in this thesis. This allows accurate measurement of well defined channels under a controlled laboratory environment. A millimeter-wave scaled propagation measurement system (SPMS) is designed for this purpose. Confining the desired range of frequency to systems operating at UHF to L-Band (0.5-2 GHz), dimensions of scatterers and terrain features in the scaled propagation channel can be reduced by a factor of 50-200 for the proposed SPMS that operates at around 100 GHz. This reduction brings the size of building from few meters to few centimeters so a scaled model of city block can easily fit in a laboratory, and measurements can be done quickly, accurately, and cost effectively.

1.2 Background

In this section, first wireless channel models are reviewed. Then importance of propagation measurement for developing or verifying of channel models and difficulties involved in that are described. As W-band transceivers are major subsystems of the Scaled Model Propagation System (SMPS), the second part of this chapter briefly introduces most recent reported researches on W-band circuit modules and systems.

1.2.1 Wireless Channel Modelling

Developing propagation models for urban environment started as early as four decades ago. These models were developed for VHF and UHF broadcasting, based on measured data and few simple corrections factor such as frequency, antennas height and gain. Those models were able to provide a rough estimation about coverage or path-loss, which was sufficient at that time because any inaccuracy in coverage estimation were compensated by increasing transmitting power without a significant cost increase in the broadcasting system. Growth of wireless communication made electromagnetic (EM) spectrum more crowded and consequently more restricted spectrum regulation has been imposed by the standard organization such as Federal Communications Commission (FCC). While these standards ask for lower power transmission to minimize interference among systems, new applications with higher bandwidth need higher signal to noise ratio (S/N) to provide adequate bit error rate (BER). Hence every part of the wireless system needs to be optimized at extreme levels including the channel.

In 1990's theoretical and numerical channel models were proposed and still expanding in order to accomplish channel modelling with higher accuracy and more details such as delay spread, coherence bandwidth, and Doppler spread which are crucial for new digital and mobile systems. Fortunately, at the same time new computers with faster computational speed have become available and helped developing these channel models. The theoretical models can be divided into two categories: 1) Physics-based models, and 2) Statistical models. Although physics-based models are more accurate and take the environment details into account, their usage is still limited to micro- and pico-cellular scenarios which statistical models cannot provide useful estimation. The main causes of this are difficulties in importing the physical environment data, such as geometry, topography, and material properties, and also lack of model verification by measurements. Hence communication scientists still rely on statistical models which are developed based on measured data. In what follows these two categories of channel models are briefly introduced and at the end difficulties and errors involved in channel measurement which is required for both models are reviewed.

Measurement-based Statistical Models

Measurement-based models are developed based on extraction of statistical behavior of channel from extensive measurements data. Okumura model [4] is one of the first empirical channel models. This model can predicts path-loss only and takes into account some of the propagation parameters such as the type of environment and the terrain irregularity. These parameters are added to mean path-loss value which is found by few looking up curves. The measurement based models have become more accurate and complicated by incorporating environment details as much as possible [5,13] and it also has been tried to use these models for indoor scenarios [14]. As mentioned earlier in order to develop an accurate statistical model a comprehensive measurement data is required, which is certainly time consuming and costly.

Site-Specific Models

Site-specific models are built up by considering the environment details, wave propagation phenomena such as reflection and diffraction, and finding signal paths between transmitter and receiver. Primary models in this category were based on simplistic situations and finding few paths such as direct, ground reflection, and rooftop diffraction [15]. Later with the advancement of computer capabilities, more complex channel simulators were developed based on ray-tracing or image algorithms [7–12]. These models seems to be the best candidates for providing all channel information required in optimizing the next generation of communication systems. However the difficulties in importing environment details to these simulators, lack of model verification by field measurements are the weak points of these models that must be overcome.

Model Verification by Field Measurement

As described in last two subsections, field measurements is important either for developing channel models or verifying simulated result of a channel model. However outdoor measurements are expensive and time consuming [16,17]. Also there are many factors such as traffic (cars, pedestrian, ...) which are not under control and affect the measurements. Furthermore for site-specific models the discrepancies between the measurement site and data used in simulation one can be significant, hence the verification process will end up with large margins of error.

1.2.2 W-Band Transceivers Background

The SPMS operation frequency is chosen around 100 GHz which gives maximum scaling ratio while transceivers' circuits can be fully characterized using available lab equipments. It will be described later that the SPMS works similar to standard millimeter-wave (mm-wave) S_{21} measurement setup. This means vector network analyzer (VNA) signal will be up- and down-converted to desired operation signal using two mm-wave modules. However for a propagation measurement system, receiver and transmitter probes are mobile, consequently it is not possible to use available mm-wave modules. Moreover, the probes' size has to be small in comparison with scaled buildings to minimize its interaction in the measurement environment. Hence design and fabrication of special receiver and transmitter probes is required. As construction of W-band probes is a major part of this thesis, in this section a brief background of recent mm-wave circuit components and systems are presented.

Subharmonic Mixers

High power signal generation at mm-wave frequencies is very difficult, so a major concern in mm-wave systems is loss reduction specially at frequency conversions which are one of the most lossy part of a system. Hence mixers are one of the challenging components in mm-wave systems. An alternative to direct conversion technique is using subharmonic mixers. The subharmonic mixers are often used because it is easier and less expensive to generate a high power, and low phase noise source at a subharmonic of required local

Table 1.1: MM-wave subharmonic mixers performance comparison

RF Freq.(GHz)	LO Freq.(GHz)	Features, Pub.	Ave. Conv. Loss(dB)
84-102	45	W.G.P[1], [19]	11
92-96	45	Flip Chip, [20]	10
92-94	45	Flip Chip, [21]	8
112-120	62	MMIC[2], [22]	16
230-240	120	MMIC, W.G.P, [23]	9.5
175-182	96	MMIC, W.G.P, [24]	16
154-170	77	Flip Chip, [25]	13
75-77	15.1	Flip Chip, [26]	23
80-110	48	MMIC, [27]	12

[1]Waveguide Package, [2]Monolithic Microwave Integrated Circuit

frequency.

Furthermore in order to have a coherent transceiver system common LO source must be used for both transmitter and receiver, this means LO signal must be carried in a long path from its source to the mobile receiver. Clearly, carrying lower frequency signal (K-band) in flexible coax cables can be done much easier than carrying a W-band signal through waveguides.

The diode based subharmonic mixers are a major category of these mixers. Antiparallel diode pair is a popular choice for subharmonic mixers becasue it creates a symmetrical *V*-*I* characteristic that suppresses the fundamental mixing product of the RF (or IF) and LO signals and leads to a better conversion loss [18]. Comparison between some of the reported results of mm-wave subharmonic mixers are shown in table 1.1.

Filters

Subharmonic mixers generate undesired harmonics as well as desired one because of their nonlinear nature. Hence for a transceiver system it is very important to weaken undesired spurious by filtering to have a single tone communication link. Also appropriate filtering at LO and IF ports of a mixer increase its efficiency. In this section a brief history of planar mm-wave filters are reviewed. As coplanar waveguide (CPW) is the optimum choice in terms of electromagnetic properties at mm-wave and simple fabrication most reviewed papers in this section are CPW based filters.

Although microwave filters have been studied extensively but there are not many articles about planar mm-wave filters, specially at W-band. There are few difficulties involved in filter design and fabrication at mm-wave and above. Most parasitic elements, that are usually ignored at lower frequencies design procedure, have significant effect at mm-wave frequencies. The parasitic elements and their effects cannot be considered as design parameters. Hence these effects have to be accurately modelled and compensated. Alternatively use of structures with minimal parasitic effects should be considered. CPW line discontinuities are well characterized at microwave frequencies [28–30] and are studied at higher frequencies up to 50 GHz [31–33]. However modelling and characterization of such discontinuities at W-band frequencies is rather sparse and incomprehensive. Calibration accuracy at W-band is one of the major difficulties for characterization parasitic capacitance and inductors which are as small as few fF's and pH's respectively.

Table 1.2 shows important parameters for few filters in some of the recent reported studies [34–38]. It should be noted fabrication process for all of these filters are not similar consequently it is not possible to compare their performance clearly.

W-Band Systems

W-band systems are mainly designed for radar applications [39–41]. These radar or transceiver MMIC's are fabricated in the state of the art labs such as TRW [40] with 0.1 μm fabrication technology which is not commercially available. In this thesis, design is done using flip-chip elements in order to reduce fabrication cost and make it feasible using the University of Michigan clean room facilities.

Table 1.2: Planar microwave filters performance comparison

F_0 (GHz)	BW (%)	I.L. (dB)	Order	Rej.@ $F_0 \pm$BW (dB)	Pub.
10	20	2.2	3	–	[35]
10	10	3.4	3	–	[35]
10	5	5.4	3	–	[35]
20	35	2.2	3	22	[34]
30	53	2.5	3	13	[36]
65	22	1.5	3	13	[38]
83	36	1.8	3	17	[38]
92	5	4.2	3	–	[38]
95	6.1	3.4	5	42	[37]
95	12.5	2.2	5	33	[37]
95	17.7	1.4	3	22	[37]

1.3 Thesis Framework

Figure 1.1 shows the main components of the W-band SPMS. The system includes an x-y-z probe positioner, scaled model of a city block, miniaturized W-band transmitter and receiver probes, and a vector network analyzer. The network analyzer in the SPMS is used for signal processing and data acquisition. Therefore the setup is configured to characterize the propagation channel in a manner similar to the standard S_{21} measurement. The network analyzer allows for coherent and broadband path loss measurement with a wide dynamic range. Also the time domain features of the network analyzer allow for measuring the power delay profile which makes the SPMS unique in channel modelling. In order to move the receiver probe with the required accuracy (to within a fraction of the wavelength $\cong$ 3 mm) for measuring fast fading and slow fading statistics, a computer-controlled xy-table has been designed and built. As the operating frequency of the network analyzer (L-band) is different from the required SPMS frequency (W-band), an up- and down-converter has been designed and fabricated as part of the transmitter and receiver probes respectively. To minimize the interaction of the probes with their environment, they must be designed as

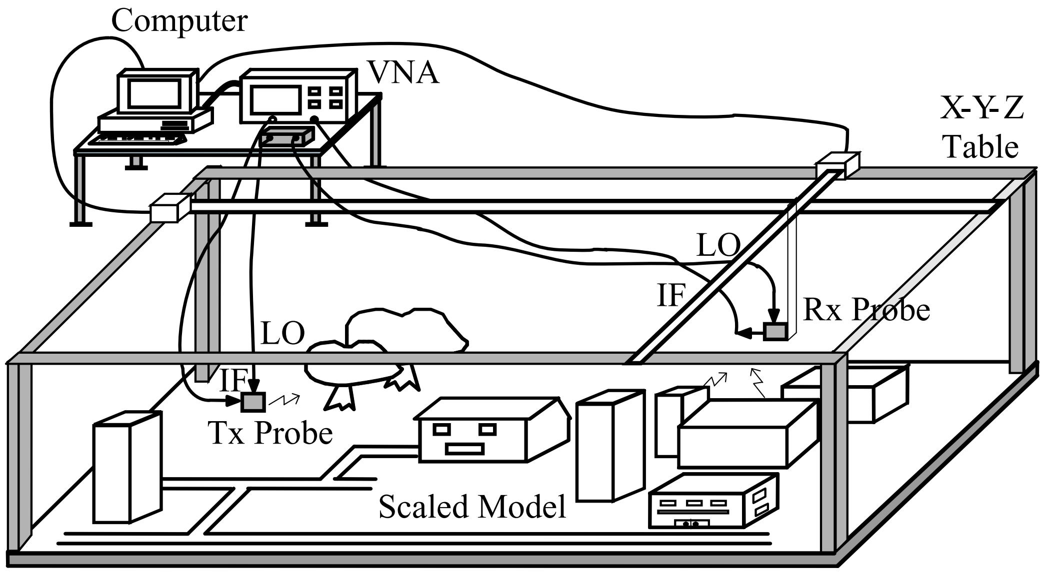

Figure 1.1: Scaled propagation measurement system block diagrams.

small as possible.

The design, fabrication, and performance of individual circuit elements of SPMS will be demonstrated in chapter 2. Construction of scaled buildings and different techniques used for characterization of building's material are described in chapter 3. XY table, which is an automatic positioner for receiver probe, and its specifications are also explained in this chapter. The system calibration and overall system specifications are presented in chapter 4. Chapter 5 explains a physics based site specific channel model using 3D ray-tracing with few examples for indoor, outdoor and suburban areas. Chapter 6 demonstrates few sample measurements of path-loss, coverage and power delay profile (PDP) and is also on model verification by comparison between theory and measurement. Finally the conclusion of this study and its applications and future work are introduced in last chapter (chapter 7).

Figures 1.2 and 1.3 show the thesis flowchart and percentage of each tasks and sub-tasks respectively.

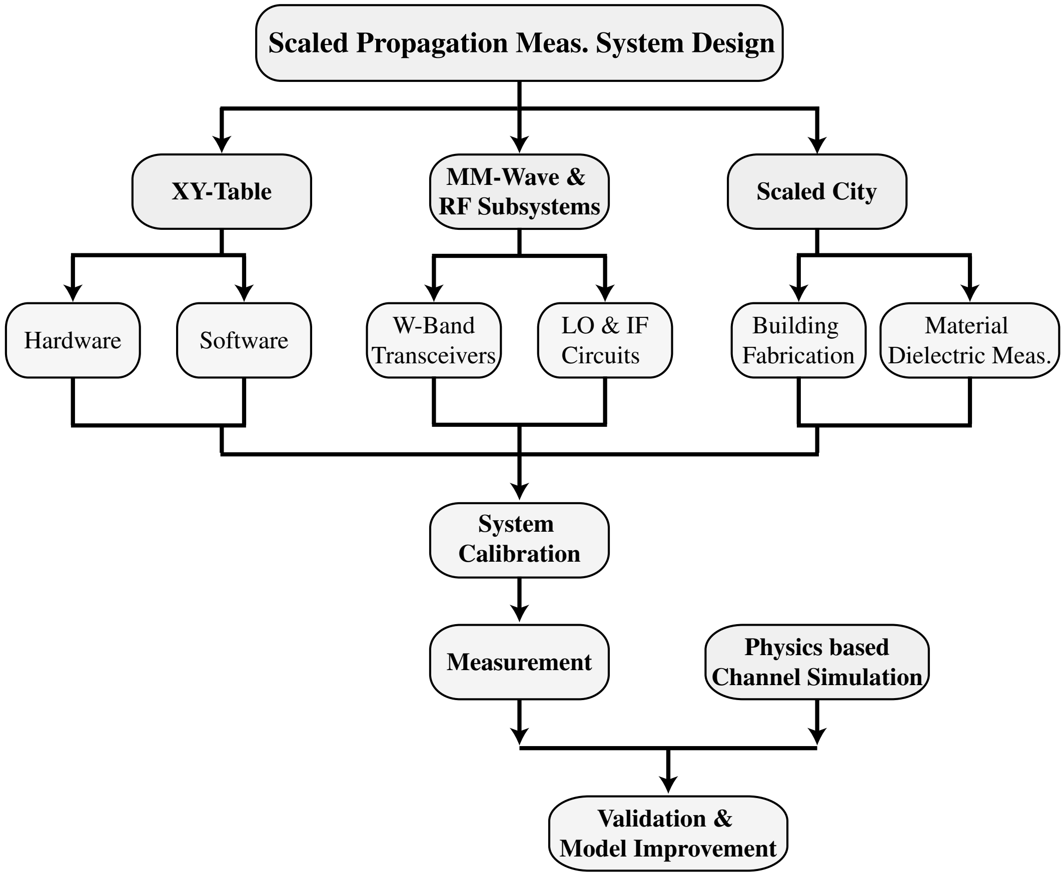

Figure 1.2: Thesis flowchart.

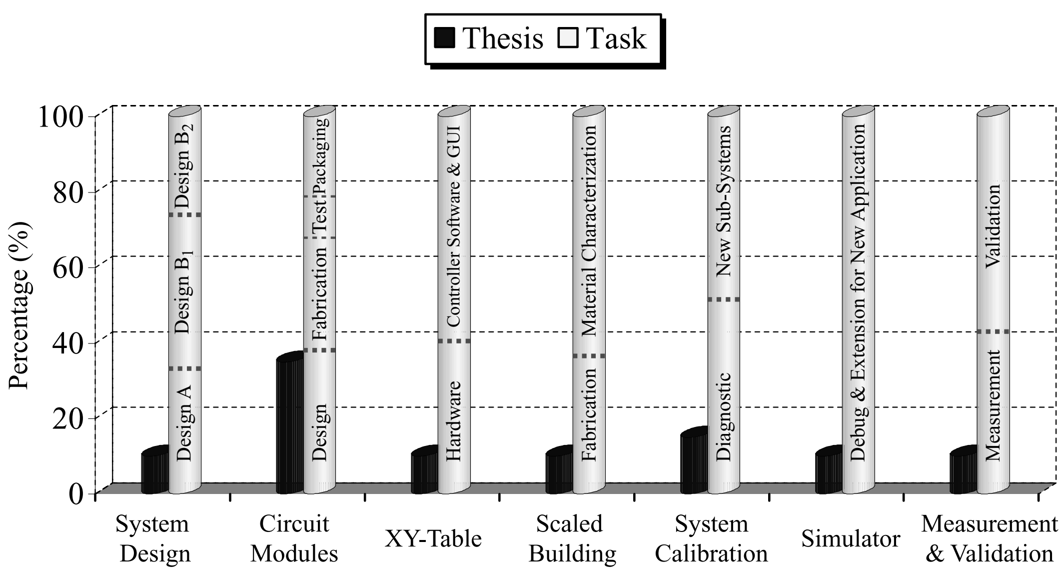

Figure 1.3: Thesis tasks and sub-tasks.

CHAPTER 2

Circuit Components

In this chapter design, fabrication, and performance of individual circuit elements in the scaled propagation measurement system (SPMS) will be demonstrated. First part of the chapter describes W-band transceiver probes and their sub-circuits and second part of the chapter is on extra circuit modules designed for IF and LO signals and overall system performance improvement.

In the SPMS a stepped-frequency vector network analyzer (VNA) is used as the base for coherent transceiver proposed system. As it is shown in Figure 2.1, the signal from the VNA is up and down converted between the W- and L-bands by the transmitter and receiver probes. Same LO source is used for transmitter and receiver probes which not only allows for coherent measurement of the fields but also for measurement of very weak signals by reduction of the network analyzer's IF bandwidth to its minimum value (10 Hz for HP8720D). Narrow IF bandwidth reduces the noise level and permits measuring signals at very low power levels (around -110 dBm for HP8720D). To maintain the high fidelity of the VNA signal The local signal source in the SPMS is generated by a dielectric resonator oscillator that has a frequency variation of 6 kHz/^{0}C and a phase noise of -86 dBc/Hz at 10 kHz offset from the center frequency. The common LO operates at 23.7 GHz and drives the subharmonic mixers in transmitter and receiver probes through a set of high quality flexible coaxial cables.

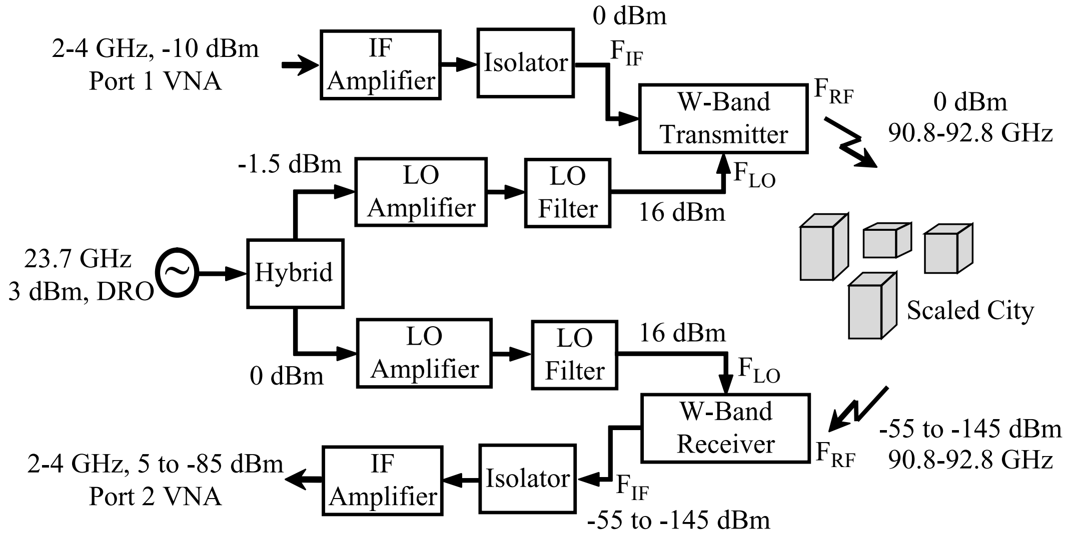

Figure 2.1: SMPS circuit components diagram.

The VNA used in the SPMS (HP8720D) can provide up to 5 dBm of output power, however the harmonics level at maximum output power are relatively high and adversely affect the quality of the overall measurement. Hence the VNA output power is set at -10 dBm and an IF amplifier is used to produce sufficient power at the IF port of the transmitter probe. Isolators are placed in order to improve matching and prevent signal ringing in the cables. The LO amplifiers are narrow-band and have significant rejection at IF band. In addition narrow-band filters are designed and placed at the LO ports to increase the isolation between the IF ports of the transmitter and receiver probes. This prevents the IF signal leakage through direct path between the transmit and receive ports of the VNA.

The simulation results in the following sections were performed by ADS Momentum for the passive elements, and a harmonic balance simulator for nonlinear analysis of the subharmonic mixer. The measurement were realized using a probe station (for on wafer measurements), HP-8510C network analyzer, HP-W85104A mm-wave test setup, HP-8562A spectrum analyzer, and HP-11970W waveguide harmonic mixer.

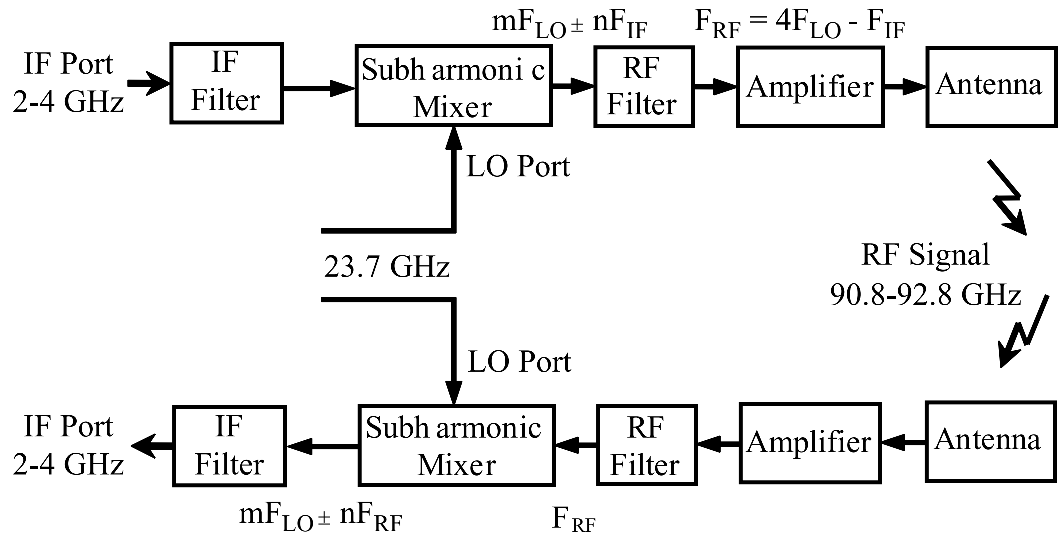

Figure 2.2: W-band transmitter and receiver probes block diagrams.

2.1 W-Band Transceivers Probes

Figure 2.2 shows the block diagrams of the transmitter and receiver probes. As shown in the upper branch, the IF signal (F_{IF}) from the output of the network analyzer is mixed with the local oscillator signal (F_{LO}) in a subharmonic mixer to generate the transmitter signal. This signal contains all harmonics of the form $mF_{LO} \pm nF_{IF}$. The desired harmonic, which results from mixing the 4^{th} harmonic of the LO signal and the IF signal, is selected by the RF filter for transmission. Then it is amplified and transmitted. At the receiver (lower branch in Figure 2.2), the RF signal captured by the antenna is amplified before down-conversion at the receiver subharmonic mixer. Then the desired IF signal ($4F_{LO} - F_{RF}$) is selected by the IF filter and delivered to port 2 of the network analyzer after IF amplification (not shown). Subharmonic mixers are used to allow for stepped frequency operation without need for distributing a common W-band local oscillator to mobile transmitter and receiver probes, which is practically impossible. The transceiver circuit was fabricated on a 10 mils ($\cong 250\mu$m) thick quartz wafer. As the width of a 50 Ω microstrip line on available substrates becomes comparable with the wavelength at W-band frequencies, microstrip lines become inappropriate for circuit design. Also to be compatible with the test setup,

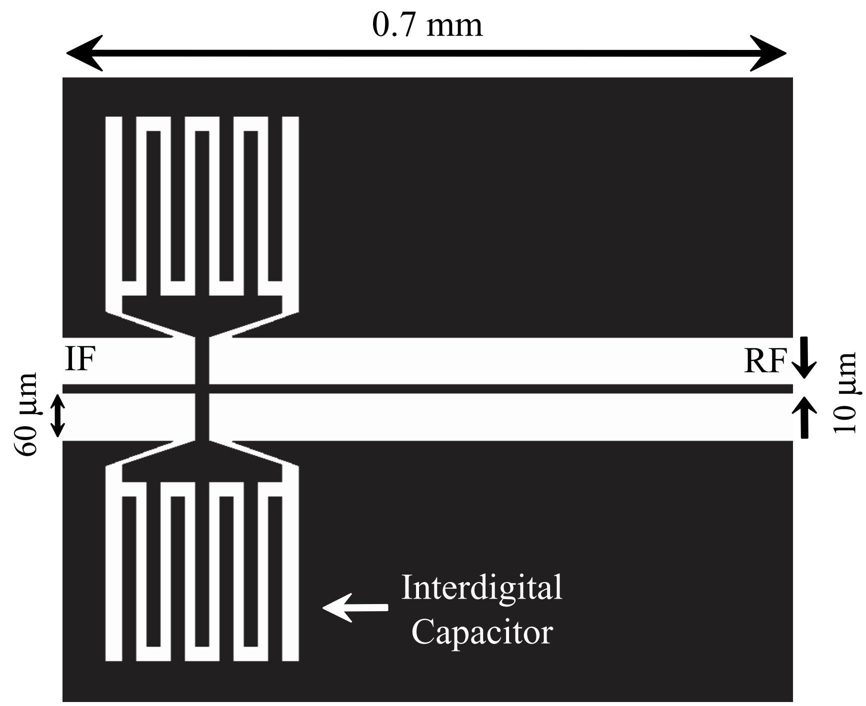

Figure 2.3: IF filter layout and dimensions.

the circuit was designed and fabricated using CPW lines. The fabrication processes were performed in the University of Michigan's clean room, using the wet-etching technique on 3 μm electroplated gold on the quartz wafer. The skin depth for the RF, LO, and IF frequencies are 0.26, 0.52, and 1.5 μm respectively. The gold thickness is marginally sufficient for the IF signal, but as it will be shown, the minimum feature size in the circuits is 10 μm, which limits the thickness of the plated gold that can be used. Fortunately insufficient metal thickness does not degrade the circuit performance because in this miniaturized circuit the IF signal path on the circuit is just 2.5 mm which is smaller than $0.01\lambda_g^{IF}$. Therefore the associated metallic loss is negligible.

2.1.1 IF Filter

The IF filter is placed to isolate the IF and RF signals in order to improve the sub-harmonic mixer's efficiency. There are many topologies that can be used for this filter. However to minimize the size, a low pass filter constructed from a quarter wavelength high

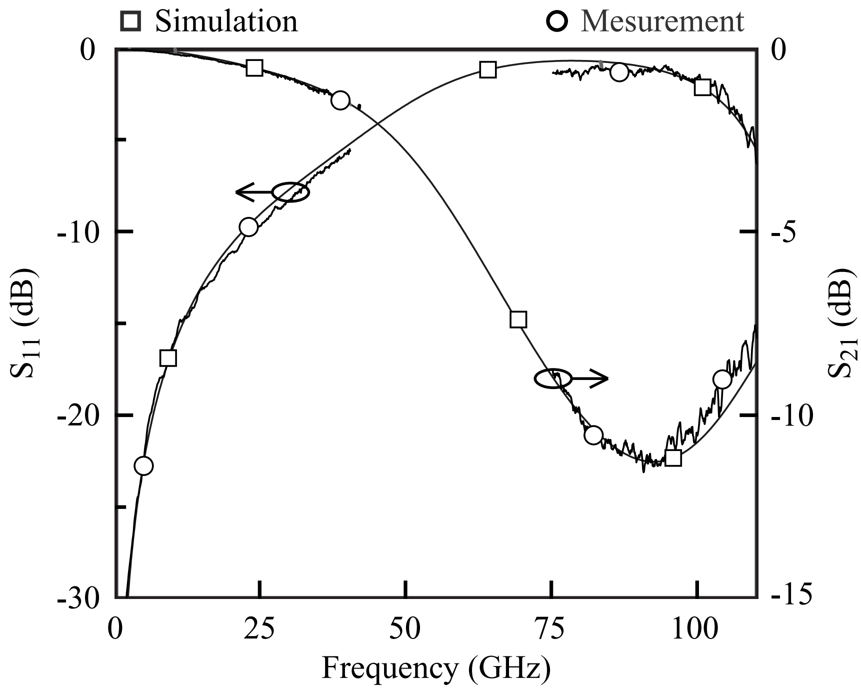

Figure 2.4: Simulation and measurement results for IF filter.

impedance line terminated by an inter-digital capacitor is used. For this simple filter the higher is the capacitance and the line impedance, the lower is the RF signal leakage to the IF port. Hence the aim is to increase the capacitance and the line impedance as much as possible. However these two parameters are limited by the minimum achievable feature size in the fabrication process, which is about 10 μm. Figure 2.3 shows the IF filter layout. For the specified dimensions in this figure, a line impedance of 145Ω and an interdigital capacitance of 75 fF with a quality factor of 10 at the W-band are achieved. The MoM simulation and the measured transmission coefficient and return loss for the IF filter are plotted in Figure 2.4, where excellent agreement is shown. There are no measured data between 40-75 GHz. The maximum insertion loss of this filter at the IF signal is less than 0.1 dB, and its return loss is less than -24 dB over the desired IF frequency range. The isolation between the RF and IF signals is more than 12 dB.

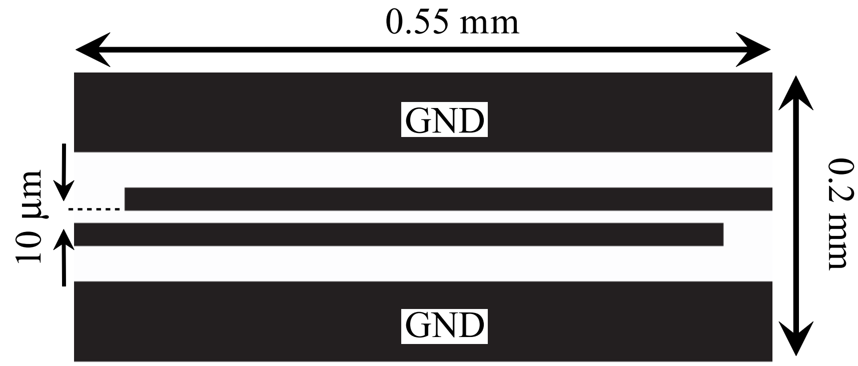

Figure 2.5: CPW coupled line for the first stage of RF filter.

2.1.2 RF Filter

The RF filter is intended for selecting the desired harmonic of the mixed IF and LO signals ($4F_{LO} - F_{IF}$) generated by the subharmonic mixer. It also prevents IF signal leakage to the RF port which improves the conversion loss of the subharmonic mixer used for up- and down-conversion. However, in the transmitter probe, in addition to RF-IF isolation, this filter should reject strong and undesired harmonics like the third and fifth harmonics of the local oscillator to keep the RF amplifier from saturation. Furthermore, for single tone transmission upper side band (USB) of up-converted IF signal ($4F_{LO} + F_{IF}$) also has to be attenuated sufficiently. In order to achieve all of the above mentioned features, the RF filter is made of two cascaded band pass filters.

First Stage

A CPW coupled line filter shown in Figure 2.5 is selected as the first stage of the RF filter. The advantages of this filter are high isolation between the RF and IF signal, low insertion loss at the RF frequency range, compact size, and high impedance at the IF frequency. Figure 2.6 shows the simulated and measured S_{11} and S_{21} of this filter as a function of frequency. As can be seen, this filter provides more than 50 dB of IF to RF isolation and has an insertion loss of less than 0.5 dB and a return loss of less than -25 dB at the RF frequency range.

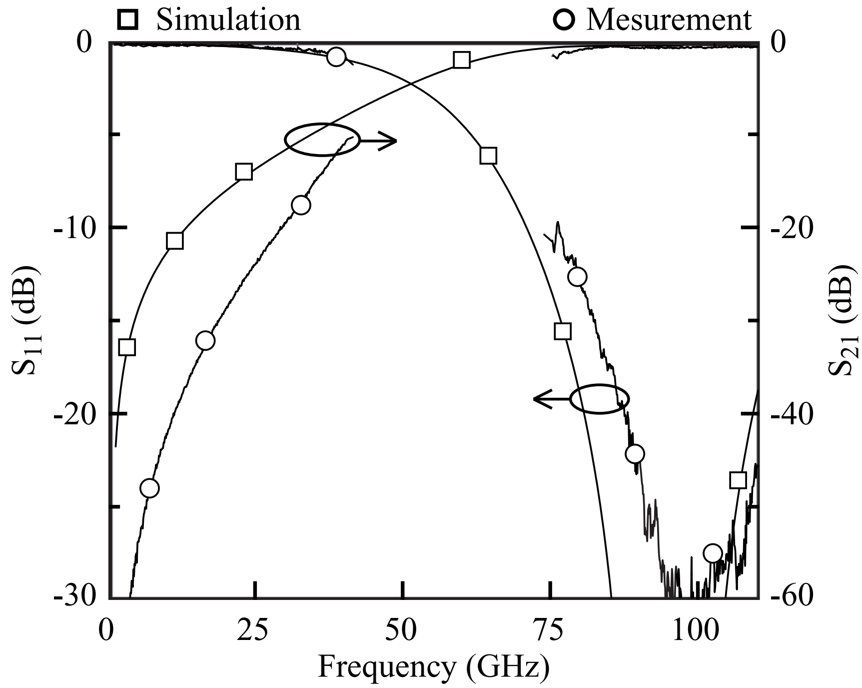

Figure 2.6: Simulation and measurement results for the CPW coupled line filter.

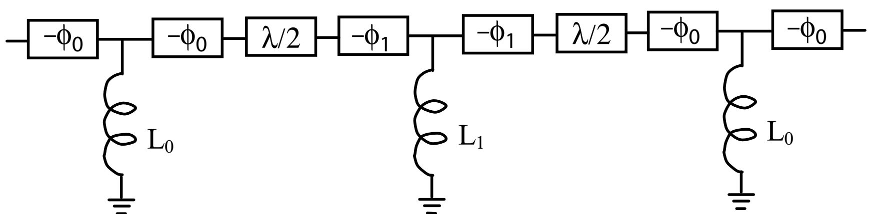

Figure 2.7: Circuit model of inductive coupled resonator filter for second stage of RF filter.

Second Stage

In order to generate a spurious free RF signal and also prevent saturation of the RF amplifier by the undesired strong LO harmonics ($3F_{LO}$ at 71.1 GHz and $5F_{LO}$ at 118.5 GHz), created by the subharmonic mixer, a second stage of RF filter is designed. The second stage is constructed from two section inductively coupled resonators [42,43], whose circuit model and topology are, respectively, shown in Figure 2.7 and 2.9. The inductive coupling between the resonators is achieved by symmetric short circuited CPW line stubs as shown in Figure 2.8(a). A simple method to calculate the inductance of these stubs is the classical formula for ribbon inductors [42].

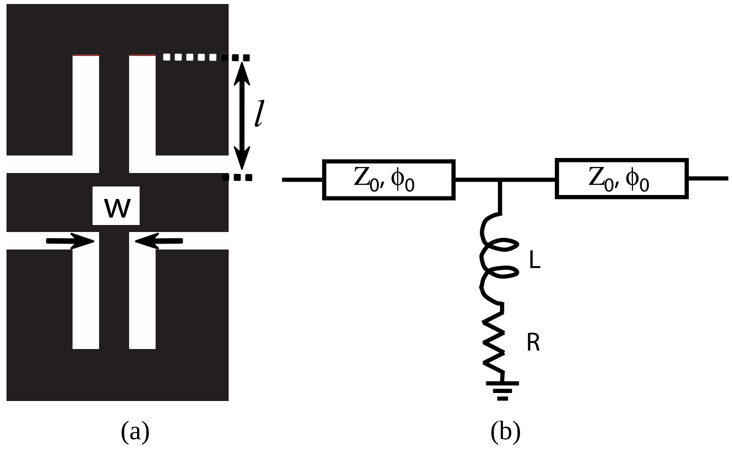

Figure 2.8: Characterization of effective inductance and resistance for short stubs in CPW line; (a) Inductor layout, (b) Circuit model.

Table 2.1: Effective Inductance of Short Stubs in CPW Line

Inductor#	*w(μm)*	*l(μm)*	MoM (pH)	Eq. 2.1 (pH)
1	60	20	5.1	1.4
2	30	20	7.1	1.8
3	30	136	21.1	32.9
4	30	198	25.0	54.9
5	25	213	33.0	64.3

$$L = 2l\{\ln(2\pi l/w) - 1 + w/\pi l\} \quad nH \tag{2.1}$$

where *w* and *l* (in cm), are the width and length of the inductor, respectively. However, the accuracy of this formula is quite poor with errors often greater than 100%. Therefore to extract an accurate effective inductance of these short stubs, the MoM simulated S-parameters of the stubs, shown in Figure 2.8(a), are compared with its circuit model, shown in Figure 2.8(b). Table 2.1 shows the calculated inductances using (2.1) and the extracted values from the MoM simulation. The MoM results are used in the final design, and as will be shown, they lead to excellent agreement between the measured and simulated filter responses. In order to provide the required out-of-band rejection and minimum insertion loss simultaneously, a 2-pole filter is found to be the optimum choice. The design of this

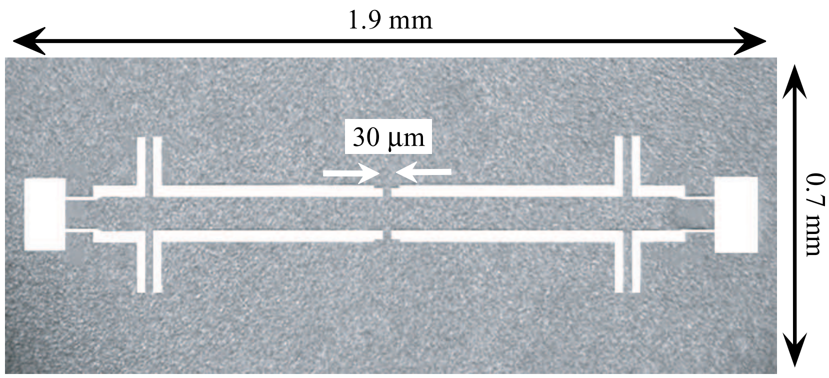

Figure 2.9: Photograph of fabricated inductive coupled resonator filter on Quartz wafer.

filter began with the corresponding lowpass element values, $g_0 \ldots g_n$. Then using (2.2, 2.3, and 2.4), $L_j(X_j/\omega_0)$ and ϕ_j are calculated [42].

$$Z_0/X_j = \begin{cases} (\frac{Z_0}{S})^{1/2} - (\frac{S}{Z_0})^{1/2} & j = 1, n+1 \\ \frac{Z_0\sqrt{g_{j-1}g_j}}{S \quad g_0 g_1} - \frac{S \quad g_0 g_1}{Z_0\sqrt{g_{j-1}g_j}} & j = 2, 3, \ldots, n \end{cases} \tag{2.2}$$

$$S = \frac{\pi Z_T}{2g_o g_1}\frac{\omega_2 - \omega_1}{\omega_0} \tag{2.3}$$

$$\phi_j = \tan^{-1}\frac{2X_j}{Z_0} \tag{2.4}$$

where Z_T and Z_0 are the characteristic impedance of the CPW line and port impedances respectively. In this design both are chosen to be 50 Ω. In (3) ω_0, ω_1, and ω_2 are the center, lower cut-off, and higher cut-off angular frequencies. A photograph of the fabricated filter is shown in Figure 2.9. Figure 2.10 shows the simulated and measured filter responses. Magnetic current concept is used in the MoM simulation for fast computation and more accurate excitation of CPW structures. As such, conductive loss is not modelled. This effect was considered in simulation by extracting inductors and CPW line parameters from measured results and used in the simulations. Figure 2.10 shows filter rejection at $3F_{LO}$ and $5F_{LO}$ to be more than 35 dB. Also the closest undesired harmonic to the RF signal, which is the upper side-band of the up-converted IF signal ($4F_{LO} + F_{IF}$ = 96.8-98.8 GHz),

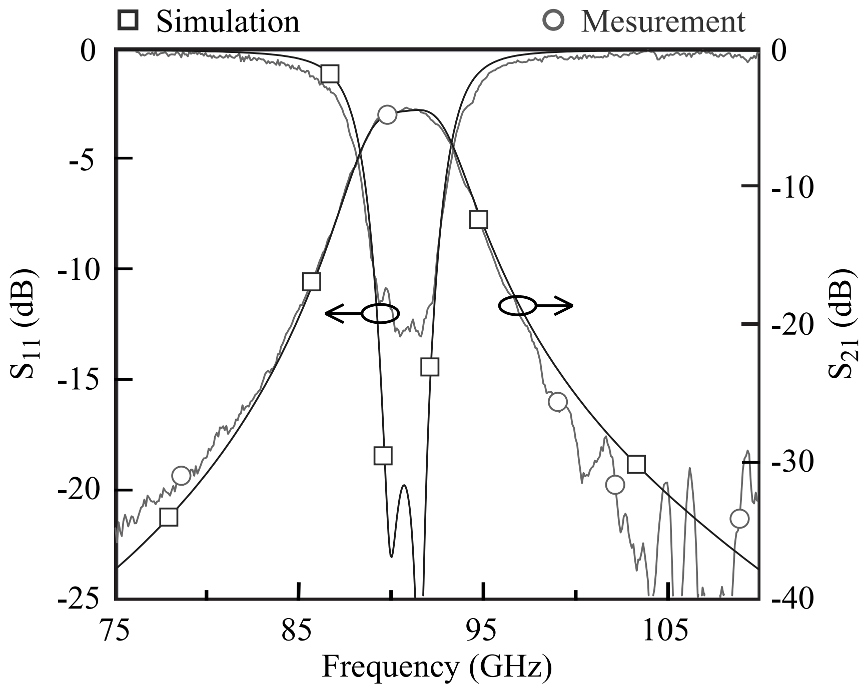

Figure 2.10: Simulation and measurement results for the inductive coupled resonator filter.

is at least 30 dB attenuated through two such filters at the transmitter and receiver probes totally. This ensures that the SPMS is able to measure fading depth at least as low as 30 dB. In extension of filter design, using shunt inductive stubs introduced in this section and interdigital capacitors a novel bandpass filter and a miniaturized highpass filter were designed and fabricated. Details are presented in appendix B.

2.1.3 Subharmonic Mixer

The conversion loss and noise performance of a millimeter-wave mixer usually is limited by insufficient LO power or by excessive LO noise [44]. Generally mixers are pumped at half or a quarter of the required LO frequency. The major disadvantage of this technique is a higher conversion loss compared to fundamental mixers. Considering the transmitter probe's block diagrams, the extra conversion loss of the subharmonic mixer is tolerable as long as the up-converted signal power reaches to the minimum input power to achieve maximum, distortion free, output power of the RF amplifier, which in this case is -24 dBm.

Table 2.2: GaAs Schottky Diodes Characteristics

	R_s (Ω)	R_j (Ω)	C_{jo} (fF)	C_T (fF)	V_F (V)	V_{BR} (V)
MACOM	4	2.6	20	45	0.7	7.0
Alpha	7	4	35	55	0.7	3.0

An antiparallel diode pair is a common choice for subharmonic mixers. The reason is the symmetrical V-I characteristic of the antiparallel diodes that suppresses the fundamental and even harmonics mixing product of the LO and RF (or IF) signal. It should be noted that proper operation of the subharmonic mixer depends on the similarity of the two back-to-back diodes. In our design we have used a GaAs flip chip schottky antiparallel diode pair manufactured by MACOM and Alpha Industries Inc. The specifications of these diodes are given in Table 2.2. In order to improve the conversion loss of the mixer, the mixing product near the second harmonic of the LO signal must be reactively terminated. Therefore, two quarter-wavelength open stubs centered at $F_0 = F_{RF} - 2F_{LO}$ are placed at both sides of the antiparallel diodes to suppress the associated harmonics with the second harmonic of the LO signal. As mentioned earlier, the RF and IF filters prevent IF and RF signal leakage to the RF and IF ports respectively. A quarter-wavelength short stub at the LO frequency, which acts as an open circuit for the LO signal and a short circuit for the IF and RF ($F_{RF} \cong 4F_{LO}$) signals, is also placed at the LO side of the subharmonic mixer to block IF and RF signals leakage to the LO port. The subharmonic mixer circuit is optimized for the best conversion loss, large signal matching at all ports, and minimum size. Figure 2.11 shows the subharmonic mixer layout with the IF and the first stage of the RF filters. Wire bonds are placed at all discontinuities to suppress undesired slot modes on the CPW line. The simulation and measured output RF power of the up-converter and conversion loss are shown in Figures 2.12 and 2.13 respectively. As can be seen, the maximum up-converted signal power is sufficient to provide the RF amplifier with the required input power for maximum output. The maximum spurious level of the RF signal in the SMPS is shown in Figure 2.14, where it is shown that the average maximum spurious level is -40dBc. This

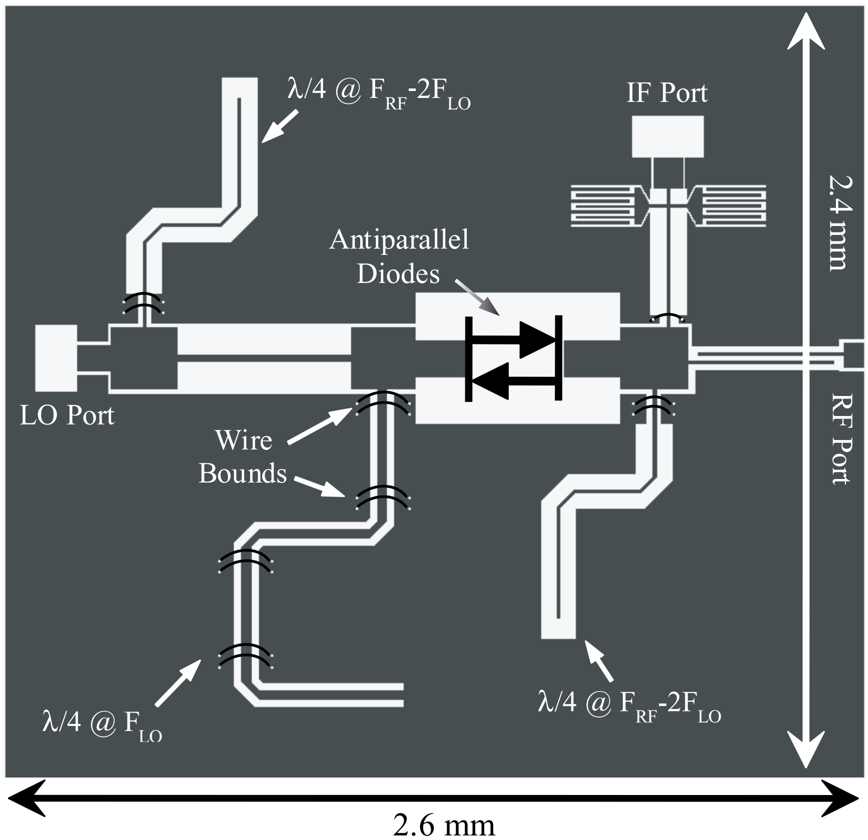

Figure 2.11: Subharmonic mixer layout with IF and part of RF filters.

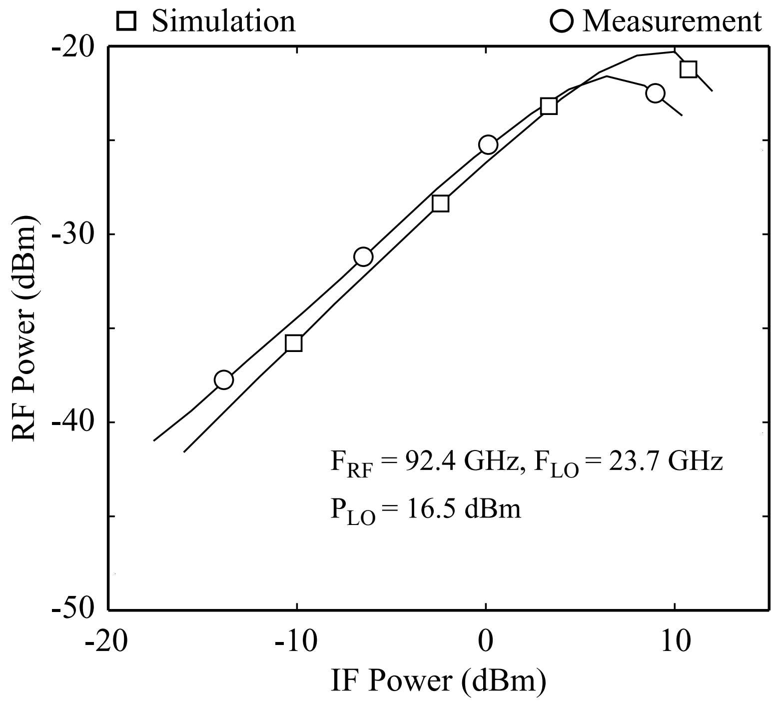

Figure 2.12: Simulated and measured RF power at the up-converter output.

allows for measurement of fading depths as low as 40 dB. The down-converter used in the receiver probe has the same topology as the up-converted with similar performance characteristics.

2.1.4 RF Amplifier

In order to compensate for the conversion losses of the up- and down-converter a W-band amplifier is used in each probe. The amplifier chip is mounted on the circuit using silver-epoxy. As shown in Figure 2.15 the input and output of the chip and DC contacts are connected to the circuit using gold wire bonds. In the desired RF frequency range the amplifier has a gain of 27-29 dB and a noise figure of 4 dB. Figure 2.16 shows the amplifier gain, noise figure, and its input and output return losses.

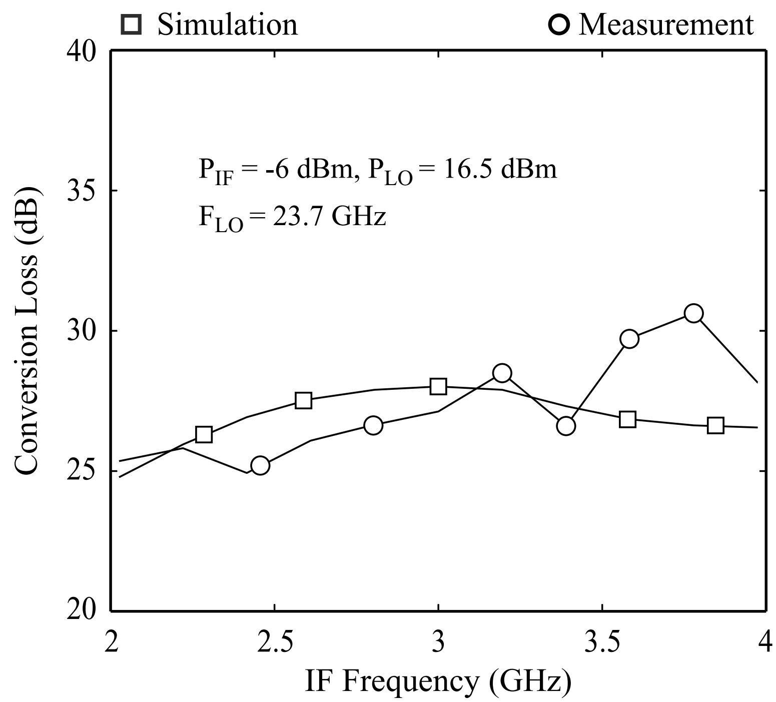

Figure 2.13: Simulated and measured conversion loss of the up-converter.

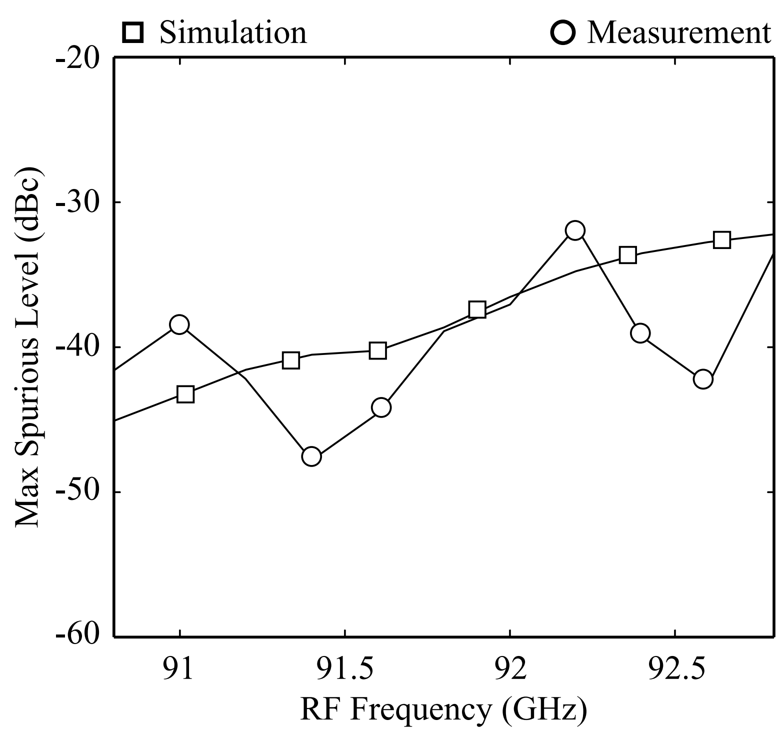

Figure 2.14: Simulated and measured spurious level of the RF signal in SPMS.

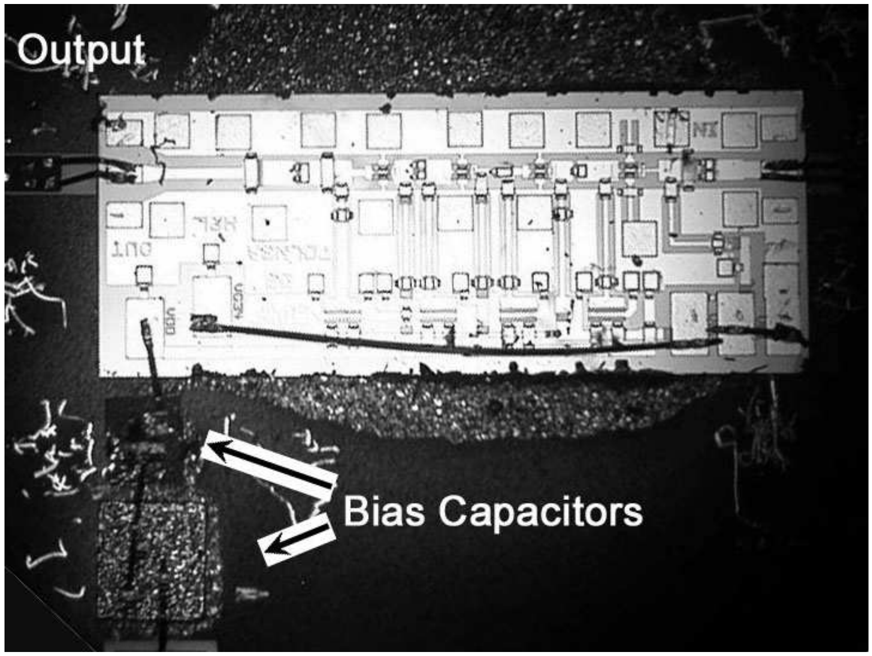

Figure 2.15: Photograph of RF amplifier and its wire bonded connections to the circuit.

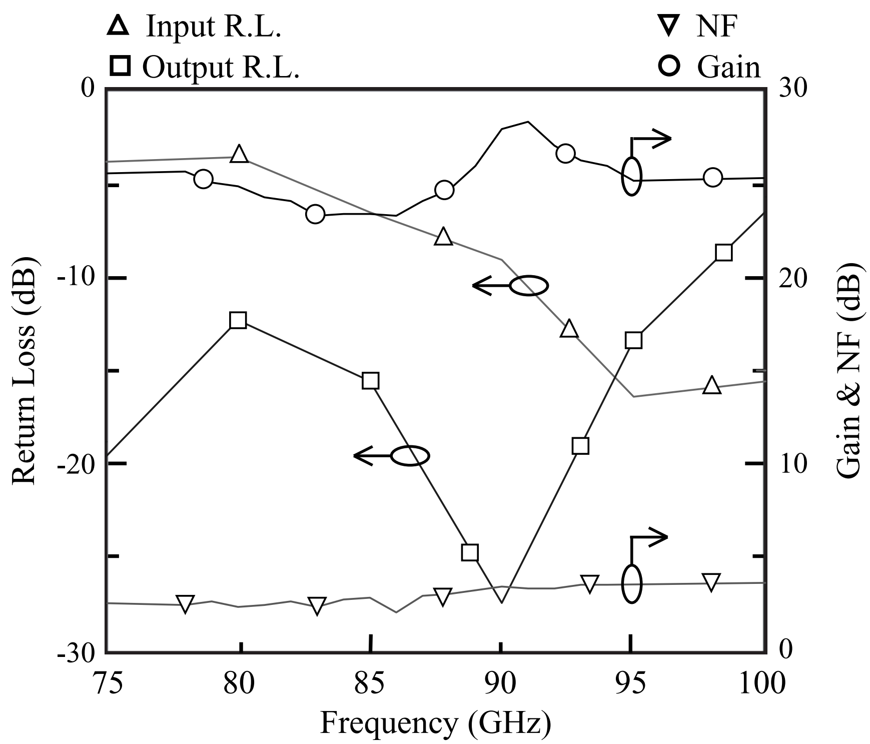

Figure 2.16: RF amplifier gain, noise figure, input and output return loss.

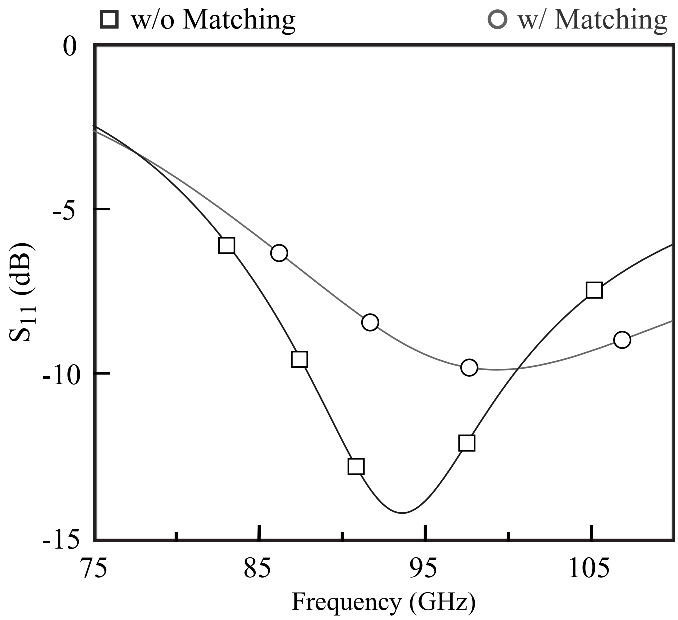

Figure 2.17: Effect of matching line on antenna return loss.

2.1.5 Antennas

The main goal of the millimeter wave scaled measurement system is to characterize propagation channels under laboratory conditions. In order to accomplish this properly, the transmit and receive antennas should have broad beam patterns. A monopole antenna is chosen for this purpose. As the monopole above a finite ground surface of the package is not automatically matched, a quarter wavelength transmission line is used to match the antenna to the circuit. As shown in Figure 2.17, quarter wavelength matching line has improved antenna return loss about 5 dB at desired frequency range. Figure 2.18 shows the antenna and the matching line between the antenna and the RF amplifier. The simulated gain patterns of this antenna, above the packaged circuit, at E- and H-planes are shown in Figures 2.19(a) and 2.19(b) respectively.

2.1.6 Packaging

The required accuracy in package dimensions has to be of the same order of the circuit elements that are connected to the package. For example in a W-band system, an error as

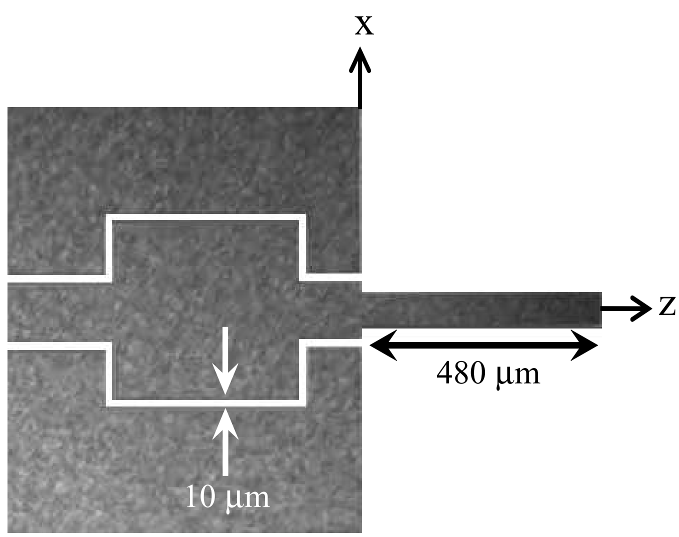

Figure 2.18: Photograph of monopole antenna and matching line.

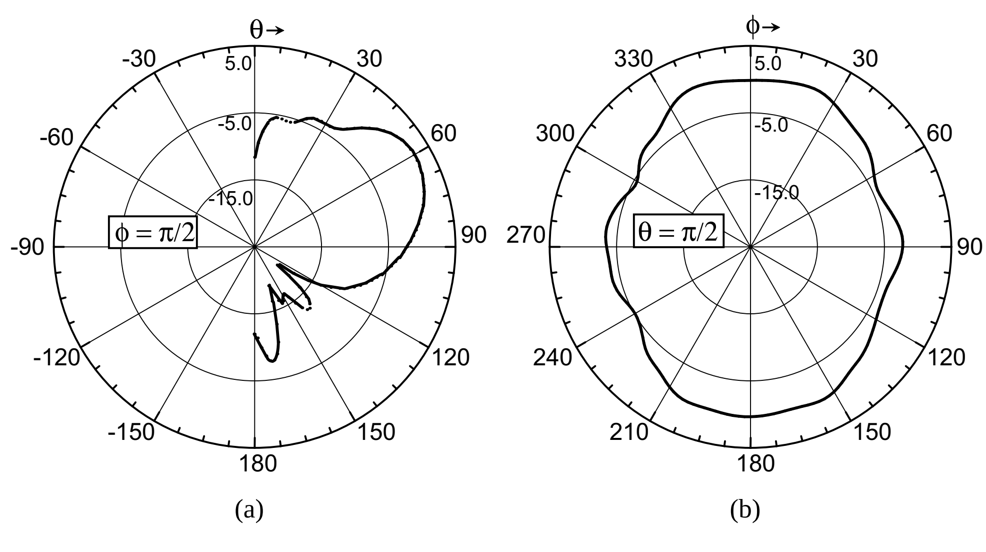

Figure 2.19: Simulated gain pattern of monopole antenna above packaged circuit; (a) E-plane, (b) H-plane.

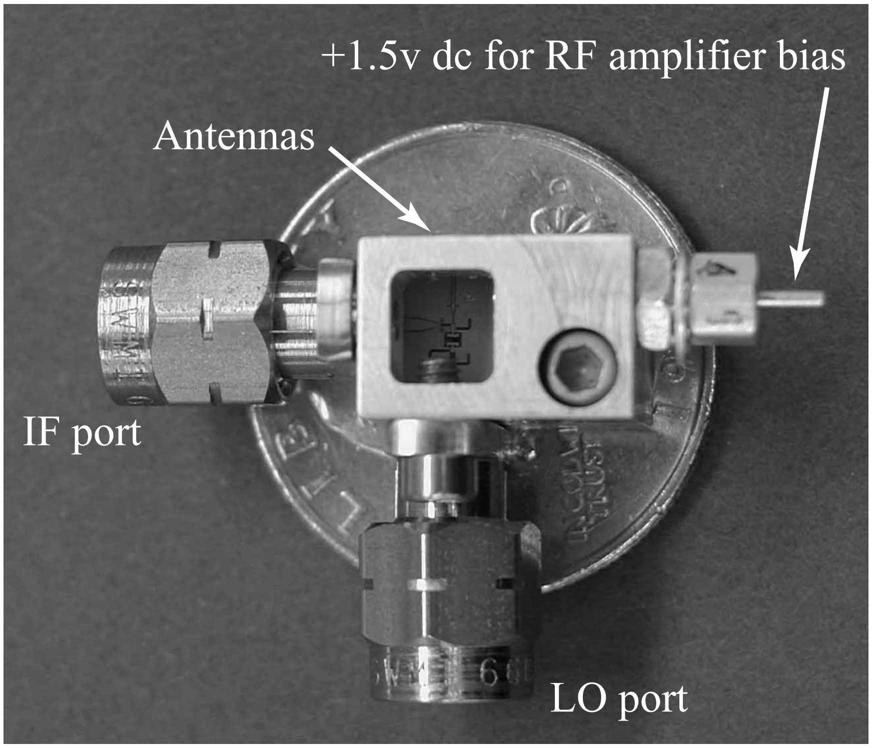

Figure 2.20: Packaged RF probe against a Quarter.

small as 10 μm in the antenna's position can change its resonant frequency by approximately 2 GHz and cause mismatching. A metallic package is designed using AutoCAD. In order to achieve the desired accuracy, the package was milled at the University of Michigan space research machine shop, using a high precision CNC machine with tolerances less than 2.5 m. The fabricated circuit on the quartz substrate was diced using an automatic dicing saw and then together with 2.4 mm coaxial connectors for the IF and LO ports was assembled with the aluminum package. The LO and IF 2.4 mm connector pins are connected to the circuit using silver epoxy. Figure 2.20 shows the packaged probe against a Quarter.

2.2 LO and IF Circuit Modules

As it is shown in Figure 2.1 there are few circuit blocks other than W-band transceiver probes. Some of these blocks have been purchased and only their specification will be mentioned in the next subsection however others have been designed and fabricated and will be described in more details.

2.2.1 IF and LO Amplifiers

IF Amplifiers

IF amplifiers are placed at both transmit and receive paths. As mentioned earlier the IF amplifier at transmit path is placed for helping VNA to operate at lower output power and consequently reducing harmonic level [45]. In the receiver path, the IF amplifier boosts down-converted signal to be detectable by the port 2 of the VNA. The transmit path's IF amplifier gain and output power is obtained by optimum required IF power by W-band transmitter probe (8 to 10 dBm) and its difference with minimum output power of the VNA without using any internal attenuators (-10 dBm). Because using internal attenuators at the VNA decreases its output signal to noise ratio (S/N). A double stage amplifier using SiGe HBT RFIC manufactured by *Stanford Microdevices* (SGA-5263) is fabricated for this purpose. As the RFIC gain was not flat over IF frequency range two parallel RC are places in cascade with each chip as gain equalizer. Figure 2.21 shows the packaged circuit. Measured gain of this amplifier with and without gain equalizer is shown in Figure 2.22. In receive path two high gain, low noise amplifier manufactured by *Miteq* is used which provide 60 dB gain and has a noise figure of 2 dB.

LO Amplifiers

Two K-band amplifiers manufactured by *NEXTEC-RF* are used to amplify LO source signal for W-band probes. These amplifiers have 20 dB gain and can provide up to 20 dBm output power. Because of the LO filter and cable losses, available power at LO port of W-band probes is 16 dBm which is sufficient for proper operation of subharmonic mixer inside the probes.

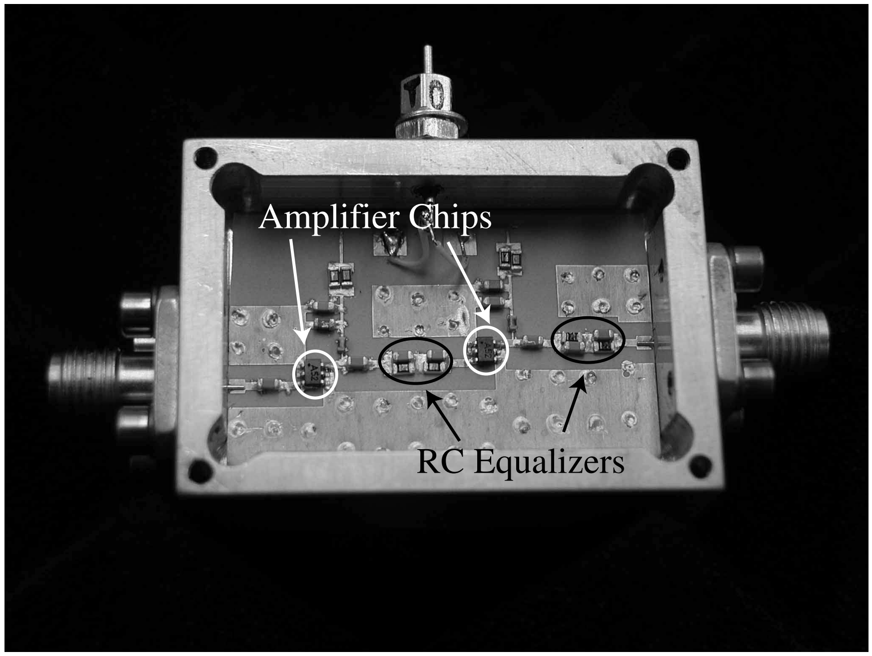

Figure 2.21: IF amplifier packaged circuit.

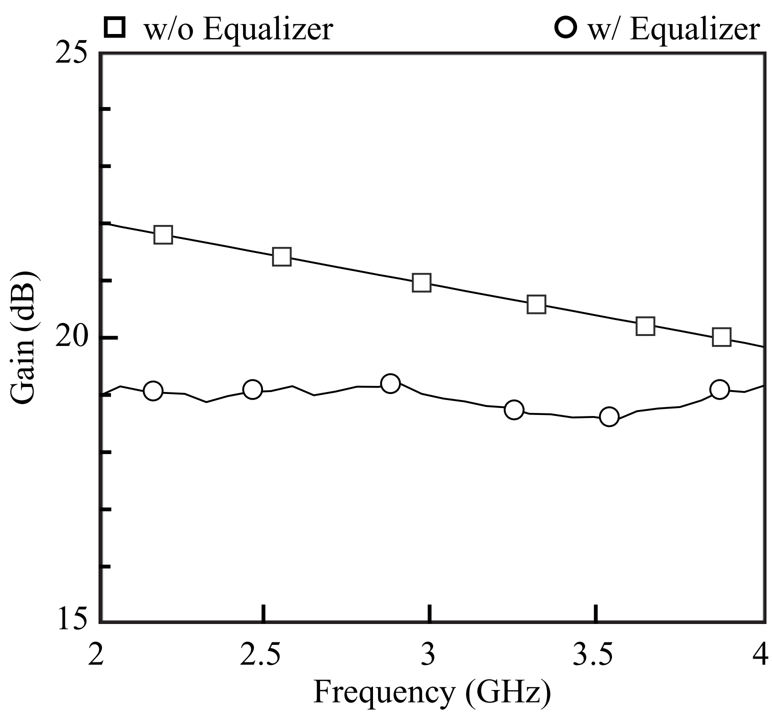

Figure 2.22: IF amplifier gain with and without equalizer.

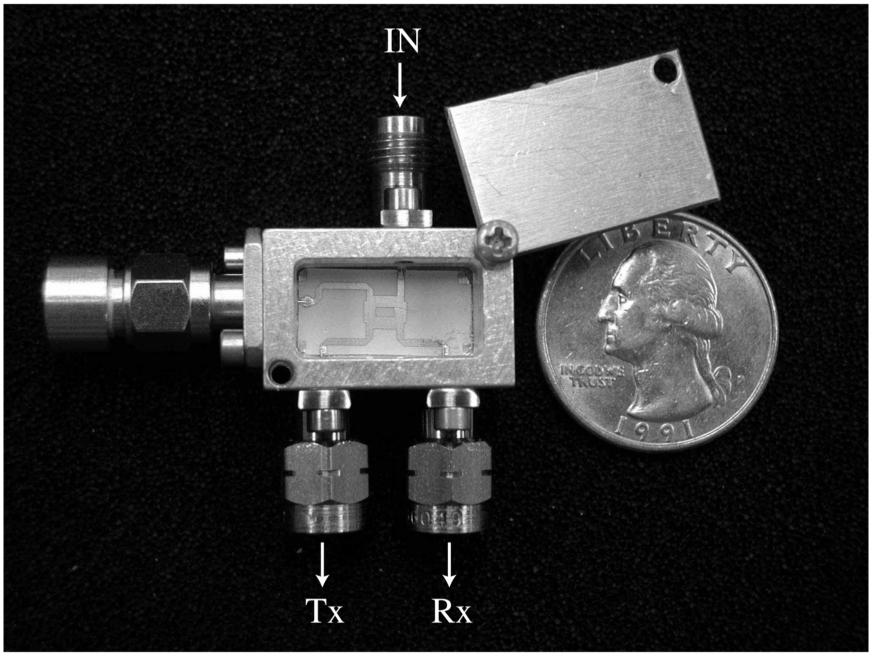

Figure 2.23: Quadrature hybrid against a Quarter.

2.2.2 LO Source, Hybrid, and Filters

A 23.7 GHz dielectric resonator oscillator (DRO) built by *Lucix corporation* that has a frequency variation of 6 kHz/^{0}C and a phase noise of -86 dBc/Hz at 10 kHz offset from the center frequency is used as common local source for transmitter and receiver probes. The output signal of the DRO is distributed to the LO amplifiers by a quadrature hybrid. The hybrid is not symmetric in order to compensate the difference between receiver and transmitter cable losses and provide equal power for the probes. Figure 2.23 shows the fabricated quadrature hybrid against a Quarter. Simulation and measurement results for this hybrid are shown in Figure 2.24. Part of difference between measurement and simulation is because of using a SMA load at the isolation port of the hybrid, which has reasonable result up to 18 GHz. IF signal leakage from the transmitter to the receiver probe through LO path has to be kept lower than minimum detectable signal by the receiver probe (-145 dBm). The LO amplifiers are narrow-band amplifiers and provide total attenuation of 97 dB at this path for IF signal ($S_{21}@F_{IF}$= -37 dB, $S_{12}@F_{IF}$= -60 dB) however considering IF signal level at transmitter probe (10 dBm) and IF to LO isolation at each probe ($\cong$ 15

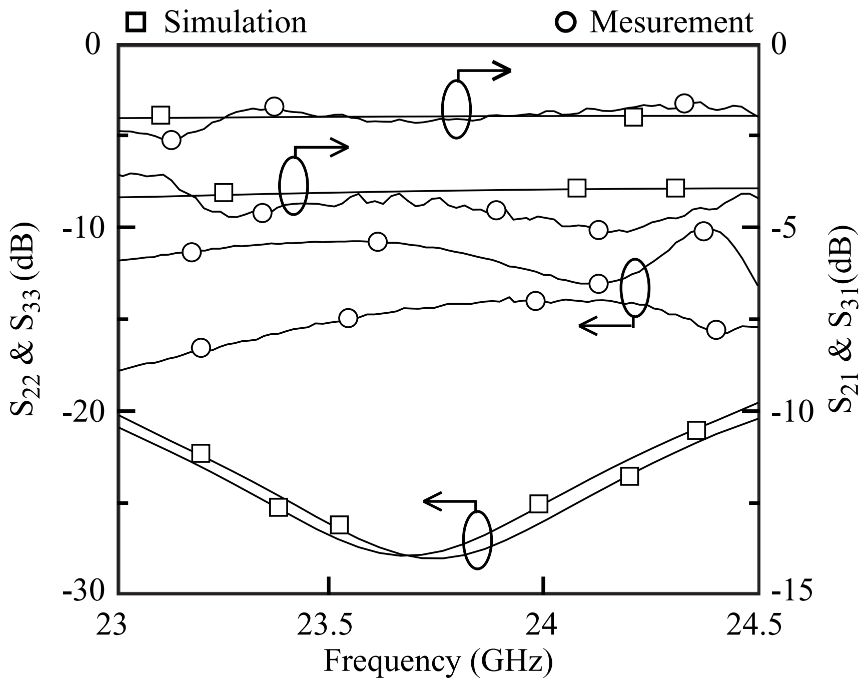

Figure 2.24: Simulation and measurement results for quadrature hybrid.

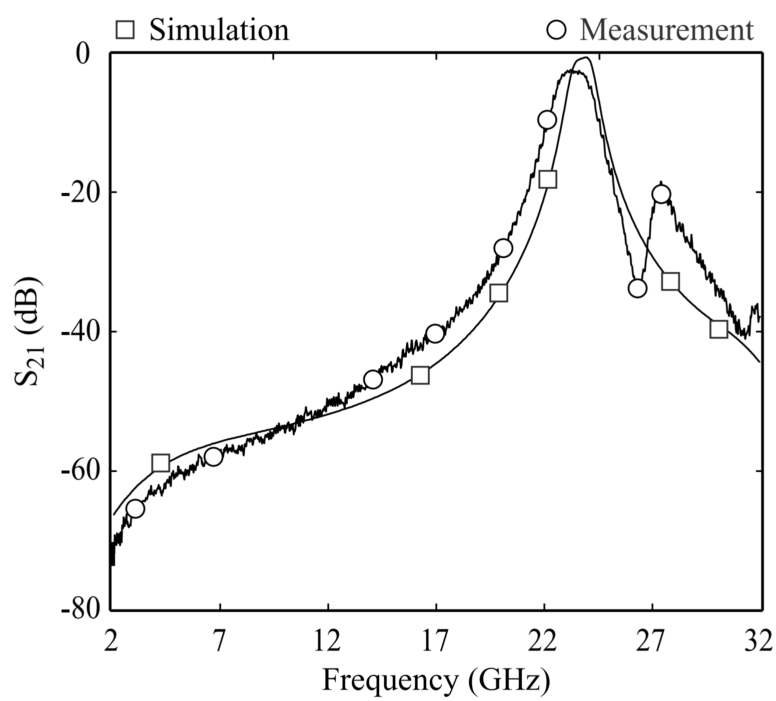

Figure 2.25: Simulation and measurement results for LO bandpass filter.

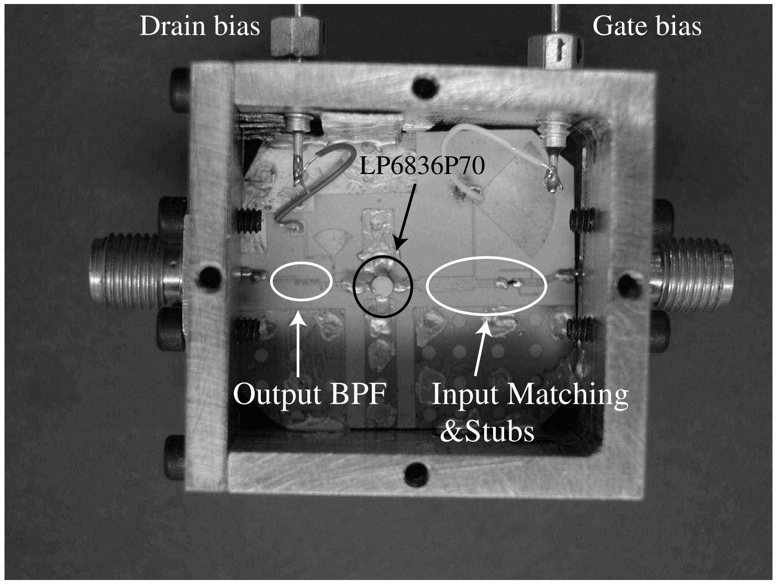

Figure 2.26: Frequency multiplier packaged circuit.

dB) still 30 dB more isolation is required. For this purpose an inductive coupled resonator bandpass filter is added after each LO amplifier. These are 2-poles filter and each one as shown in Figure 2.25 provide at least 60 dB attenuation at IF frequency band. It may seems to be over designed however because of other coupling mechanism between circuit modules using these filters found to be necessary.

2.2.3 Frequency Multiplier

In a primary system design it was intended to use a combination of a DRO operating at one third of the desired local frequency and a frequency tripler to generate the LO signal for W-band probes. For this purpose a frequency tripler were designed and fabricated. The nonlinear element in the frequency tripler was a PHEMT built by *Filtronic* (LP6836P70). Figure 2.26 shows the fabricated circuit. The measured and simulated output power versus input power and input frequency are shown in Figures 2.27 and 2.28 respectively. It should be mentioned that primary system design were based on a LO at 22.5 GHz.

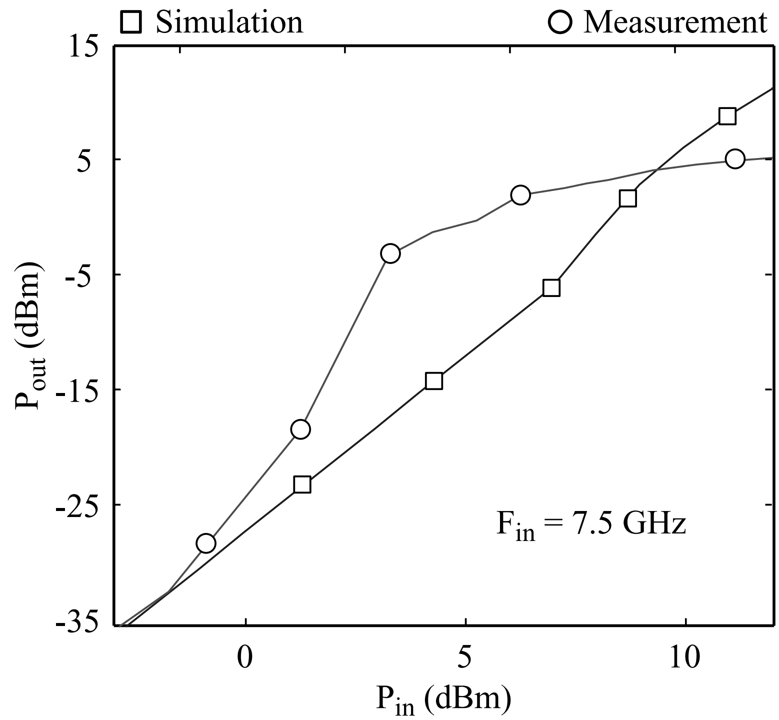

Figure 2.27: Output power vs. input power of the frequency multiplier.

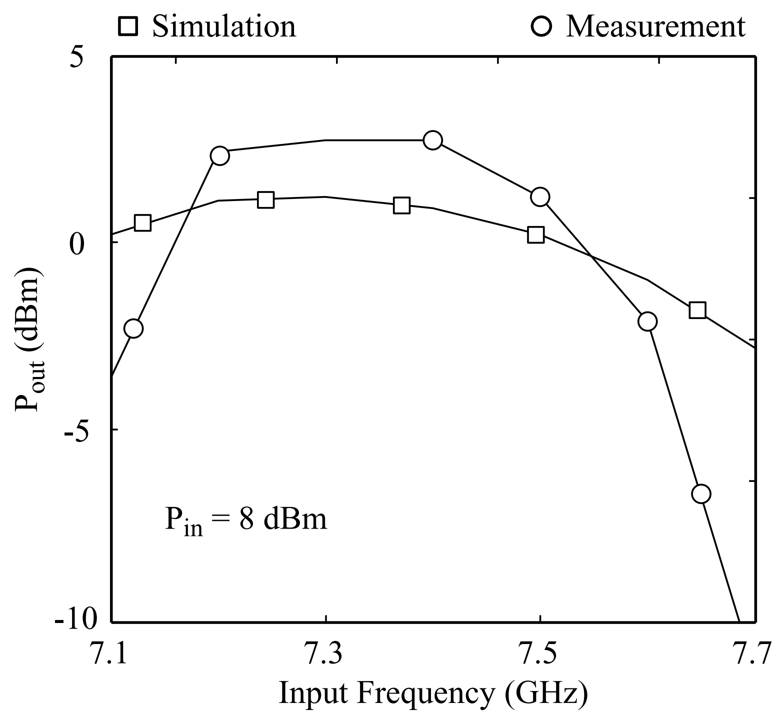

Figure 2.28: Output power vs. input frequency of the frequency multiplier.

CHAPTER 3

Scaled Environment

In this chapter we discuss the construction process of scaled buildings followed by different dielectric measurement techniques which were used for characterizing buildings' material properties. Design, fabrication and specification of XY-table, which is a computer controlled tool for precise placement and movement of the receive probe in the scaled city is describe at the end of this chapter.

3.1 Scaled Building Fabrication

As mentioned earlier SPMS is designed to evaluate the performance of physics-based propagation models. As such, beside electronic precision for signal amplitude and phase measurement over a wide dynamic range, accurate rendition of the environment is also important. This includes accurate knowledge of geometrical features of scatterers (like buildings) as well as their material properties. To accommodate these features, scaled buildings and other scatterers with an arbitrary degree of complexity and well-characterized dielectric properties are used. A precise 3-D printer is used to make scaled buildings. The 3D printers use a powder-binder technology to create parts directly from digital data. First, the 3D printer spreads a thin layer of powder. Second, an ink-jet print head prints a binder in the cross-section of the part being created. Next, the build piston drops down, making room

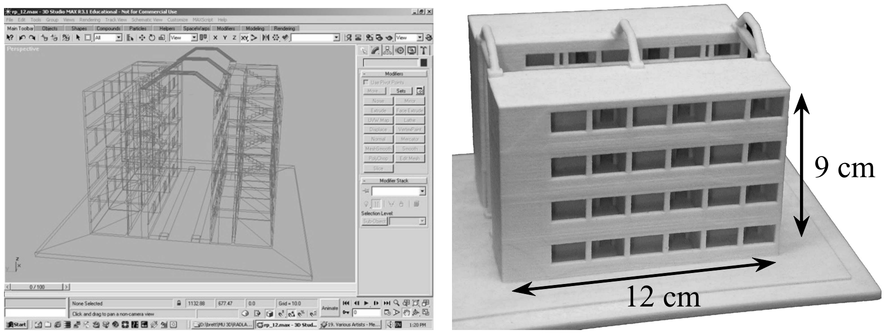

(a) (b)

Figure 3.1: Scaled building; (a) CAD model, (b) printed building.

for the next layer, and the process is repeated. Once the part is finished, it is surrounded and supported by loose powder, which is then shaken loose from the finished part. This printer can use different materials and can make any building with any desired fine features. Any standard CAD software can be used to draw the buildings and export the geometry file for the 3D printer. Figures 3.1(a) and 3.1 show the CAD model of a scaled building and actual building printed by the 3D printer. Figure 3.2 shows the first version of a scaled city block with simple building structures. It can be seen that the scaled city has a flexible grid which is designed to help making an arbitrary arrangement of the blocks including roads, sidewalks, cars, and buildings. The 3-D printer is capable of making complex building with fine details such as one shown in Figure 3.3 and this feature can be used for maing buildings with different level of details and study their effect on wireless channel using the SPMS. The result of such study is very beneficial for physics-based model developments as it helps to understand how important are the environment details and in what degree they have to be considered in channel simulations.

3.2 Dielectric Characterization

Dielectric properties of scatterers are needed for numerical simulation of wave propagation. Hence the material used to make the blocks must be characterized at W-band

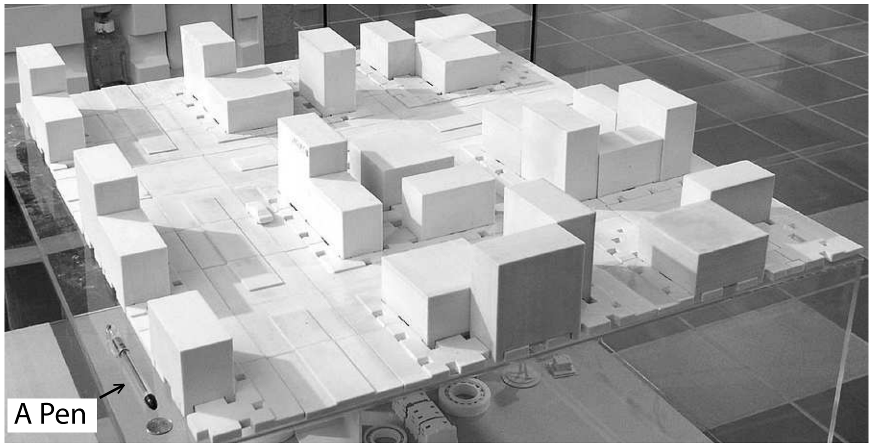

Figure 3.2: Scaled city block.

(a) (b)

Figure 3.3: Scaled University of Michigan president building; (a) front view, (b) side view.

frequencies. In this study, different techniques are used to characterize the real and imaginary parts of the dielectric constant of the material used in constructing the scaled buildings over a wide range of frequency. The first method is based on capacitor measurements at L-band and below and has been done using Agilent E4491A RF impedance/material analyzer. The second method is based on transmission and reflection measurements in a WR-90 X-band waveguide and post processing has been done using HP 85071E material measurement software. The third dielectric measurement is done at the W-band using transmission measurement through a dielectric slab at different incidence angles, and reflection measurement of the back metal dielectric slab [46]. The lower frequency dielectric measurements are mainly done to verify the measured results at the W-band.

3.2.1 L-Band Measurement

For the L-Band measurements, an Agilent E4991A RF impedance/material analyzer is used for characterizing the permittivity and loss tangent from 1 MHz to 3 GHz. The dielectric samples used for this measurements are shown in Figure 3.4. The permittivity and loss tangent measurement accuracy using this method are calculated by applying 3.1 and 3.2 [47]:

$$\frac{\Delta\varepsilon_{rm}}{\varepsilon_{rm}} = \pm\left[5 + \left(10 + \frac{0.1}{f}\right)\frac{t}{\varepsilon_{rm}} + 0.25\frac{\varepsilon_{rm}}{t} + \frac{100}{\left|1 - \left(\frac{13}{f\sqrt{\varepsilon_{rm}}}\right)^2\right|}\right][\%] \tag{3.1}$$

$$\frac{\Delta\tan\delta_m}{\tan\delta_m} = \pm[E_a + E_b][\%] \tag{3.2}$$

where,

$$E_a = 0.002 + \frac{0.001}{f}\cdot\frac{t}{\varepsilon_{rm}} + 0.004f + \frac{0.1}{\left|1 - \left(\frac{13}{f\sqrt{\varepsilon_{rm}}}\right)^2\right|} \tag{3.3}$$

$$E_b = \left(\frac{\Delta\varepsilon_{rm}}{\varepsilon_{rm}}\cdot\frac{1}{100} + \varepsilon_{rm}\frac{0.002}{t}\right)\tan\delta_m \tag{3.4}$$

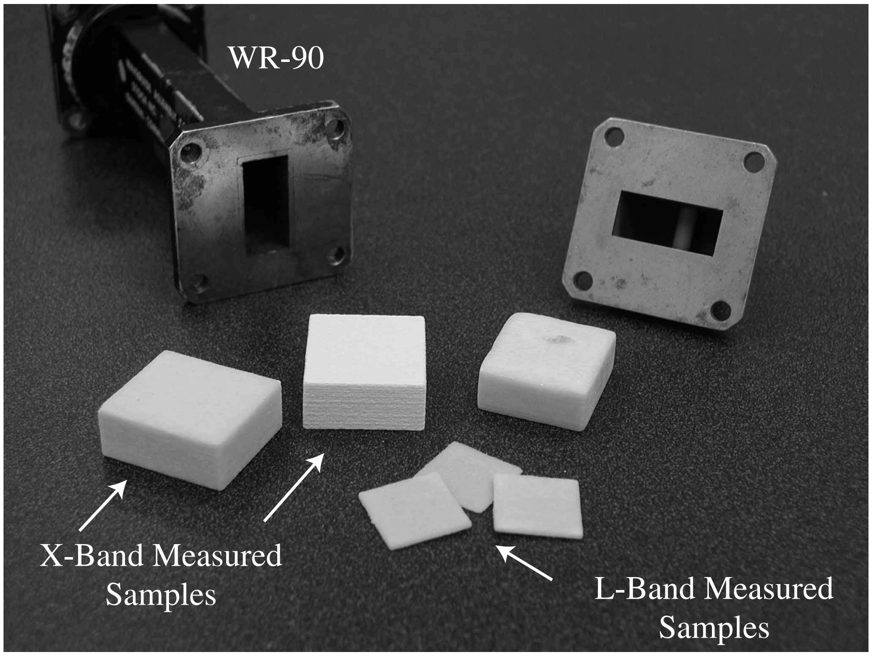

Figure 3.4: Dielectric samples.

f is the measurement frequency in GHz,t is thickness of the material under test (MUT) in mm, ε_{rm} is the measured value of permittivity, and $\tan\delta_m$ is the measured value of loss tangent. For the measured samples with 1-2 mm thickness and typical permittivity of 3, maximum error is approximately %10 at 300 MHz [47].Figure 3.5 shows measured permittivity and loss tangent for two different samples.

3.2.2 X-Band Measurement

Dielectric characterization at X-band (8.2-12.4 GHz) is done using a transmission measurement through cubic samples shown in Figure 3.4 in a WR-90 waveguide. HP 85071E material measurement software is used for calibration and extracting the permittivity and loss tangent from measured data. The transmission line method works best for materials that can be precisely machined to fit inside the sample holder. The 85071E features an algorithm that corrects for the effects of an air gap between the sample and holder, considerably reducing the largest source of error with the transmission line technique. The overall accuracy of this technique is 1 to 2 percent [48]. Figure 3.6 shows measured results for two

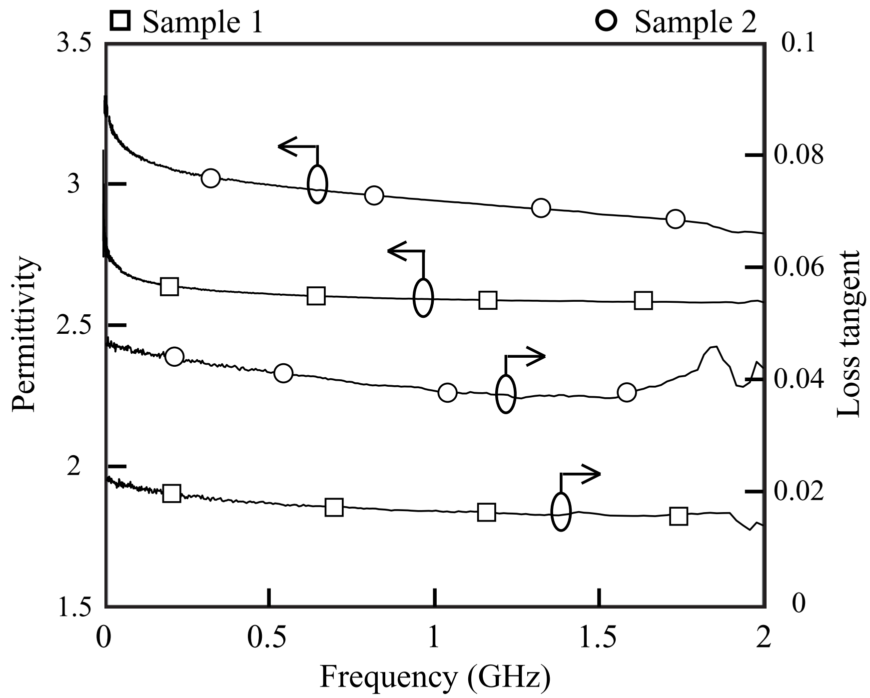

Figure 3.5: Measured permittivity and loss tangent at L-band for two samples.

different samples using this technique.

3.2.3 W-Band Measurement

Figure 3.7 shows the free space measurement setup used for dielectric characterization at W-band. The dielectric slab is placed in the far-filed of both horn antennas and is selected large enough to minimize diffraction effects. Measurements for both transmission through dielectric slab and reflection from a back metal slab measurement were performed. However the reflectivity measurement showed better agreement with theory and is used as final data. Calibration error, which can be seen as a fast variation in raw measured data, has been removed using a 14^{th} order lowpass Butterworth filter whose response in the spatial domain, is shown in Figure 3.8. Measured reflectivity in the spatial domain before and after filtering is shown in Figure 3.9. Coherent reflectivity for the back metal slab is calculated using the formulation in chapter 4.14 of [46] (see appendix A). Figures 3.10 and 3.11 compare simulated results for optimum values of ε_r with measurement for two different di-

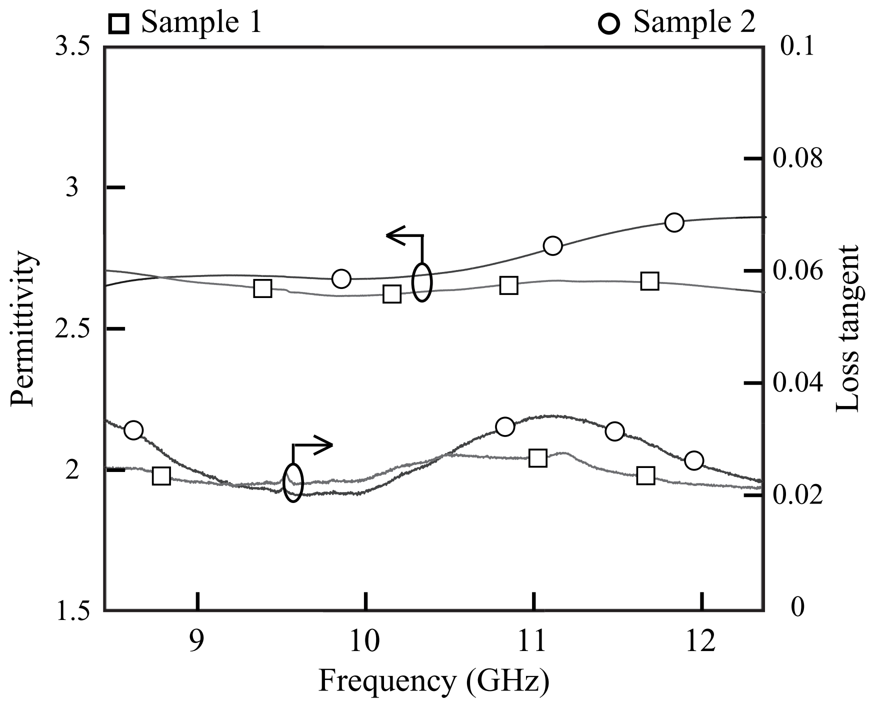

Figure 3.6: Measured permittivity and loss tangent at X-band for two different samples.

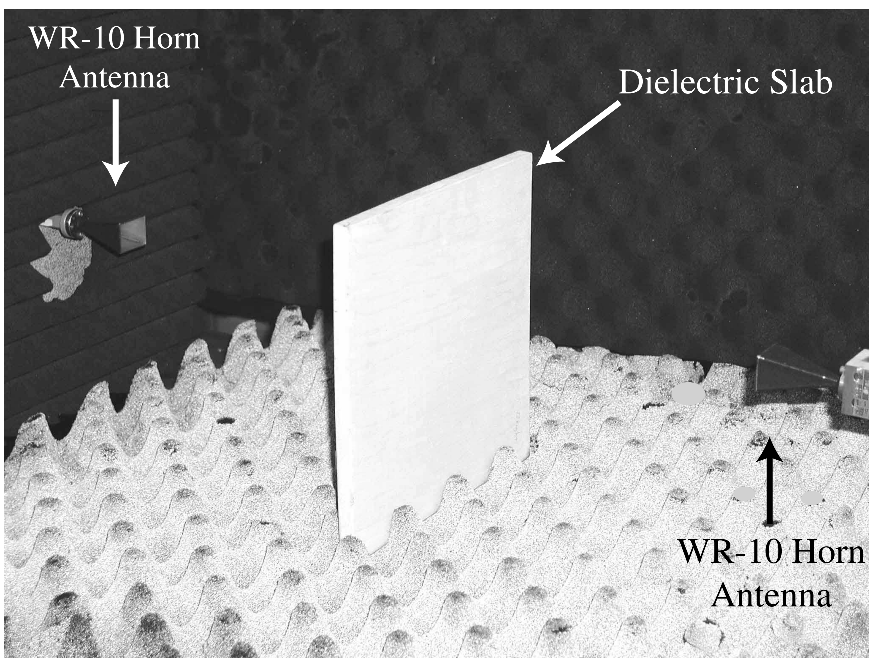

Figure 3.7: Free space dielectric measurement setup at W-band.

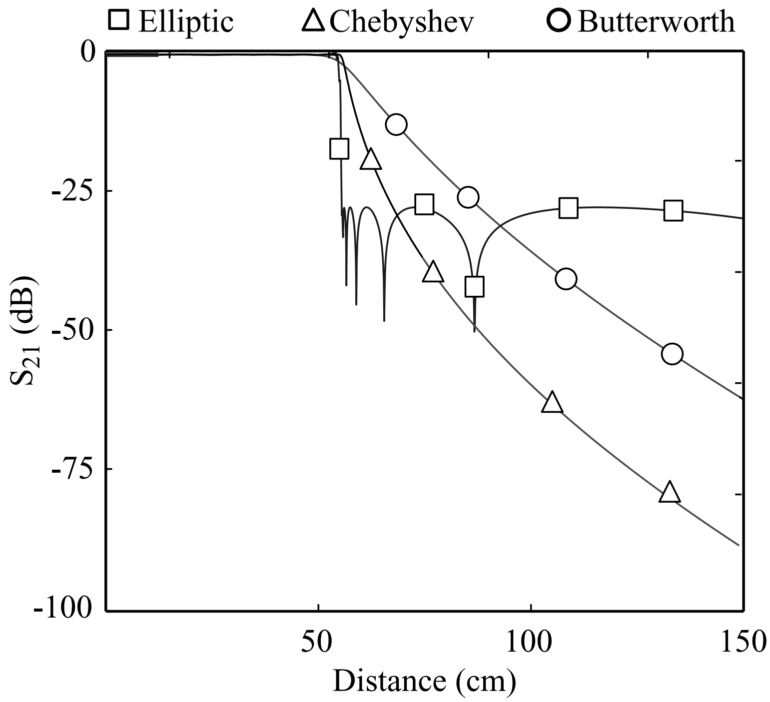

Figure 3.8: Spatial domain filters.

Table 3.1: Measured Effective Dielectric Constant

Frequency Band	L	X	W
Sample 1	2.7-j0.05	2.40-j0.04	2.34-j0.03
Sample 2	3.05-j0.15	2.70-j0.07	2.48-j0.06

electric slabs. The measurement results for the two different samples, using the discussed techniques for different frequencies, are summarized in Table 3.1. The permittivity of material used in the construction of the scaled buildings resembles those of brick and concrete.

3.3 XY Table

A computer-controlled xy-table that places the receiver probe at any arbitrary position within a 1.5 m $\times$ 1.5 m area was designed and built. The system includes a motion control card, two step-motors, power amplifiers, encoder and drivers. The computer issues commands to the motion control card, which in turn triggers the power amplifier to drive the

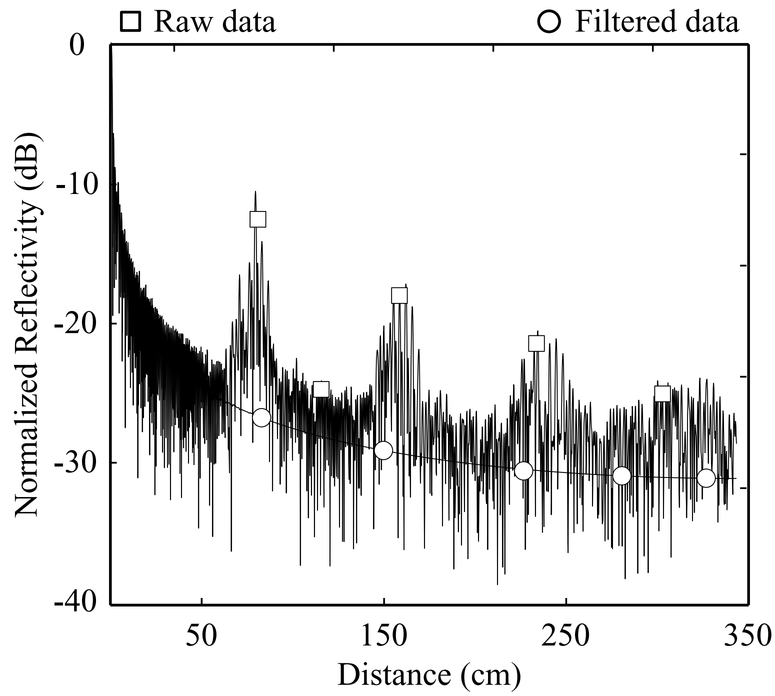

Figure 3.9: Measured reflectivity in the spatial domain.

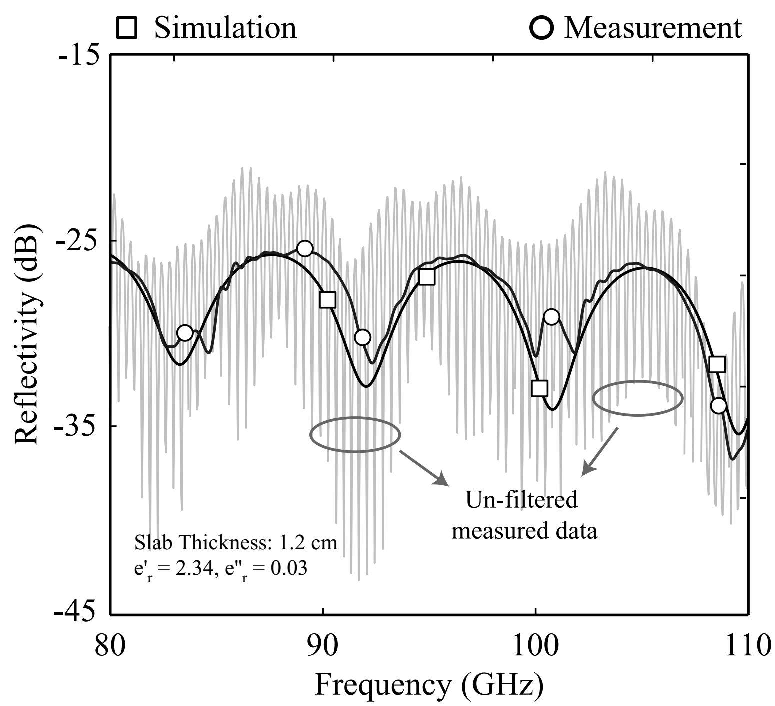

Figure 3.10: Simulated and measured reflectivity of the dielectric slab at W-band, sample 1.

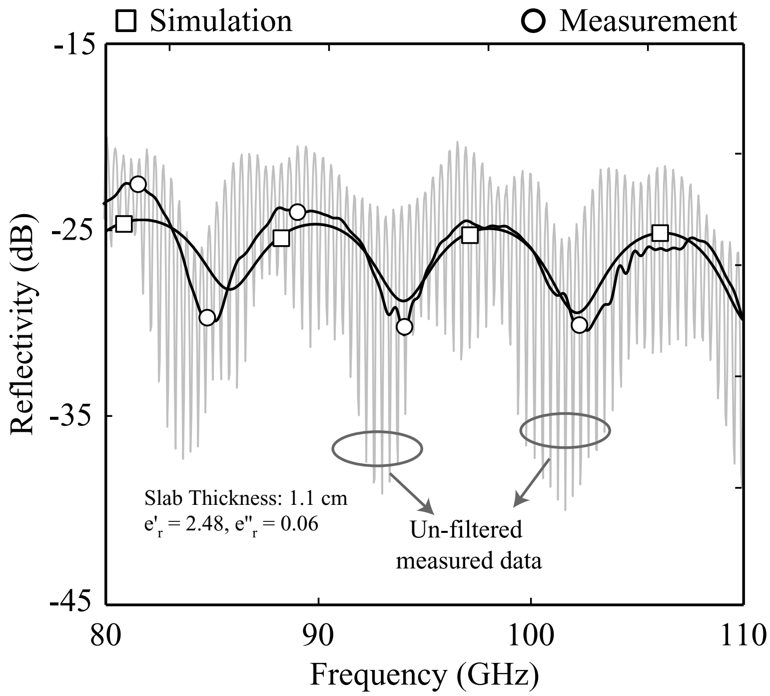

Figure 3.11: Simulated and measured reflectivity of the dielectric slab at W-band, sample 2.

motor. An optical encoder attached to each motor sends the position and velocity data back to the computer. The computer uses this information to control the probe movement. The system placement is accurate to within 0.25 mm. This is acceptable accuracy even for fast fading measurements at the RF frequency range (90.8-92.8 GHz) at which the wavelength is about 3.3 mm. Figure 3.12 shows the block diagram of the xy-table system. A four layer pcb (printed circuit board) with low interference considerations is designed and fabricated for use as the motherboard of this system. Figure 3.13 shows the layout of this board.

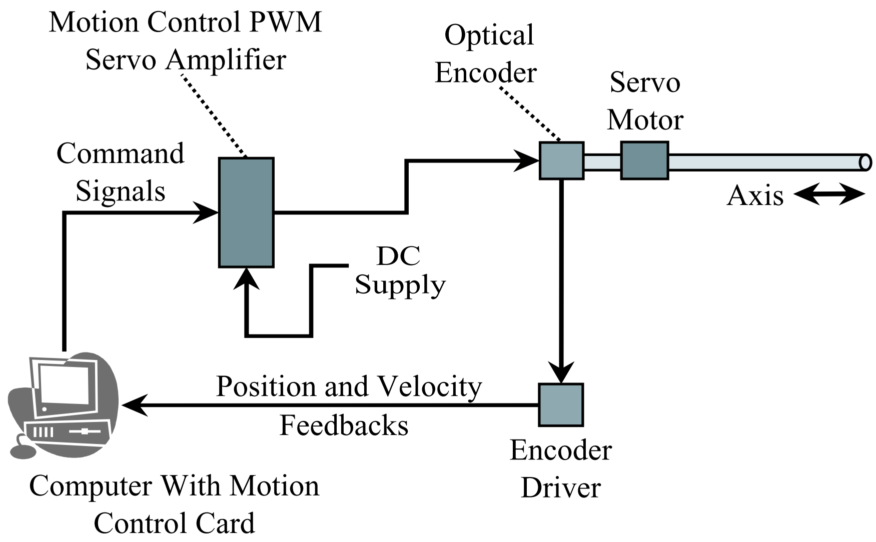

Figure 3.12: XY-Table block diagram.

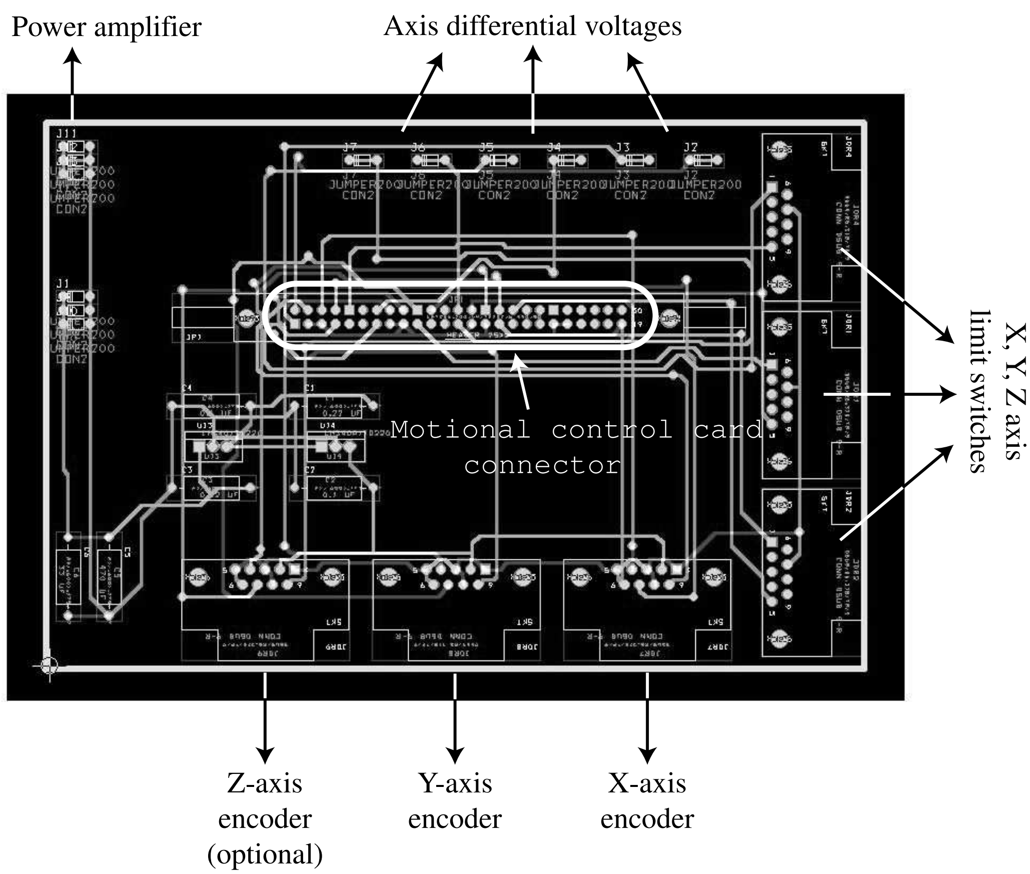

Figure 3.13: XY-Table motherboard layout.

CHAPTER 4

System Calibration and Specification

4.1 System Calibration

In the previous chapter the millimeter-wave scale measurement system and its major components for the characterization of propagation environment were described. Through the proper up- and down-conversion a vector network analyzer is used to presume the amplitude and phase of the signal over a 2 *GHz* bandwidth. Like any measurement instrument, accurate measurements of field quantities in a propagation environment are limited by measurement errors. The source of measurement errors can be categorized into two major groups.

1 Random errors that are not repeatable (uncorrectable) such as: a) thermal noise, b) environmental changes, c) inconsistencies in attaching connectors, and d) operator error

2 Systematic errors that are repeatable (correctable) such as: a) mismatches at connectors, b) leakage in directional couplers, c) difference in the system transfer functions of different channels, and d) cross-talk between the reference and test channels. In this section a brief discussion on the systematic error sources in the SPMS is presented. Methods for determining the source of errors are described and improvements in the hardware are

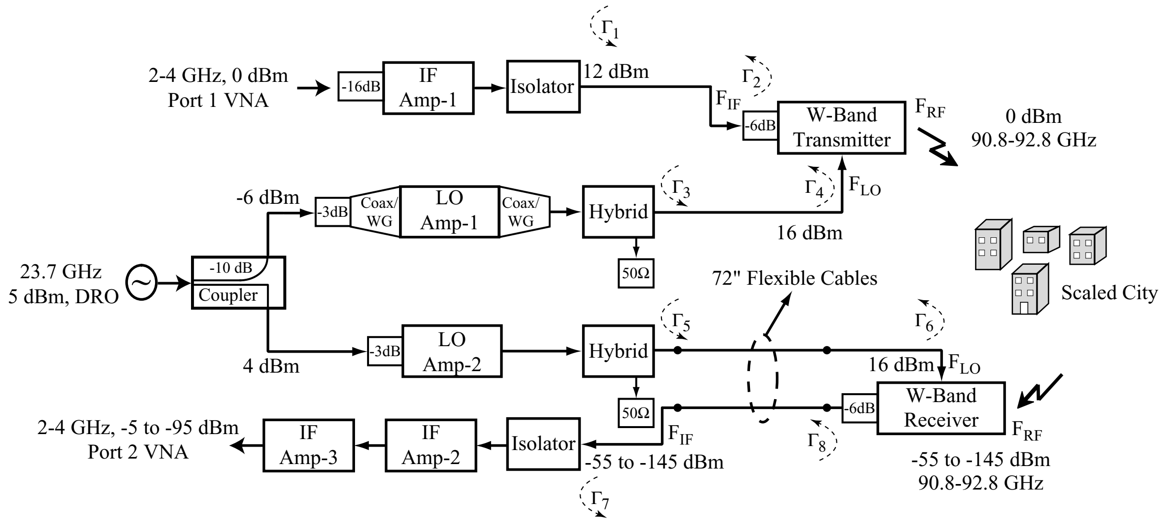

Figure 4.1: Signal flowgraph in scaled propagation measurement system.

implemented to reduce unwanted signals as much as possible.

In order to obtain maximum practical performance of the SPMS, all subcircuit and modules of the system should be impedance matched at the IF and LO frequencies appropriately. Figure 4.1 shows critical points where the reflection coefficient at each junction is defined by Γ_i ($i = 1, \ldots, 8$). These reflections generate multipath inside the cables and degrade the system performance.

Nonlinear devices such as mixers are difficult to match. For example return loss at the IF ports of the transmitter and receiver probes are only about 7 dB. This is due to the miniaturized size of the probes, which rejects the possibility of using a matching circuit at the IF frequency. Hence 6 dB coaxial attenuators have been added to the IF ports of the mixers to improve their return loss (Γ_2 and Γ_8), up to 19 dB, at the cost of 6 dB reduction in the system dynamic range at the worst case. Considering 19 dB return loss at the isolator ports (Γ_1 and Γ_7) and 1 dB cable loss, any ringing in the IF cables would be at least 40 dB below the main signal.

Another source of signal multipath in the up- and down-converter is the leakage of the IF signal to the LO ports of the mixers. The short-circuit stubs at the LO ports of the up- and down-converter provides only 9 dB isolation between the IF and LO ports at the IF

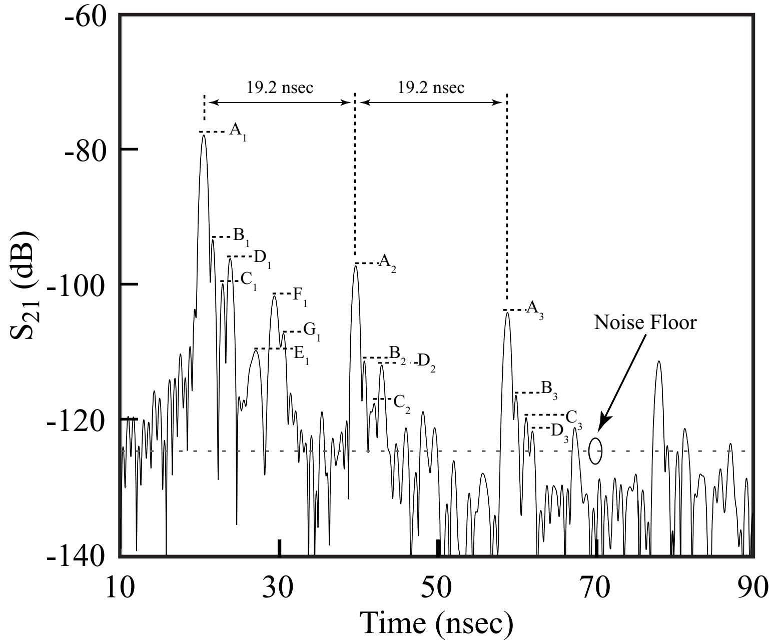

Figure 4.2: Power delay profile of un-calibrated SPMS for a through case.

frequencies. This is in addition to the output impedance mismatch of the LO amplifiers that appears as an open circuit for the IF signals. As a result, the IF leakage to the LO cables can cause a multipath with a level that is only 20 *dB* below the main signal. Figure 4.2 shows power delay profile of the SPMS (without RF amplifiers) in the absence of any scatterers when the transmitter and receiver probes are placed in a mm-wave anechoic chamber. As shown the received signal in the time domain has a semi-periodic behavior ($A_1B_1C_1D_1 \rightarrow A_2B_2C_2D_2 \rightarrow A_3B_3C_3D_3$) with duration of 19.2 *nsec* which is equal to the two-way propagation delay in the receiver LO cable as calculated by:

$$LO\ cable\ delay = \frac{2L_{cable_1}}{V_{cable_1}} + \frac{2L_{cable_2}}{V_{cable_2}} = \frac{2 \times 0.33}{0.695 \times 3e8} + \frac{2 \times 1.83}{0.76 \times 3e8} = 19.2\ (nsec) \quad (4.1)$$

where cable$_1$ (*RG405*) and cable$_2$ (*Lab-Flex160*) are both *Florida RF Labs* products with propagation velocity of *0.695c* and *0.76c* respectively, and the unknown spurious signal (G_1 in Figure 4.2) is probably a result of the non-ideal absorbers at oblique angles.

Also as shown in Figure 4.2, the transmitted signal is not a clean single pulse and this

Table 4.1: Multiple reflection/path in the transmitter signal shown in Fig. 4.2

Signal	Dealy(nsec)	Amplitude(dBc)	Multipath Source / Path
B_1	1.13	-15.4	IF port mismatch/IF cable_1
C_1	2.40	-21.8	Unknown/Unknown
D_1	3.34	-18.1	IF leakage to LO/LO cable
E_1	6.58	-31.7	IF leakage to LO/LO cable (double bounces)
F_1	8.93	-23.6	IF port mismatch/IF $\text{cable}_{1,2}$
G_1	10.09	-29.1	Unknown/Unknown

is due to the multiple reflection of the IF and LO signals inside the transmitter probe's IF and LO cables as shown in Table 4.1.

In order to prevent multipath in the LO cable, the leaked IF signal into the LO port must be absorbed. For this purpose, a three port hybrid whose layout is shown in Figure 4.3, has been added to the output of the LO amplifiers. These hybrids provide an acceptable match through the lowpass filter for the IF signal. In addition to the removal of multiple reflections, these hybrids also improve isolation between the IF ports through the LO path, while having minimal effect on the LO signal level. This hybrid is composed of a bandpass filter at the LO frequency and a lowpass filter whose passband covers the IF signal band. As mentioned earlier the lowpass filter is terminated by a 50 Ω load to dissipate leaked IF signal. The simulated and measured insertion loss and return loss values for this hybrid are shown in Figures 4.4 and 4.5, respectively. As it can be seen Γ_3 and Γ_5 are now less than -20 dB at the IF frequencies which guarantees suppression of the ringing of the IF signal in the LO cables by at least 40 dB below the main signal.

Another major factor in addition to multipath inside cables, which can degrade the performance of the SPMS, is the direct IF leakage from transmitter probe to the receiver probe. This can happen either through the LO path or by radiation from the packages. The isolation between the transmitter and receiver IF ports through the LO path can be written

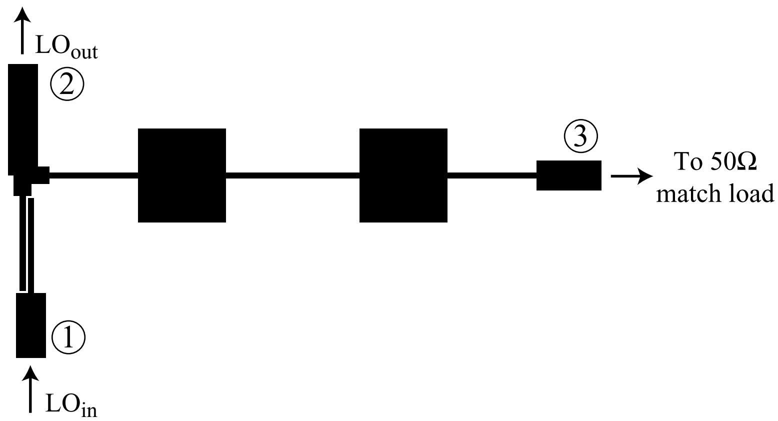

Figure 4.3: Three ports hybrid at LO path for preventing IF ringing in the cable.

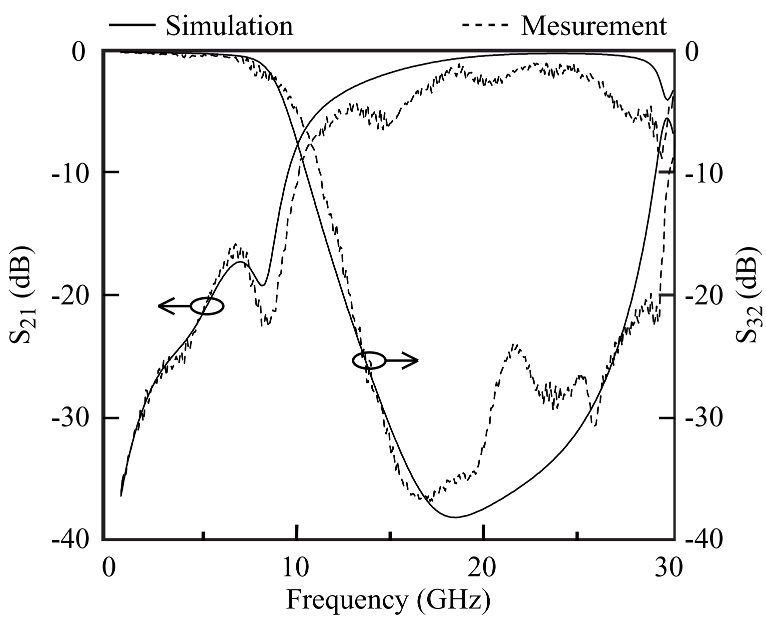

Figure 4.4: Measured and simulated insertion loss of the three ports hybrid.

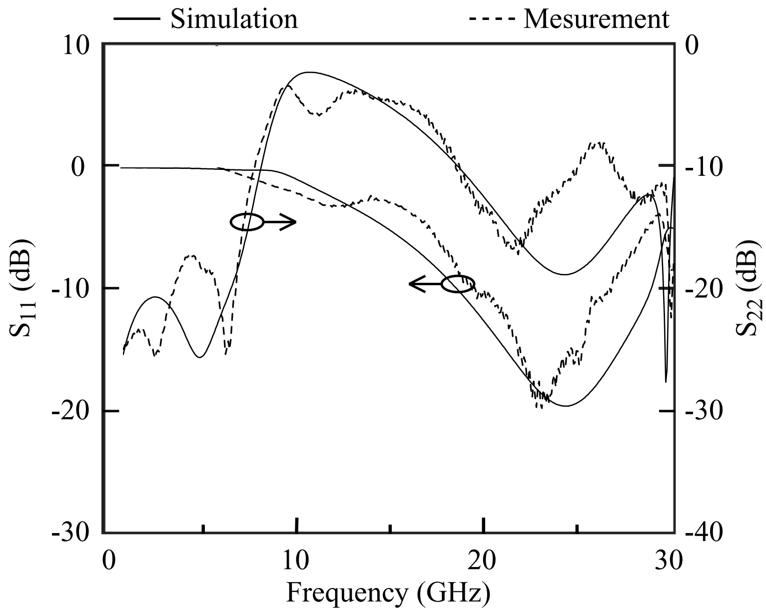

Figure 4.5: Measured and simulated return loss of the three port hybrid.

as:

$$(Tx \rightarrow Rx)\ IF_{isolation}(dB) =$$
$$2 \times (IF \rightarrow LO)_{isolation} + 2 \times (Hybrid_{isolation}) + 2 \times (Coax \rightarrow W.G.)_{isolation} + S_{12,LO\ Amp_1} +$$
$$Coupler_{isolation} + S_{21,LO\ Amp_2} = 20 + 48 + 60 + 2 \times (Coax \rightarrow W.G.)_{isolation} + 35 + 37 =$$
$$200 + 2 \times (Coax \rightarrow W.G.)_{isolation} \quad (4.2)$$

The IF leakage can be ignored if it is significantly ($\geq 10\ dB$) less than the minimum detectable power at the input of the receiver's IF amplifier. This means that the isolation between IF ports should be at least 10 dB more than the difference between the the IF transmitted power (5 dBm) and minimum detectable power at the input of the receiver's IF amplifier.

In order to calculate minimum detectable power at the input of the receiver's IF amplifier, the sensitivity of the receiver probe must first be calculated. The sensitivity of the

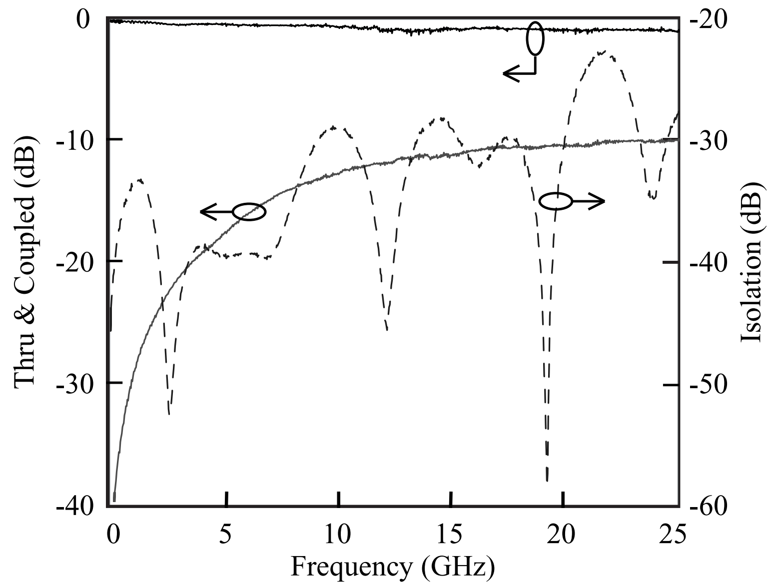

Figure 4.6: Measured S-parameters of the 10 dB coupler in LO path.

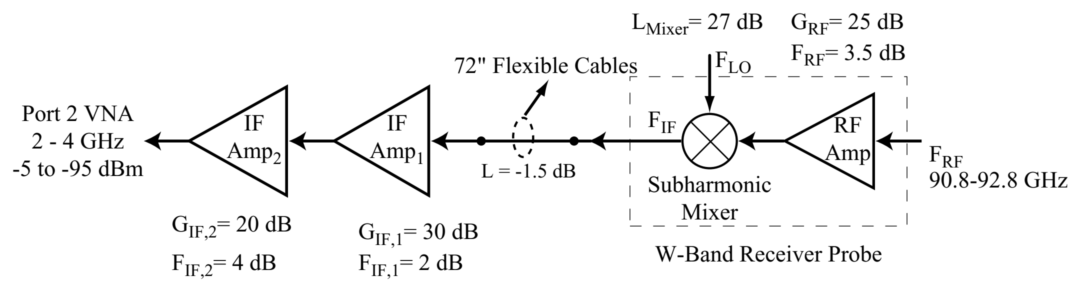

Figure 4.7: Gain and noise characteristics of the receiver chain.

receiver probe is calculated using the sensitivity of the vector network analyzer (VNA), or the gain and noise characteristics of the all components in the receiver chain if the thermal noise power happened to be more than the VNA sensitivity. The dynamic range of the VNA used in the SPMS (8720D) is 100 dB for 5 dBm test power and an IF sweep bandwidth equal to 10 Hz [45]. Hence the sensitivity of the VNA is -95 dBm $(= 5dBm - 100dB)$.

In order to calculate the thermal noise power at the VNA port, the noise figure for the receiver path including the receiver probe and IF amplifiers must be calculated. For the receiver chain shown in Figure 4.7, total noise figure can be written in the following form. where F and G are noise figure and gain respectively.

$$F_{Rx} = F_{RFamp} + \frac{F_{mixer} - 1}{G_{RFamp}} + \frac{(F_{cable} - 1)L_{mixer}}{G_{RFamp}} + \frac{(F_{IFamp_1} - 1)L_{mixer}L_{cable}}{G_{RFamp}} + \frac{(F_{IFamp_2} - 1)L_{mixer}L_{cable}}{G_{RFamp}G_{IFamp_1}} \tag{4.3}$$

As for the cable and single side band mixer noise figure are equal to their attenuation and conversion loss respectively, 4.3 can be simplified to:

$$F_{Rx} = F_{RFamp} + \frac{L_{mixer} - 1}{G_{RFamp}} + \frac{(L_{cable} - 1)L_{mixer}}{G_{RFamp}} + \frac{(F_{IFamp_1} - 1)L_{mixer}L_{cable}}{G_{RFamp}} + \frac{(F_{IFamp_2} - 1)L_{mixer}L_{cable}}{G_{RFamp}G_{IFamp_1}} \tag{4.4}$$

Using the values shown in Figure 4.7 F_{Rx} can be calculated and is found to be 5.8 ($NF_{Rx} = 7.6\ dB$). Thermal noise power for a 10 Hz bandwidth is $-163\ dBm$, hence noise power at the VNA port can be written as:

$$P_{noise} = -163(dBm) + NF_{Rx}(dB) + G_{Rx}(dB) = -163 + 7.6 + 46.5 = -108.9dBm \tag{4.5}$$

where G_{Rx} is total gain of the receiver chain. Hence it can be seen that P_{noise} is 13.9 dB less than the VNA sensitivity, consequently the receiver sensitivity is limited and defined by the VNA sensitivity, and not by thermal noise power in this case. Also it should be noted that even by adding a 6 dB attenuator at the IF port of the receiver probe, P_{noise} still remains 9.4 dB below the VNA sensitivity, therefore it does not degrade the system's dynamic range. Based on the VNA sensitivity ($-95\ dBm$) and total gain of the receiver chain (G_{Rx}) shown in Figure 4.7, the receiver sensitivity is calculated as:

$$Rx_{sensitivity} = VNA_{sensitivity} - G_{Rx} = -95dBm - 46.5dB = -141.5dBm \tag{4.6}$$

Now using the receiver sensitivity and the IF power at the transmitter probe, the required isolation between the transmitter and receiver probes' IF ports is simply calculated using:

$$\begin{aligned} \textit{Required IF Ports Isolation} &= 10\ dB + IF_{power}@Tx_{probe} - Rx_{sensitivity} \\ &= 10\ dB + 5\ dBm - (-141.5\ dBm) = 156.5\ dB \end{aligned} \quad (4.7)$$

where 10 dB was considered an acceptable margin for the required isolation. Comparing IF isolation through the cables in the SPMS setup ($> 200\ dB$, calculated in 4.2), and 4.7 it can be seen that there is sufficient isolation between IF ports through the cables.

The IF to RF port isolation in the up- and down-converter is about 110 dB at the IF frequencies. Hence, the transmitter and receiver IF ports, through the RF path (radiation from antennas) are at least 220 dB isolated at the IF frequencies. This does not include the isolation provided by the RF amplifiers and antennas. However, during a system calibration it was observed that radiation of the IF signal from the transmitter package to the receiver package is much stronger than its radiation from the antennas. This was tested by turning the LO source off, looking at the time domain response, and measuring leakage level at the same time spot of the main signal. Magnetic loaded absorber were used to cover the transmitter and receiver probes' surface and therefore reduce the surface current on the packages in order to prevent IF radiation from it. Measured pathloss at 91.8 GHz in an isolated block by mm-wave absorbers (scaled anechoic chamber) without any scatterers, before and after adding these absorbers is shown in Figure 4.8. It is shown that before covering the package surfaces, the pathloss has a 15 dB variation which is result of the interference and multipath between the RF signal and IF leakage.

Figure 4.9 shows a power delay profile of the SPMS after modification in the absence of any scatterers when the transmitter and receiver probes are placed in a mm-wave anechoic chamber. As it can be seen, the IF leakage level of the same order as the noise level, and thus does not degrade the system performance.

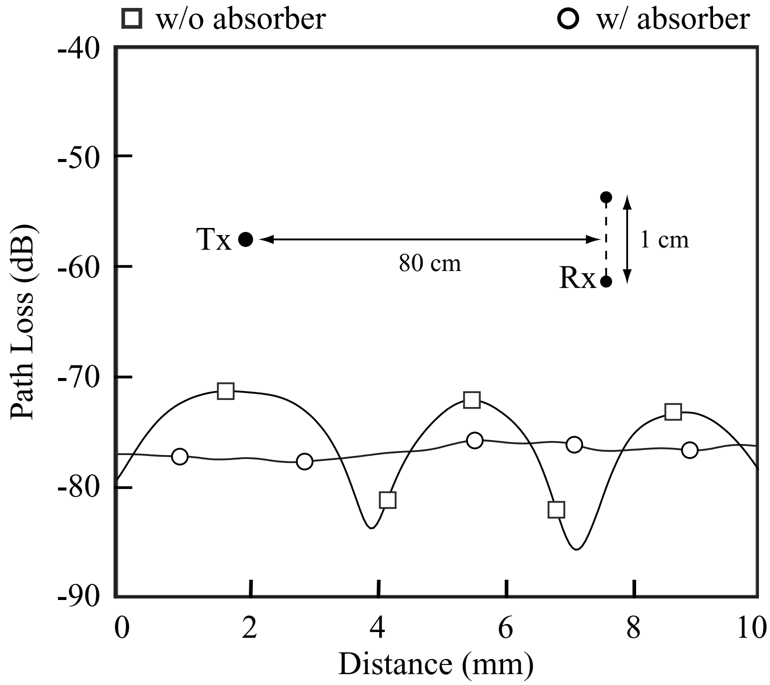

Figure 4.8: Package radiation and its effect on pathloss.

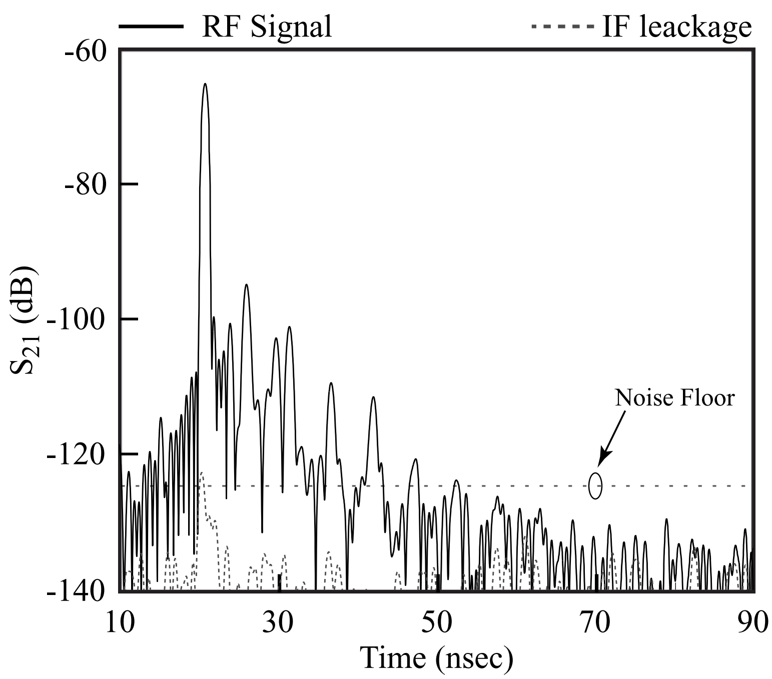

Figure 4.9: Power delay profile of modified SPMS for a through case.

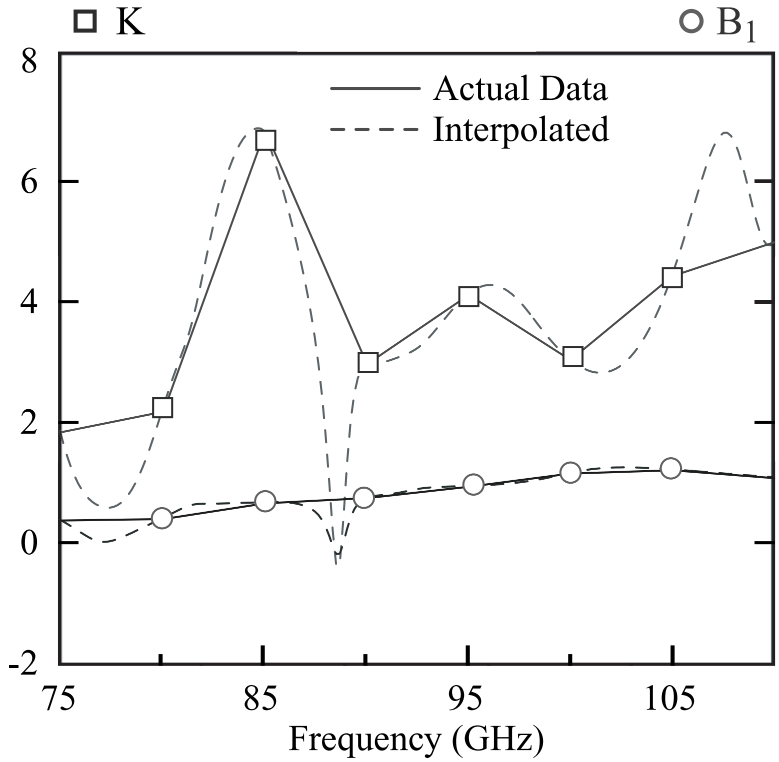

Figure 4.10: RF amplifier stability parameters.

4.2 Degradation in System Specification

Although the RF amplifier was expected to be unconditionally stable ($K > 1, B_1 > 0$) based on data provided by the manufacturer (as shown in Figure 4.10), in practice the amplifier was oscillating in its operating frequency band. The possibility of this oscillation can be seen by interpolating actual data, as shown in Figure 4.10.

$$K = \frac{1 - |S_{11}|^2 - |S_{22}|^2 + |\Delta|^2}{2|S_{11}S_{22}|} \tag{4.8}$$

$$B_1 = 1 + |S_{11}|^2 - |S_{22}|^2 - |\Delta|^2 \tag{4.9}$$

where

$$\Delta = S_{11}S_{22} - S_{12}S_{21} \tag{4.10}$$

Many experiments were performed to stop the oscillation of the RF amplifier, however none of them were successful. Also due to a limited number of available amplifiers (70LN3A is an outdated product of HRL) it was not beneficial to characterize the RF amplifier and redesign whole circuit in order to take this imperfection into account and provide the RF amplifier input and output impedance, in its stable range. Hence the actual receiver used for measurements does not have the RF amplifier and consequently its sensitivity was decreased by 20dB.

CHAPTER 5

A Physics based Site Specific Channel Model using 3D Ray-Tracing

A pre-developed [1] deterministic channel model based on a 3D ray-tracing algorithm and the physics of the environment is extended and used as a simulation tool to predict communication channel parameters such as power delay profile, pathloss, angle of arrival/departure and coverage. This model is used against the measured results obtained from the SPMS. High frequency wave propagation phenomena such as reflection, transmission, diffraction and absorption are accommodated in a systematic manner. The fundamental assumption in the ray-tracing algorithm is that all scatterers in environment are considered to have dimensions much larger than wavelength. The model is generally applicable to any arbitrary environment with pyramidical dielectric or metallic objects such as building structure, interior walls, etc. Dielectric properties of the materials (ε_r, σ) are considered as well.

Determination of field quantities is made on the basis of coherent vector summation of all rays that arrives at the observation point through various paths. Geometrical optics (GO) and a modified uniform theory of diffraction (UTD) are applied successively starting from the source until the ray arrives at the receiver. Relative complex dielectric permittivity,

[1] This model was developed as my M.Sc. thesis in University of Tehran and later was expanded for wave propagation modelling in tunnels and subways

conductivity and material thickness are stored and used as the main parameters of any reflecting surface and diffracting wedge. Unless specified otherwise it is assumed that all reflecting surfaces are planar and smooth. The surface roughness effects can be included using a probabilistic model for the surface profile. Antenna effects such as directivity and the polarization can be chosen arbitrarily. Reflection, transmission and diffraction coefficients used in this model are in matrix form and thus the polarization of the reflected and diffracted rays are taken into account.

In what follows, first the algorithm for the wave propagation simulation code is briefly introduced and then few examples demonstrating behavior of wave propagation for urban and suburban areas are presented. In last section a space-time focusing algorithm based on 3D ray-tracing applicable for through wall imaging at microwave frequencies is presented.

5.1 Fundamentals of Ray-Tracing Algorithm

Ray-tracing is an efficient tool for analytical prediction of wave propagation in large and complex random media with large scatterers (compared to the wavelength). It has been increasingly used for wireless channel characterization in recent years. Considering the complexity of problem with thousands of scatterers in a typical urban scenario and millions of interactions between rays and scatterers, there are a number of issues which should be dealt with cautiously. As starting point and in order to define the ray-tracing scheme an important parameter which should to be chosen according to the environmental features and the sought accuracy accuracy is the *angular resolution* of the transmitted rays, which is defined as angular difference between adjacent rays transmitted from source. In this simulator, angular resolution, α, is determined by 1) minimum feature size of the environment under consideration, D_{min}, and 2) maximum path length that a ray may travel,

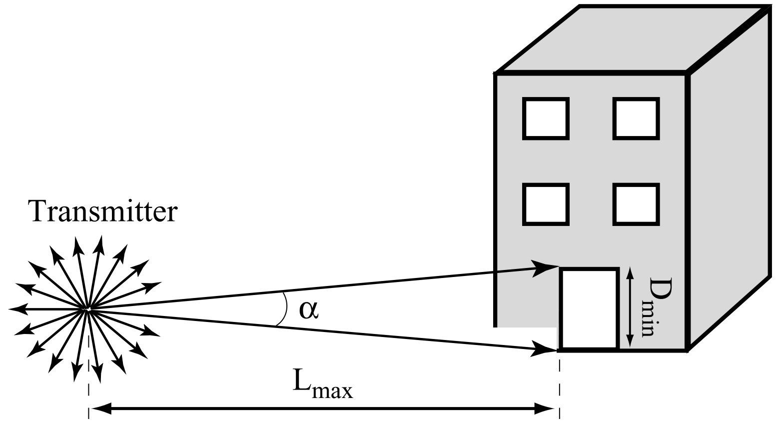

Figure 5.1: Defining angular resolution based on the resolution of scene and maximum ray length.

L_{max}, before its power drops below the receiver sensitivity (see Figure 5.1).

$$\alpha = 2\arctan\left(\frac{D_{min}}{2L_{max}}\right) \tag{5.1}$$

As it can be seen in Figure 5.1 D_{min} it is data resolution which user has selected for the scene and is not necessarily smallest dimension in the scene. The upper and lower limits of L_{max} can be estimated using 1) Friis formula when assuming no reflection, diffraction or penetration through objects happens for the ray (5.2), and 2) maximum distance between transmitter and objects in the scene.

$$L_{max} = \frac{\lambda}{4\pi}\sqrt{\frac{P_T}{P_{R,min}}} \tag{5.2}$$

where P_T and $P_{R,min}$ are transmitter power and receiver sensitivity respectively. As shown in Figure 5.2 , equal angular resolution in azimuth and elevation planes will result in nonuniform ray tubes facets (F_1, F_2) which is not computationally efficient. Hence a nonuniform angular resolution (5.3) is selected in azimuth plane such that ray tubes are nearly uniform.

$$\Delta\varphi = \frac{\Delta\theta}{\sin\theta} \tag{5.3}$$

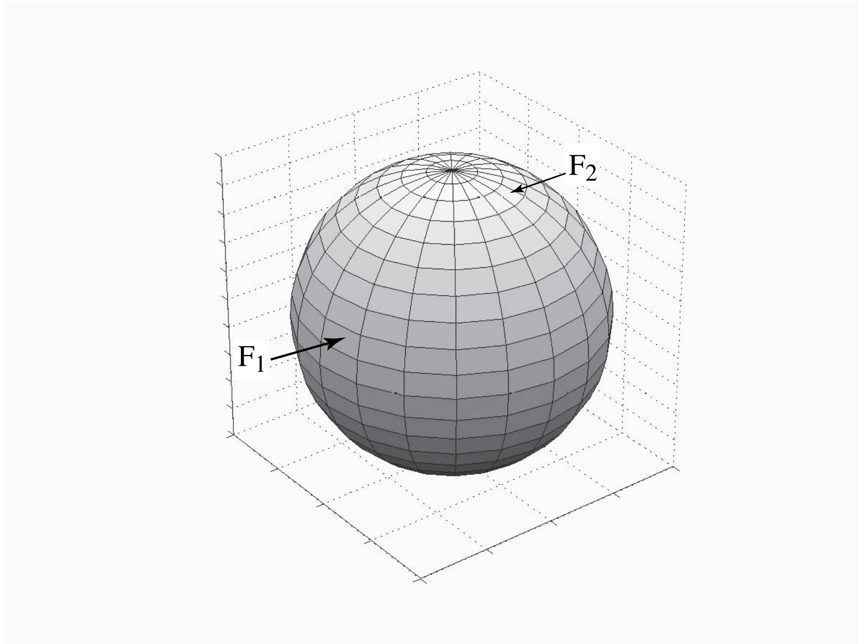

Figure 5.2: Nonuniform ray tube facets due to uniform angular resolution.

Simulation time is a major issue for a dense urban (indoor or outdoor) environment specially for a full 3D simulator. In order to increase simulation speed, an intelligent technique has been applied in 3D ray-tracing algorithm. Any ray generated from a source point (transmitter, reflection, diffraction, ...) will interact only with $1/8$ of the space around it which is selected based on the direction of the ray. As it is shown in Figure 5.3 this technique reduces the number of objects under consideration at each step in average by factor of 8 simply by looking at the objects which fall in subspace along the direction of the ray. The same assumption is made when checking for ray interaction with a given receiver.

Many ray-tracers base the decision on when to disregard a ray, at least in part, on the number of reflections or diffractions that a ray undergoes. In a highly scattering environment, this number must be set fairly high, as it is more likely that the dominant ray path will be one with significant reflections. This is inefficient however, as many rays, whose power levels have dropped below the receiver sensitivity, will continue to be traced. Basing the criteria for disregarding a ray solely on its power level (usually set to the expected receiver

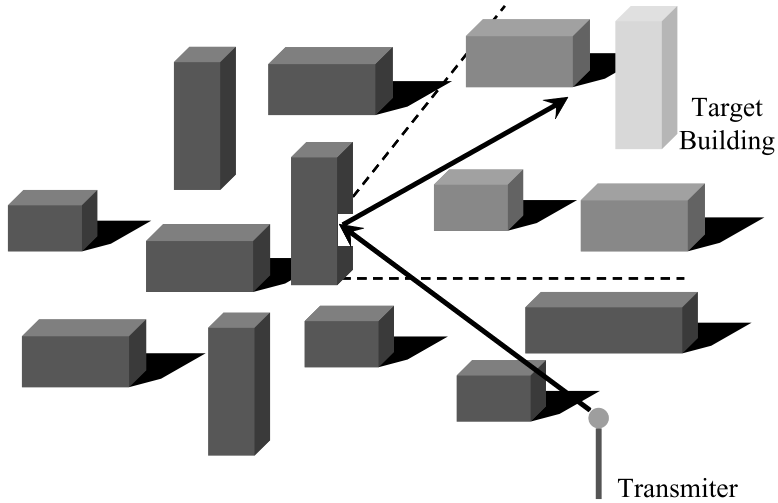

Figure 5.3: Reduction in the number of objects considered for each intersection by intelligent ray-tracing.

sensitivity), will result in maximum efficiency in the ray tracing algorithm, both in terms of accuracy and simulation run time. Figure 5.4 shows a simplified version flowchart of the 3D ray-tracing algorithm.

5.2 Wave Propagation Phenomena

5.2.1 Reflection, transmission and diffraction

Reflection and transmission coefficients have a great effect on the accuracy of the numerical results. Hence the matrix from of these coefficients for multi-layer object have been used which considers polarization as well as material parameters (ε_r, σ) and thickness of each layer (see appendix A). The objects can be defined penetrable or impenetrable and also as shown in Figure 5.5 there are two kinds of penetrable objects, solid or hollowed.

High frequency asymptotic techniques are successfully used to evaluate the field scattered from an object when the electromagnetic field wavelength is small compared to the significant dimensions of the object itself. Two such techniques that have received considerable attention in the past are the geometrical theory of diffraction (GTD) and the uniform

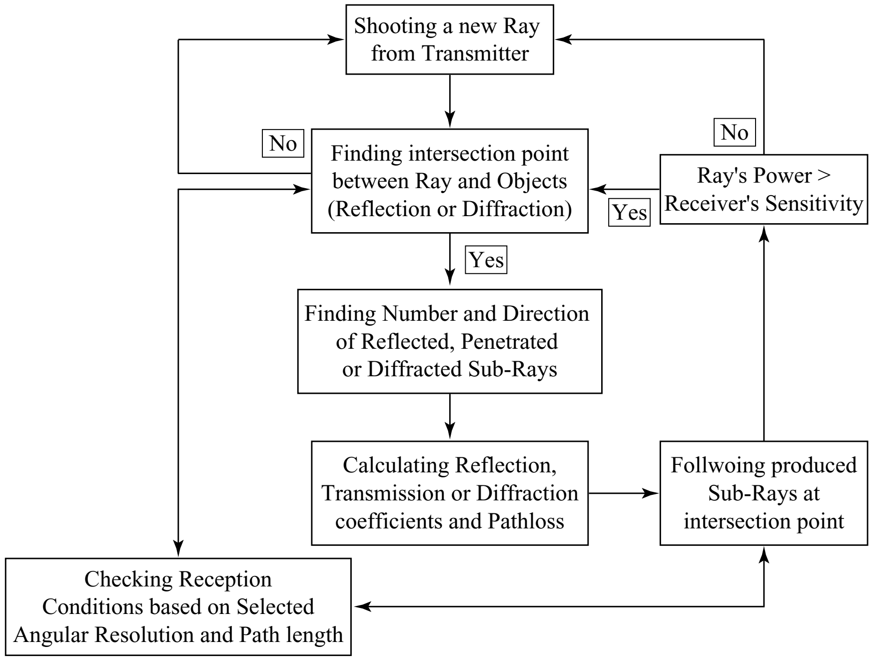

Figure 5.4: Ray-tracing flowchart.

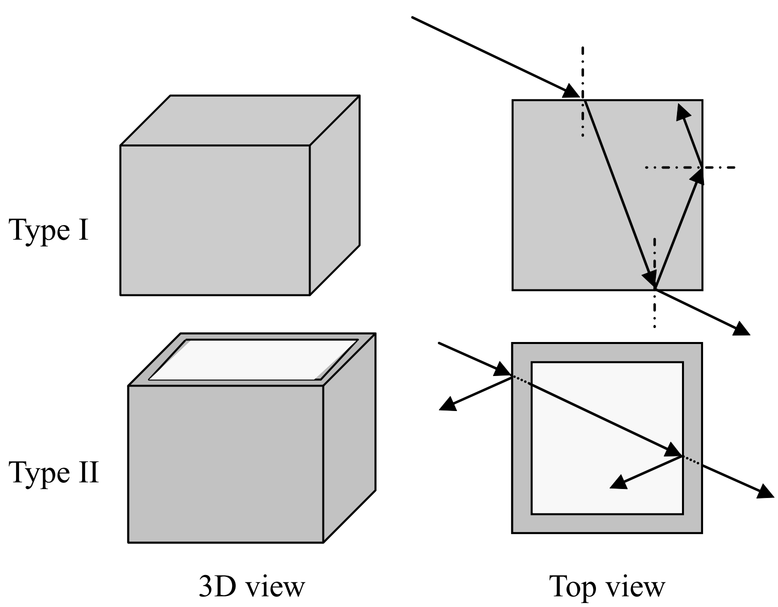

Figure 5.5: Penetrable objects.

theory of diffraction (UTD) [49, 50]. Since exact analytical solutions for the diffraction coefficients of penetrable wedges are not available, heuristic UTD diffraction coefficients have been introduced [51–54]. Here we use a three-dimensional heuristic diffraction coefficient to predict the electromagnetic field scattered from vertical and horizontal impedance wedges. The model is based on a modification of the two-dimensional solution [52]. For the parameters shown in Figure 5.6 diffracted filed field can be written as:

$$E_{UTD} = E_0 \frac{e^{-jks'}}{s'} D_{\parallel}^{\perp} \sqrt{\frac{s'}{s+s'}} e^{-jks} \tag{5.4}$$

where $D_{\parallel}^{\perp}$ is UTD diffraction coefficient for impedance wedges and is defined as following.

$$D_{\parallel}^{\perp} = \frac{e^{-j\pi/4}}{2n \sin\theta_0 \sqrt{2\pi k}} \times (D_1 + D_2 + D_3 + D_4) \tag{5.5}$$

where D_i ($i = 1 \rightarrow 4$) are defined by 5.6 to 5.9.

$$D_1 = \cot\left(\frac{\pi + (\varphi - \varphi')}{2n}\right) F\left(kLa^{+}(\varphi - \varphi')\right) \tag{5.6}$$

$$D_2 = \cot\left(\frac{\pi - (\varphi - \varphi')}{2n}\right) F\left(kLa^{-}(\varphi - \varphi')\right) \tag{5.7}$$

$$D_3 = R_0^{\perp,\parallel} \cot\left(\frac{\pi - (\varphi + \varphi')}{2n}\right) F\left(kLa^{-}(\varphi + \varphi')\right) \tag{5.8}$$

$$D_4 = R_n^{\perp,\parallel} \cot\left(\frac{\pi + (\varphi + \varphi')}{2n}\right) F\left(kLa^{+}(\varphi + \varphi')\right) \tag{5.9}$$

$R_n^{\perp,\parallel}$ and $R_0^{\perp,\parallel}$ are reflection coefficients from wedge's faces for vertical and horizontal polarizations. $a^{\pm}$ $\beta^{\pm}$, L, and F (Fresnel function) are given by.

$$a^{\pm}(\beta) = 2\cos^2\left(\frac{2n\pi N^{\pm} - \beta}{2}\right) \tag{5.10}$$

$$\beta^{\pm} = \varphi \pm \varphi' \tag{5.11}$$

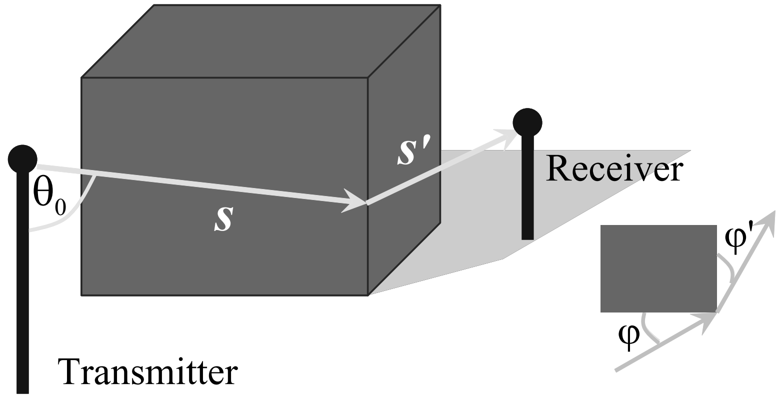

Figure 5.6: Diffraction from impedance wedges.

$$L = \frac{ss'}{s+s'}\sin^2\theta_0 \tag{5.12}$$

$$F(x) = 2j\sqrt{x}e^{jx}\int_{\sqrt{x}}^{\infty} e^{-j\tau^2} d\tau \tag{5.13}$$

and $N^{\pm}$ are integers that most nearly satisfy the following equations.

$$2\pi n N^{+} - (\varphi \pm \varphi') = \pi \tag{5.14}$$

$$2\pi n N^{-} - (\varphi \pm \varphi') = -\pi \tag{5.15}$$

$$n = \frac{2\pi - \alpha}{\pi} \tag{5.16}$$

α is interior wedge angle.

5.2.2 Antenna Pattern

Antenna pattern determines the direction of wave propagation and consequently affects the channel parameters. Usually waiting transmitted and received rays based on the transmitter and receiver antenna patterns is done during simulation. Hence simulation results for a specific antenna can not be used for another type. Here in order to minimize total simulation time, initially channel parameters are calculated based on the isotropic antennas and the angle of arrivals and departures are stored in primary data files. Then the effect of

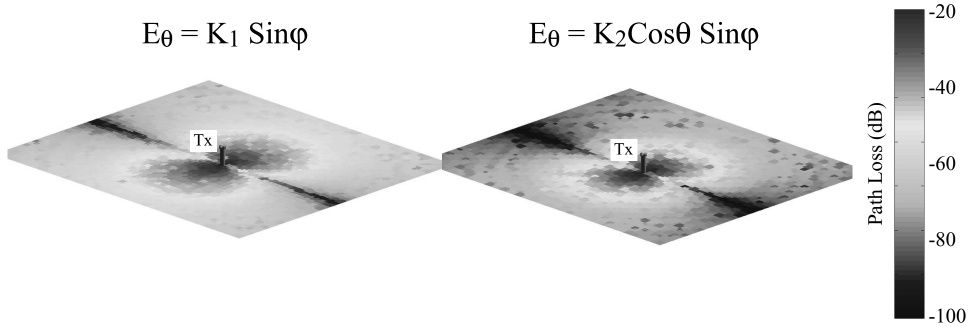

Figure 5.7: Effect of antenna pattern on coverage.

the antenna patterns (transmitter and receiver) are applied by post processing the primary data and using desired antennas. This process can be repeated for any antenna with no need to run the simulation again. Figure 5.7 shows the coverage in an open flat area for two types of transmitter antenna with similar receiver antenna.

5.3 Examples

In this section few examples for different environments are shown to demonstrate the capabilities of our channel simulator and its features.

5.3.1 Urban Areas

Outdoor

A simplified model of University of Michigan central campus shown in Figure 5.8 is selected as an example for urban/outdoor area. Figure 5.9 shows pathloss for path $A \rightarrow B \rightarrow C$ shown in Figure 5.8. As it can be seen vector (field) summation will result in few dB higher pathloss due to phase difference between received signal from different paths, hence it is necessary to maintain the phase for more accurate estimation. Simulation has been done at 1 GHz for a vertically polarized transmitter, and buildings are assumed to be penetrable solid box (type I) with $\varepsilon_r = 6$ and $\sigma = 0.005\ S/m$, receiver sensitivity has

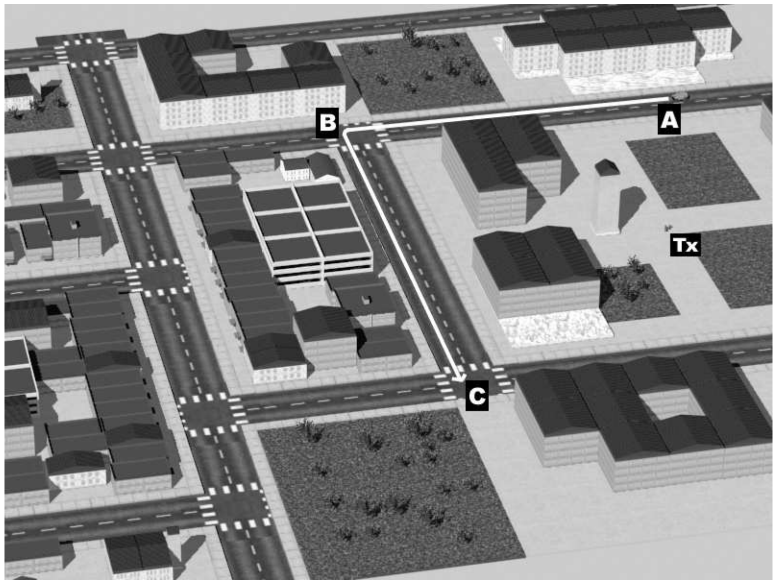

Figure 5.8: Simplified model of University of Michigan central campus.

been set at -90 dBm and transmitter power was 1 Watt. Power delay profile and direction of arrivals for receiver at position ”B” are shown in Figures 5.10 and 5.11 respectively. Finally coverage for the whole scene is shown in Figure 5.12.

Indoor

Since a full 3D ray-tracing algorithm has been developed and used in the physics based model, which was presented in the previous section, the model can be applicable for indoor scenarios as well as outdoors. For indoor scenarios one of the dilemma is the extent of details that must be considered in simulation in order to predict accurate result while running time remains reasonable. Hence in this section two examples which have been done in order to investigate these effects are presented.

Example 1. For first example, signal coverage inside a two stories covered parking structure which its first floor is shown in Figure 5.13 were predicted for two different types of car's model. As it can be seen in Figure 5.14 the simple car's model is only a rectangular cube covering the car, while the complex model is made up of 77 pieces of metal and absorbers that approximately shape a car. Figures 5.15 and 5.16 compare signal coverage

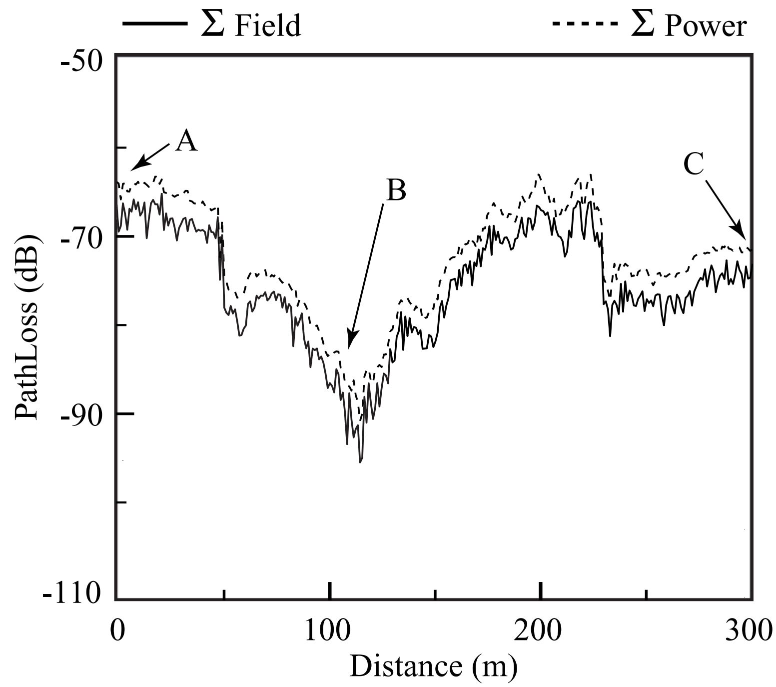

Figure 5.9: Pahloss for path A-B-C shown in Figure 5.8.

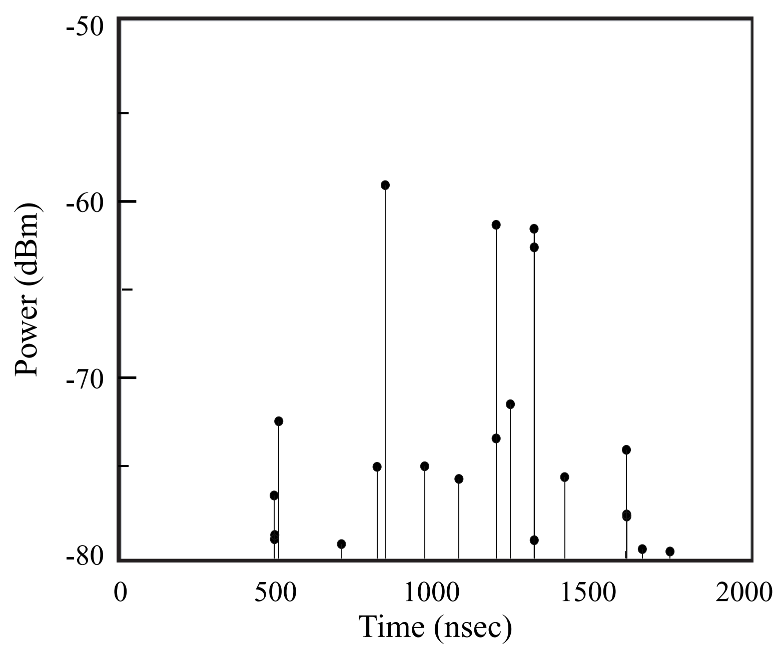

Figure 5.10: Power delay profile for position *B* shown in Figure 5.8.

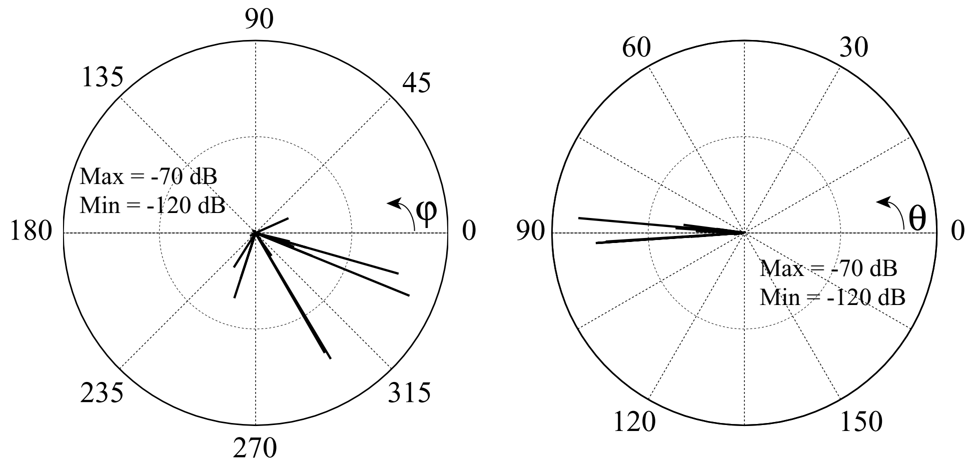

Figure 5.11: Direction of arrivals for position *B* shown in Figure 5.8.

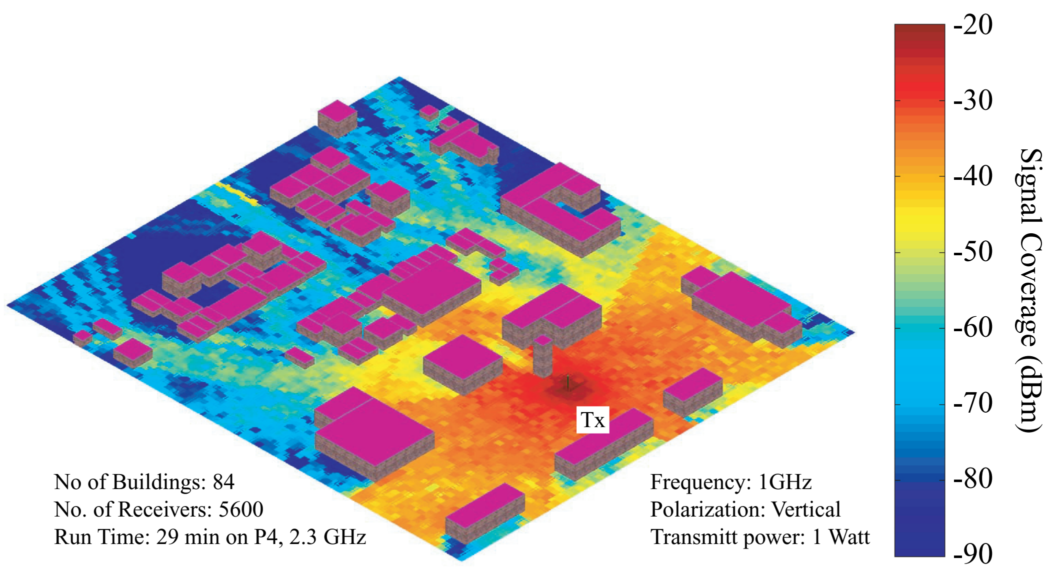

Figure 5.12: Signal coverage calculated for scenario shown in Figure 5.8.

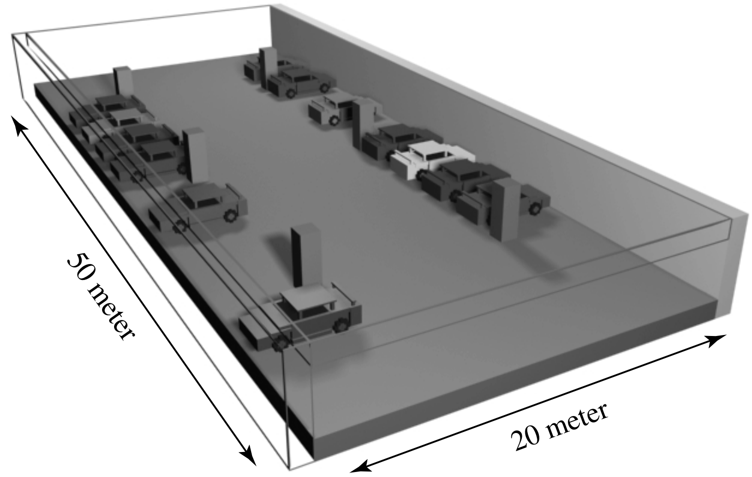

Figure 5.13: A covered parking structure.

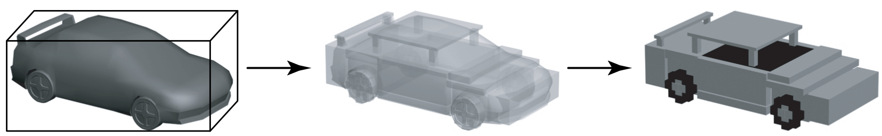

Figure 5.14: Car modelling by discretization to canonical objects.

at the first floor of the parking when transmitter is in the first and second floor respectively, for two types of car's model. It can be seen when the transmitter is in the same floor as the receivers the difference in signal coverage due to model used for the cars varies from $-20\ dB$ to $10\ dB$, however this difference increases ($-30\ dB \rightarrow 30\ dB$) when the transmitter and receivers are in different floors. This can be translated as when the transmitter and receivers are in same floors there are many short paths (strong rays) between transmitter and receivers which dominates the effect of subrays related to the difference in the car models. However when the transmitter and receivers are in different floors the number of strong rays between transmitter and receivers decreases hence the effect of the subrays becomes more significant.

Example 2. For the second example of indoor scenario, an outdoor-indoor case has

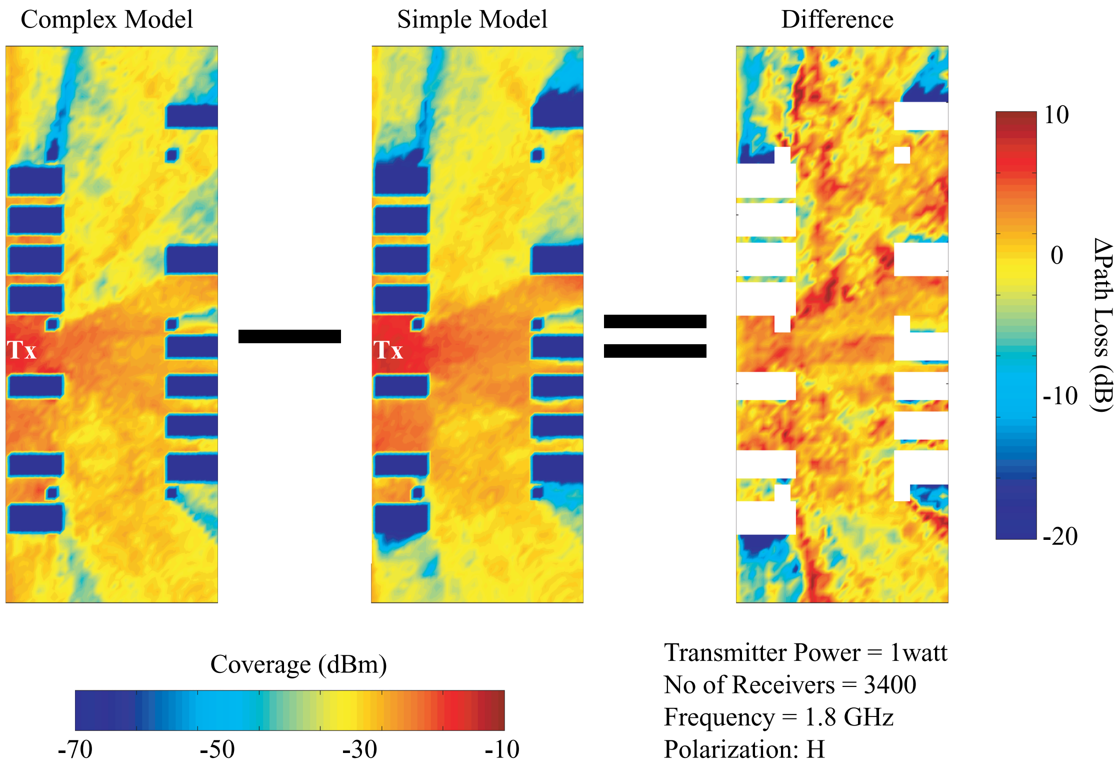

Figure 5.15: Signal coverage inside the covered parking structure shown in Figure 5.13 for two different car models (Tx at 1st floor).

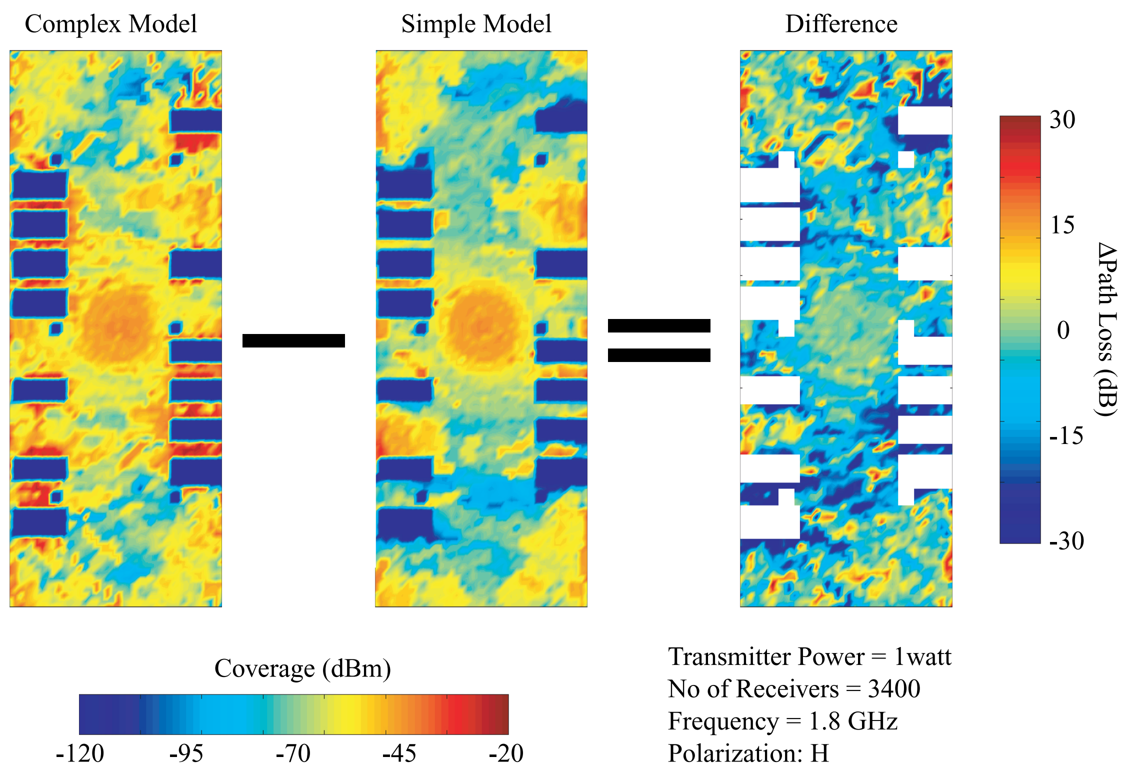

Figure 5.16: Signal coverage inside the covered parking structure shown in Figure 5.13 for two different car models (Tx at 2nd floor).

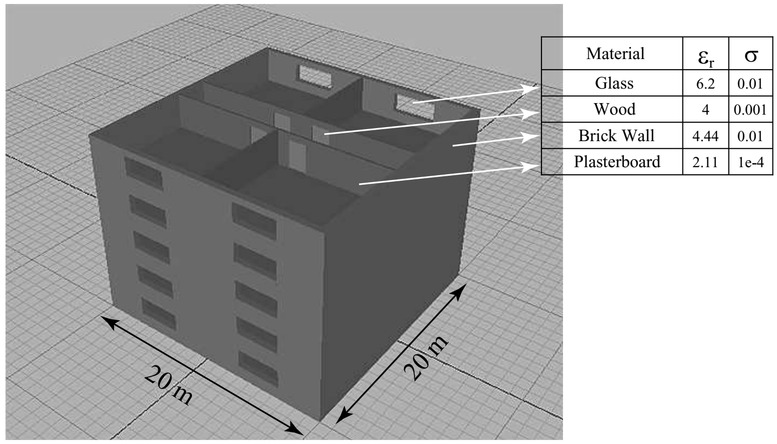

Figure 5.17: A five stories building.

been considered. Using a five stories building shown in Figure 5.17 an apartment complex shown in Figure 5.18 was designed. Transmitter was placed on the top of building *A* and receivers are in the 4^{th} floor of the building *B* and the 5^{th} floor of the building *C*. Signal coverage for one watt transmitted power in the 4^{th} and 5^{th} floors of the building *B* and *C* respectively, are shown in Figure 5.19.

In order to investigate effect of adjacent buildings' interior on signal coverage in specified buildings. Signal coverage was calculated in a simplified model of the apartment complex shown in Figure 5.20. As shown in Figure 5.20 number of objects are five times less than actual scenario in Figure 5.18, consequently simulation time was four times faster (45 sec instead of 180 sec). Figure 5.21 shows difference in predicted results between actual scenario and the modified model. As it can be seen the predicted results for coverage inside building *C* are similar while results for building *B* are significantly different. This is due to the different distance between transmitter and the target buildings, when transmitter is close to the target building (such as building *B* in this case) reflected waves from interior of the adjacent buildings are strong enough enough to penetrate inside the target building and affect signal coverage. In the simulation results shown in Figures 5.19 and 5.21 diffraction was not considered as usually it does not have significant effect for indoor propagation. To evaluate this assumption signal coverage was computed with considering

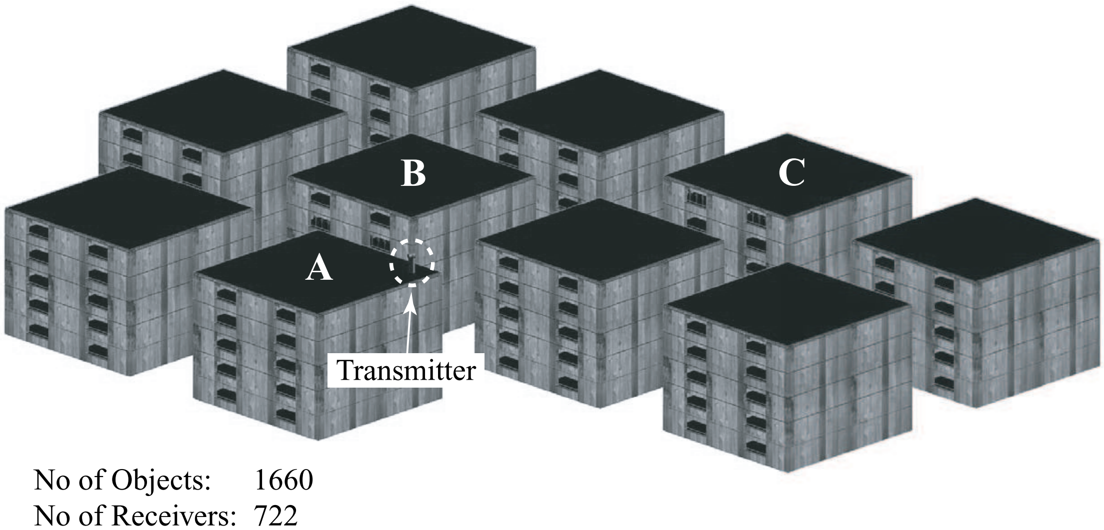

Figure 5.18: An apartment complex.

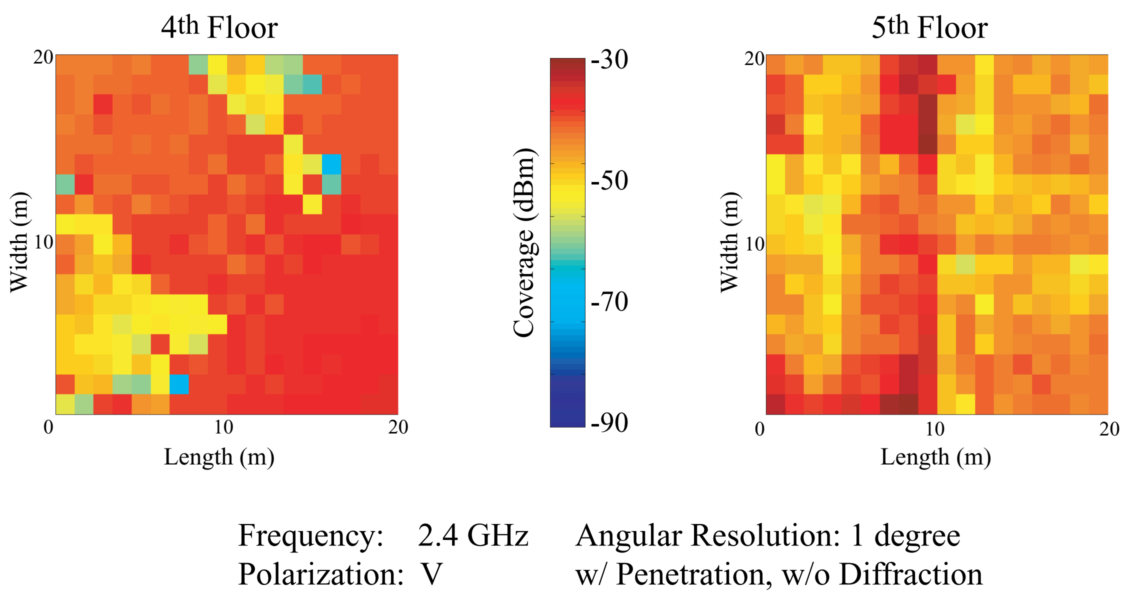

Figure 5.19: Signal coverage inside buildings *B* and *C* shown in the Figure 5.18.

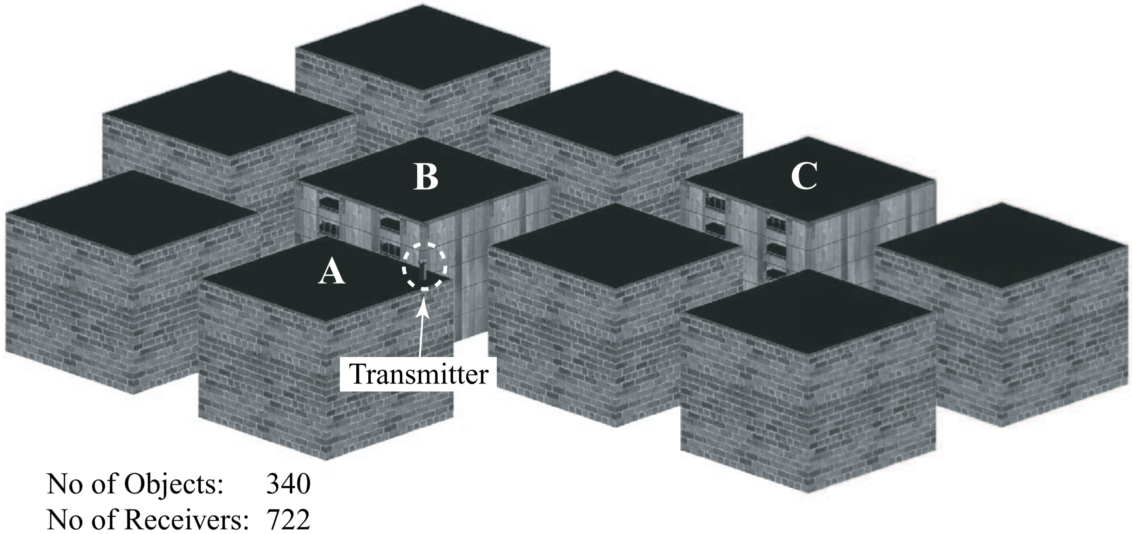

Figure 5.20: Simplified model of apartment complex shown in the Figure 5.18.

diffraction effect into account. Figure 5.22 shows difference in predicted signal coverage due to diffraction effect, and as it can be seen the change is negligible specially considering simulation time which is much longer (4 times in this case) by considering diffraction.

As it was discussed in section 5.1, angular resolution indirectly is defined based on system dynamic range (transmitter power - receiver sensitivity) and the size of propagation site. For the example shown in Figure 5.20 using the rules discussed in section 5.1 required angular resolution ($\Delta\theta$) is 0.1 degree. In order to investigate convergence of ray-tracing algorithm we defined relative error due to coarse ray resolution as:

$$Error_{ndB} = \frac{No.\ of\ |P_i - P_{i-1}| \geq n\ dB}{Total\ No.\ of\ Receivers} \tag{5.17}$$

where P_i and P_{i-1} are received power by a receiver for new and previous angular resolution

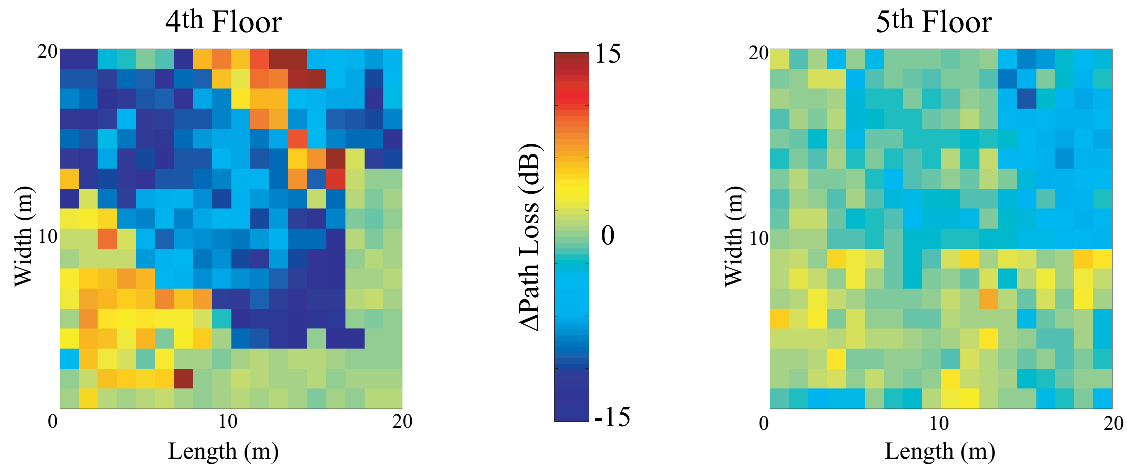

Figure 5.21: Difference in signal coverage between actual and simplified models.

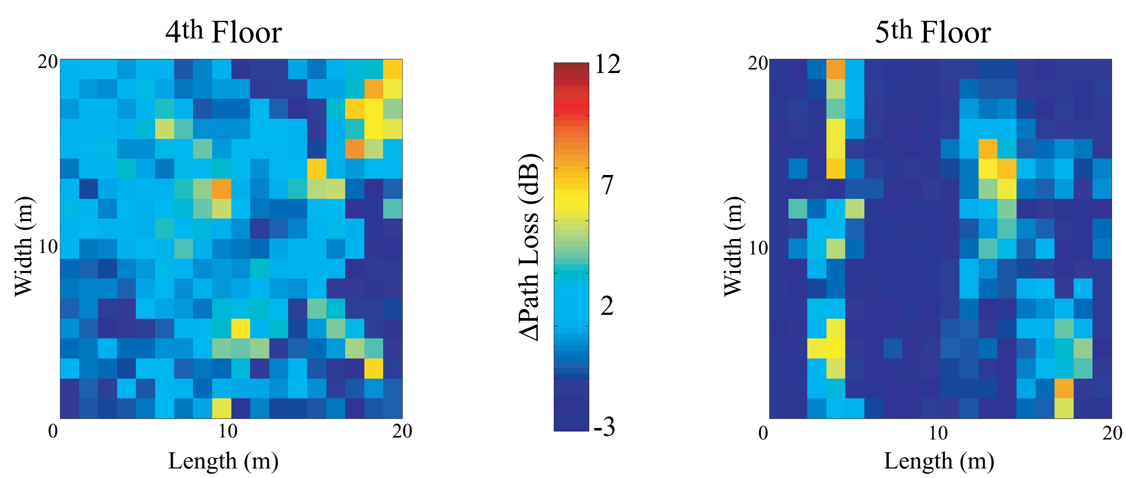

Figure 5.22: Difference in predicted signal coverage due to diffraction effect.

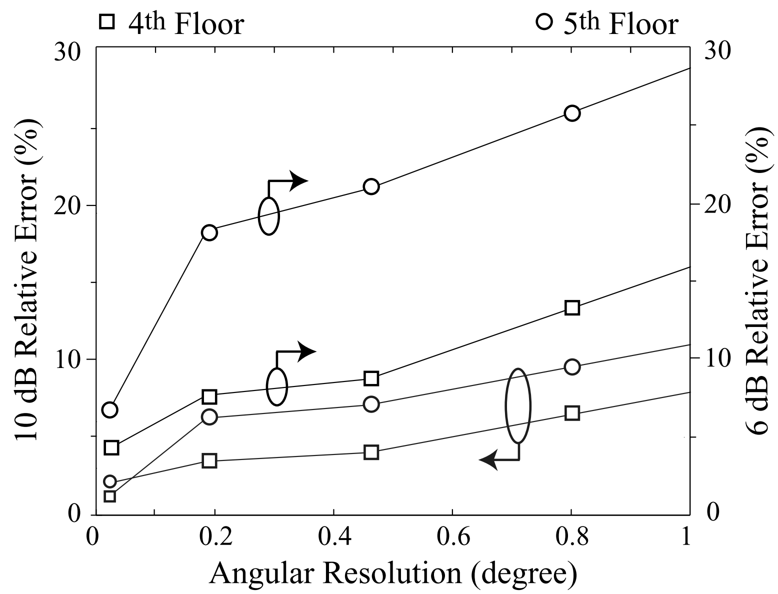

Figure 5.23: Relative error in predicted results vs. angular resolution.

respectively. Figure 5.23 shows how 6 dB and 10 dB relative errors are decreasing and simulation results are converging to their final value with increasing angular resolution. As in 3D ray-tracing total number of the rays is inversely proportional to square of angular resolution, simulation time is expected to vary with the same rate. Figure 5.24 shows simulation time for example shown in Figure 5.20 for few angular resolution and fitted curve ($\frac{k}{x^2}$).

5.3.2 Suburban Areas

In last few years there have been numerous studies done on wave propagation characterization in urban areas for wireless communication applications. However, there is little in the literature [55–57] on wireless channel modelling in rural areas. Because of the complexity of wave propagation phenomena in forested environment all of the previous works in this area are based on simple approximations and have a narrow range of application. For broadband and commercial systems in suburban areas usually there is a base station tower that provides a LOS path or a path with one reflection and/or diffraction, and therefore predicting the coverage is straightforward. However for military applications the situation is

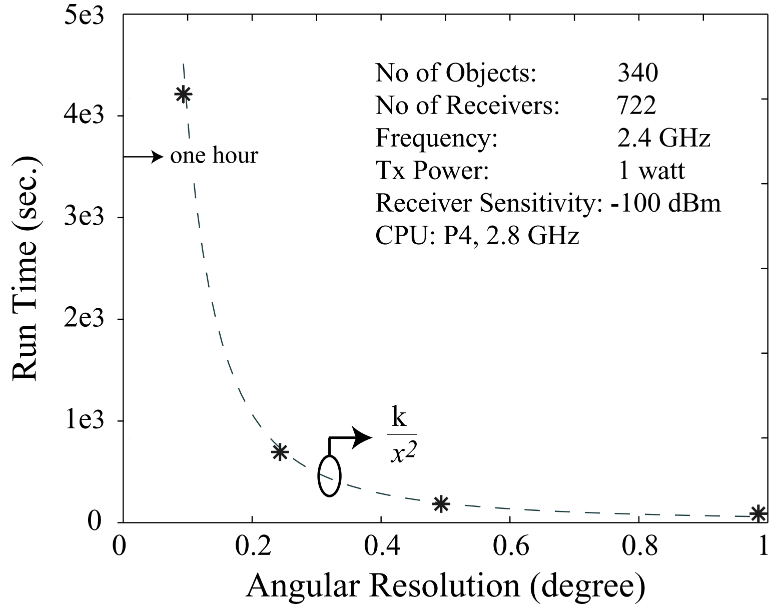

Figure 5.24: Simulation time vs. angular resolution.

more difficult as there is usually no LOS and propagation will be through forest and adjacent buildings or over hills, with multiple reflection and diffraction from terrain and other objects. Figure 5.25 shows a typical suburban area which is around 3 km^2 wide with 25 m^2 resolution. In order to demonstrate the effect of terrain on signal coverage, simulation were performed with and without terrain separately and results are shown in Figures 5.26 and 5.27. As it can be seen ignoring the effect of terrain will result in optimistic estimation of the signal coverage in shadow regions such as behind hills and in valleys, which the only path is diffracted signal over the hills.

5.4 Through Wall Imaging at Microwave Frequencies

5.4.1 Introduction

Imaging inside of buildings to detect human signature has become a problem of great importance to law enforcement agencies. Existing technology based on infrared cameras, although can provide high resolution images, has limited applicability to situations where

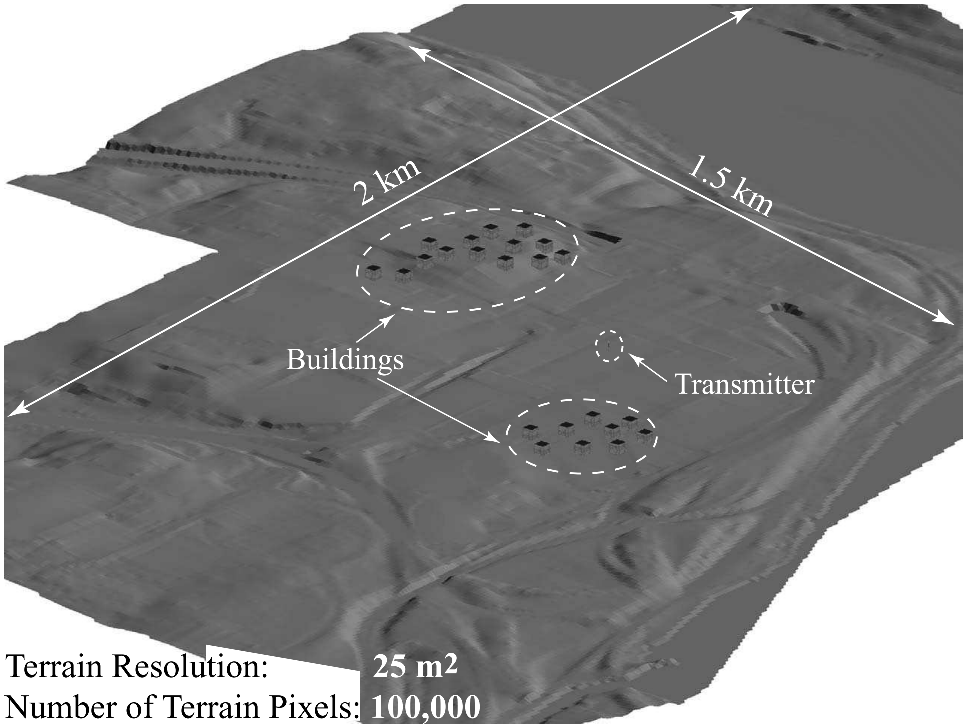

Figure 5.25: A typical suburban area.

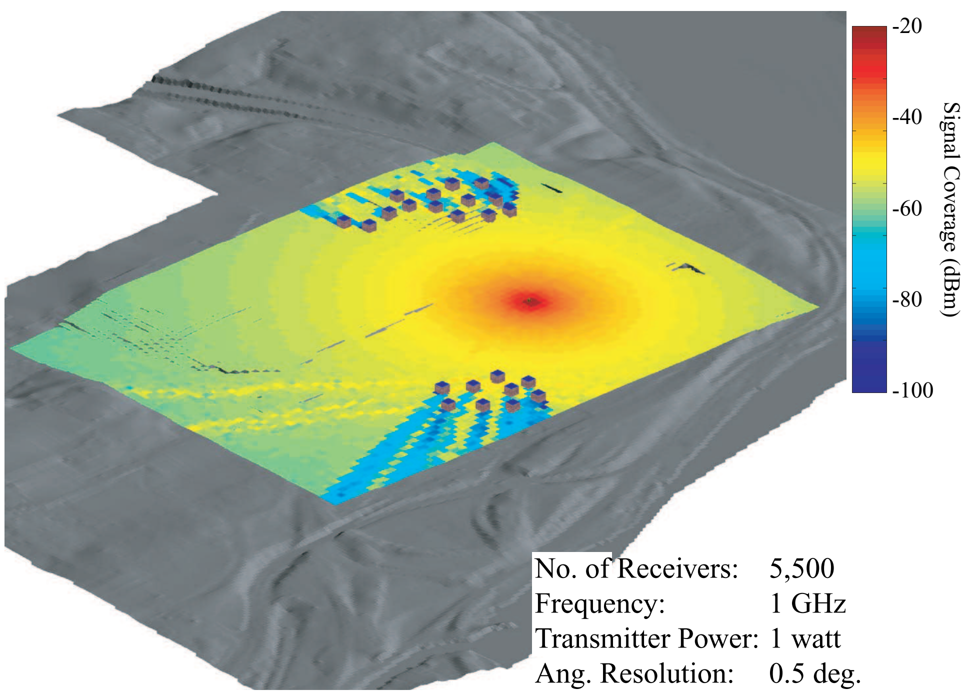

Figure 5.26: Predicted signal coverage without effect of terrain.

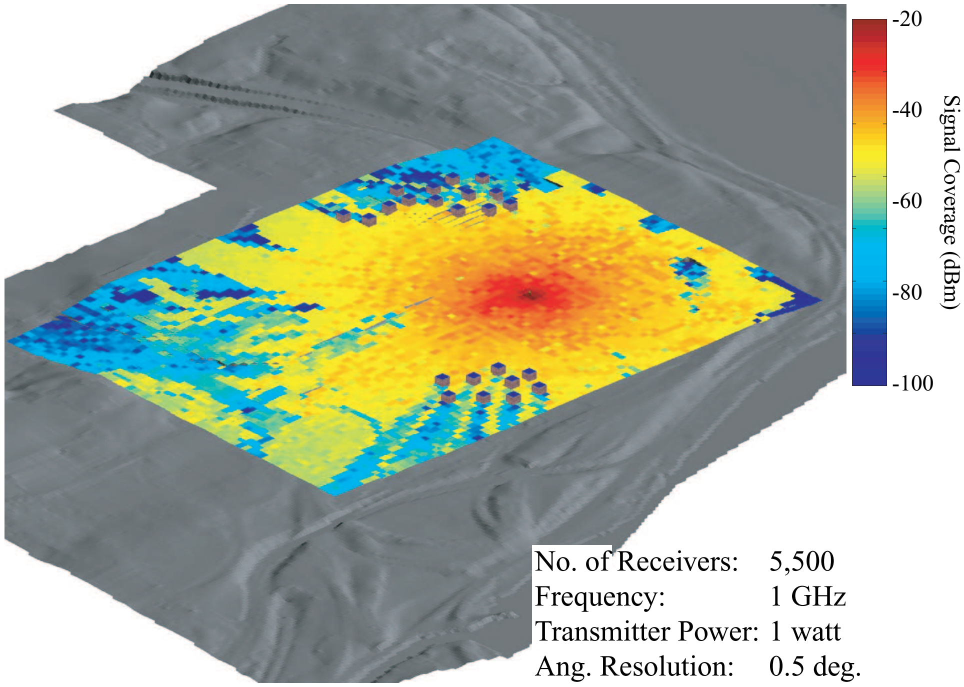

Figure 5.27: Predicted signal coverage with effect of terrain.

the building opacity is low. Therefore imaging is only possible through thin non-absorbing material such as imaging through curtains and single walls without insulations, etc. Electromagnetic (EM) spectrum in the range of 100MHz-100GHz offers a unique opportunity for mapping of an unknown area including interior of a building because of its penetration capability through building materials. While the real part of the relative dielectric constant of non-metallic building materials at VHF through W-Band ranges from 2-4 and their loss tangent is of the order of 0.1 or less, human body present certain unique features as a scatterer of EM waves, because of its very high dielectric constant. In addition characteristic voluntary and involuntary movements affecting scattered signal such as Doppler shift, could be exploited for detection and identification. In this paper a physics based wave propagation simulation tool is employed to investigate the phenomenology of wave propagation inside complex building structures such as statistics of path loss, angel of arrival, spatial and spectral field coherence, etc. In addition the application of a space-time focusing method for detecting objects inside a building is examined. The focus of this investigation is mainly on the forward problem to better understand the physics of the problem which can be utilized to simplify the inverse problem. The result of this study will be used in the development of novel radar-based detection algorithms as well as detection methods based on multi-modality.

5.4.2 Imaging Algorithm

At low microwave frequencies, scattering and attenuation of EM waves through buildings and vegetation is relatively low. Hence the signal will survive over relatively long distances in an urban environment. Although the backscatter signal level may be sufficiently above the noise level, target detection and location in a highly scattering environment, where the signal between a target and radar may experience many reflections and diffractions, is not straightforward. To remedy this difficulty a multi-static sensor configuration is considered. In this approach an ad hoc array of cooperative transceivers is proposed. Assuming the locations of the transceiver nodes can be determined using a combination of differential GPS and laser triangulation, the backscatter and multi-static responses of the scene can be generated. The delay profiles obtain from this array of sensors can be used in an inverse scattering algorithm to generate the radar image of the scene. Time reversal methods can offer a unique opportunity for solving the inverse scattering problem of EM wave propagation and focusing in a spatially varying (inhomogeneous) medium.

While the concept of time reversal to focus waves in spatially varying media is new to the field of EM wave propagation, it has been applied in the area of acoustic and ultrasonic for several years [58–60]. The basic premise is quite simple. Let an impulse source (in time and space) be transmitted into some general inhomogeneous medium, and the tangential surface fields determined on a closed surface surrounding the impulse. It can be shown mathematically that if these surface fields are conjugated and re-radiated in time reversed sequence, that the incoming wave, generated by the surface fields is identical to the outgoing wave, and the returning energy focuses on the original source point. This is an appli-

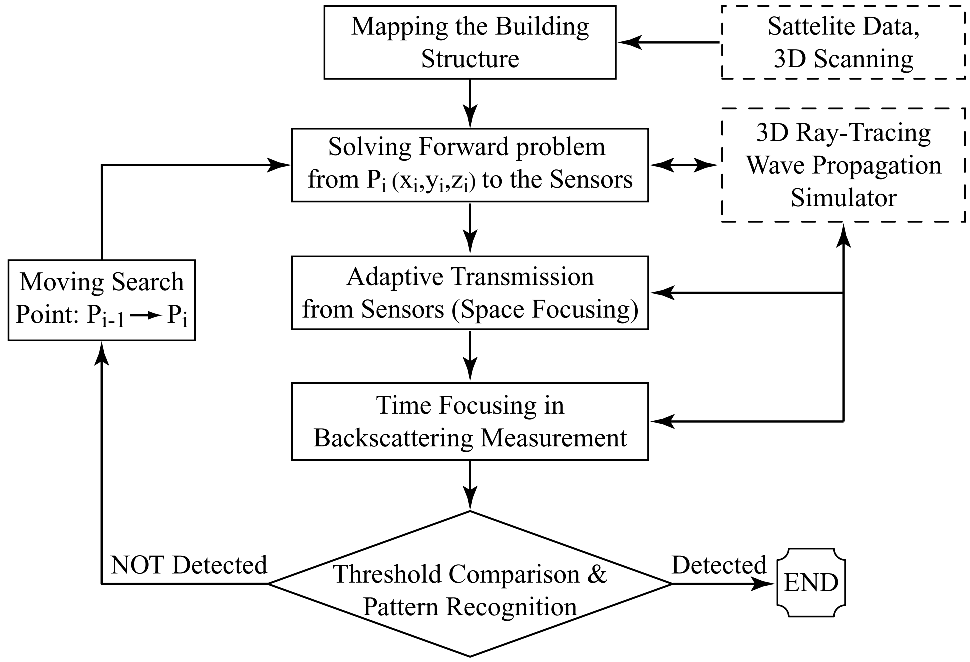

Figure 5.28: Flowchart of through wall imaging method.

cation of reciprocity and can be shown to be similar to a matched filter commonly applied in radar and communications. In any finite size array that occupies a limited spatial area the system is diffraction limited, however, it is shown that in an inhomogeneous medium a time reversal array is not always diffraction limited and can achieve super-resolution as the scatterer in the vicinity of the transmitter array and the focal point increases. As shown in Figure 5.28, the imaging algorithm is constructed of four major tasks: 1) Mapping the building structures, 2) Solving forward scattering problem, 3) Space focusing by adaptive transmission from transceivers, and 4) Time focusing for measuring backscattering. In this study it is assumed that the building structure is known.

5.4.3 Forward Scattering Problem

A typical scenario considered for through wall imaging can be viewed as a combination of outdoor-indoor environment which can potentially create an extreme multipath environment for the wave propagation. In these scenarios usually the direct paths between target and detectors are not the dominant paths. Therefore forward propagation problem must

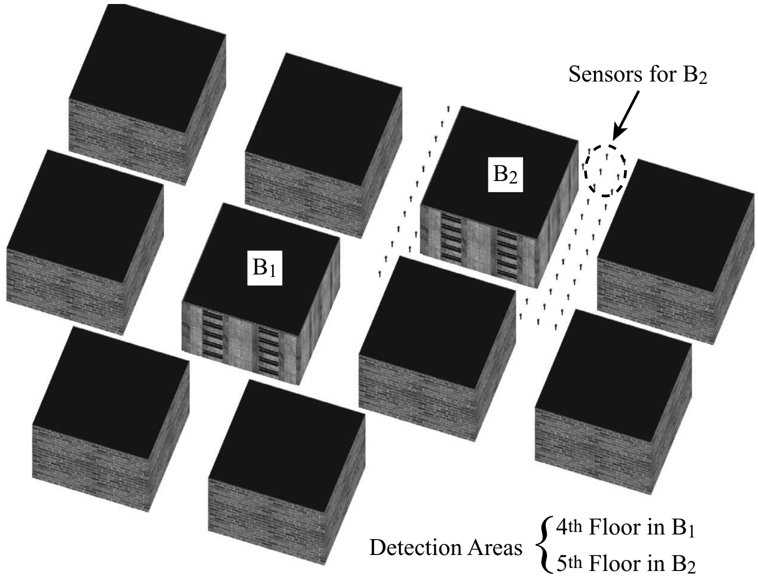

Figure 5.29: A typical scenario used in simulation.

be solved to find the optimum transmission paths between the target and the detectors. Each of these paths may include few reflections, transmissions and diffractions. A wave propagation simulator based on a 3D ray-tracing algorithm [9, 61] has been used for this purpose.

5.4.4 Space Focusing Technique

The first focusing technique used in this study in order to maximize the field intensity at the target point will be referred to as space focusing. In a typical scenario the target is located inside a building in an apartment complex, shown in Figure 5.29, surrounded by a set of sensors located randomly around the building. The proposed space focusing method works similar to standard arrays. However each sensor has a scanning array capable of focusing its beam into desired direction for the purpose of final focusing at the target location. On the other hand each sensor (transmitter at this moment) points its signal to few preferred direction which are found from forward scattering solution for the same scenario. The phases and amplitudes of the signals for transmission in desired directions are also determined from the solution of forward scattering problem.

5.4.5 Time Focusing Method

The space focusing algorithm helps to balance phase and transmission direction from transmitters such that all arrive at the target constructively. However the uniqueness of the solution for inverse problems is not guaranteed. A simple case for explaining the lack of uniqueness is when backscattering of transmitted signal from an adjacent object to the detector is much stronger than actual backscattering from target. Therefore additional mechanism is required to filter the actual backscattering of the real target from false alarms because of the early and late responses of other objects in the search area.

The advantage of ray-tracing algorithm used for solving forward scattering problem is determining delay profile as well as amplitude, phase and directions of paths at once. The last three sets of information were used for space focusing and now delay profile is used to perform time focusing. There are different ways which time focusing can be done. For the simplicity of detection system proposed in this paper, time focusing here is done by simultaneous transmitting from all transceivers and receiving at a time window around the mean value of all of the paths' delay. The width of time window is chosen proportional to standard deviation of the delay values, not less than 10 nsec to relax time gating procedure in practical applications.

5.4.6 Simulation Results

For scenario shown in Figure 5.29, 80 sensors are placed around the target building at 2 m above the ground, operating at 2.3 GHz. The forward problem has been solved for two different target position, in the 4^{th} floor in B_1 and 5^{th} floor in B_2. The results are used for optimum transmission from sensors. Figures 5.30 and 5.31 show angle of arrival for the rays arrived to the target positions. Then in order to filter spatially focused power at the target positions form undesired spikes at other positions, time focusing is done as described in section 5.4.5.

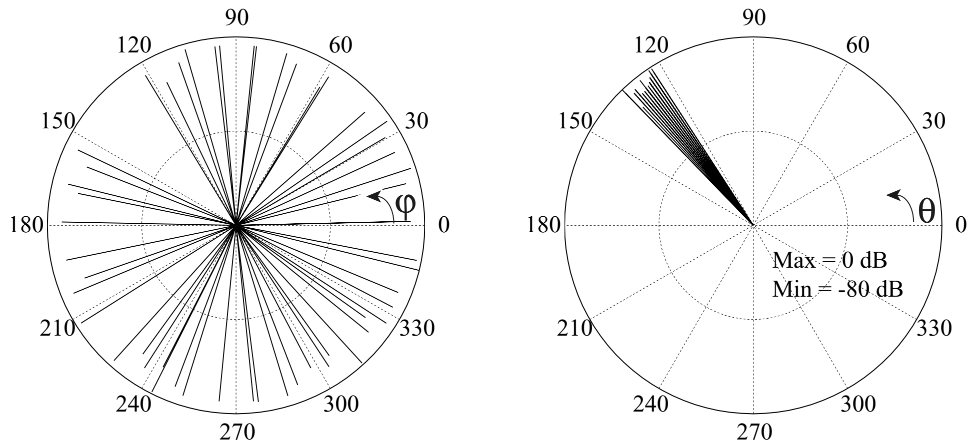

Figure 5.30: Angle of arrival for the target at the 4^{th} floor in B_1.

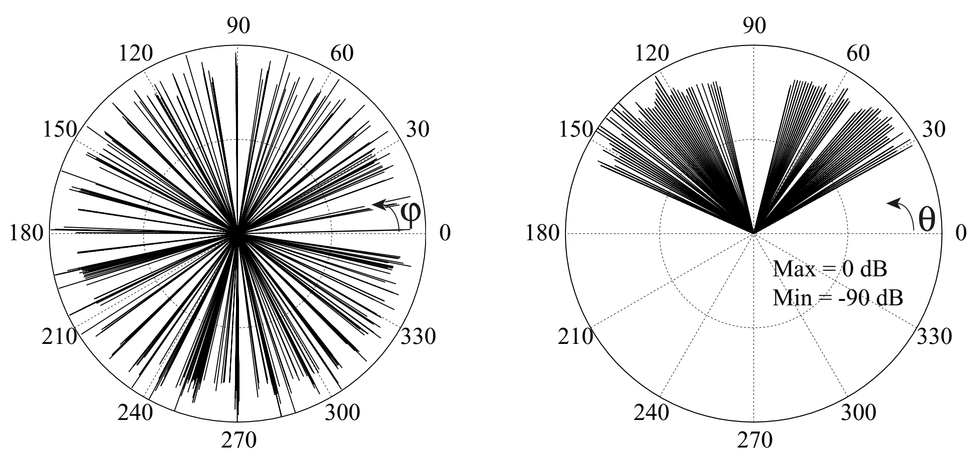

Figure 5.31: Angle of arrival for the target at the 5^{th} floor in B_2.

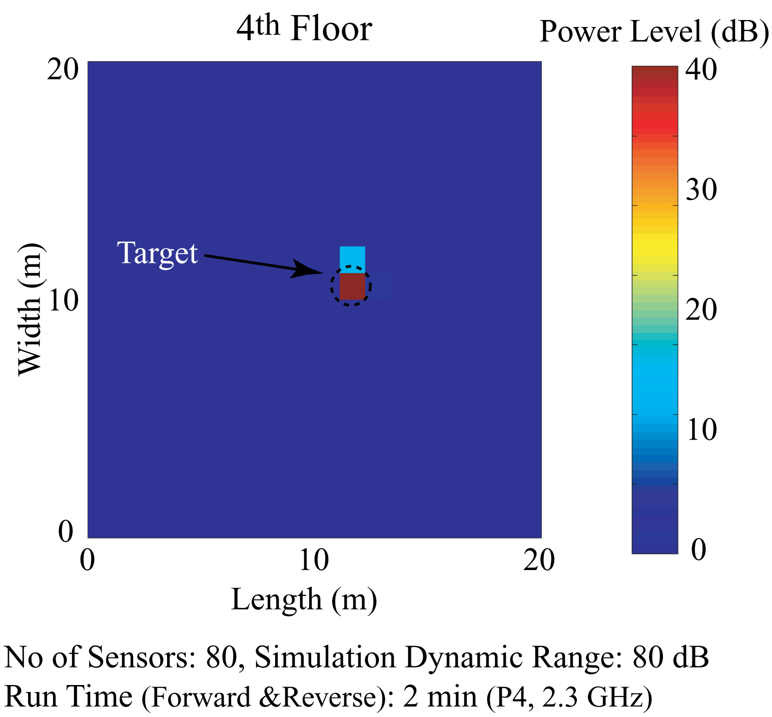

Figure 5.32: Field map at the 4^{th} floor in B_1.

Field map at 4^{th} floor in B_1 and 5^{th} floor in B_2, are shown in Figures 5 and 6 respectively. The hot (red) spot locates target's position, as it is shown focused field at desired position is at least 25 dB above field level at entire area at 4^{th} floor and 20 dB at 5^{th} floor. The reduction in focus for 5^{th} floor is because of higher signal attenuation and lower number of propagation paths. It is shown in Figures 5.34 and 5.35 that filed focusing at the target position has a narrow band behavior and rapidly reduces by changing the frequency (Δf = frequency difference between forward and reverse simulation). Also as Figure 5.36 shows reducing the number sensors weakens signal strength at the target position as expected.

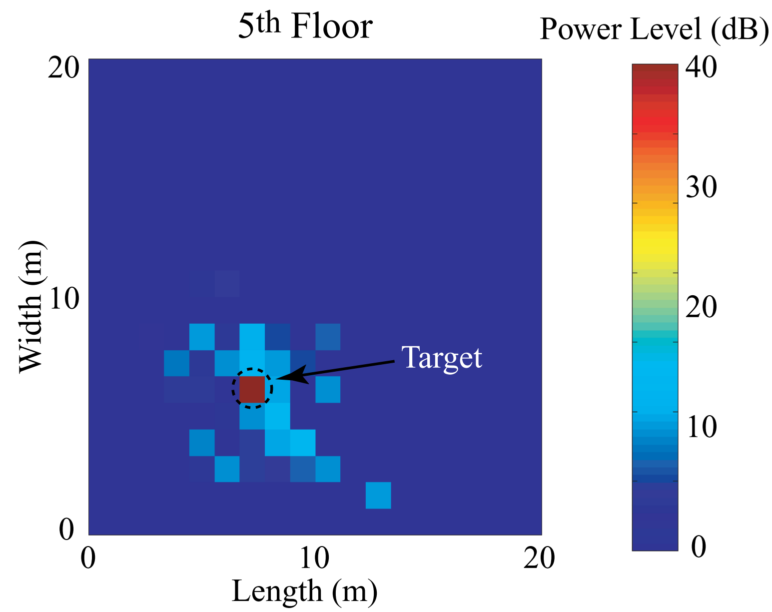

No of Sensors: 80, Simulation Dynamic Range: 90 dB
Run Time (Forward & Reverse): 11 min (P4, 2.3 GHz)

Figure 5.33: Field map at the 5^{th} floor in B_2.

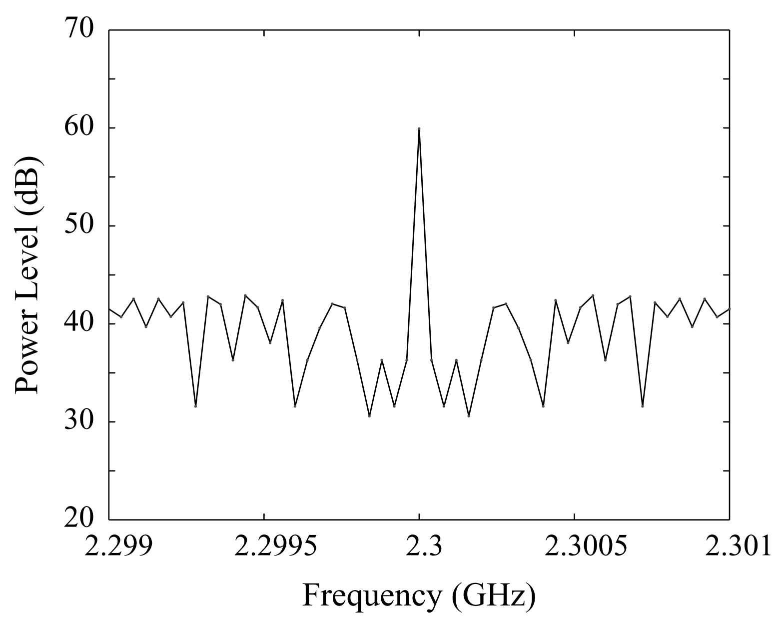

Figure 5.34: Frequency response of focused power at target.

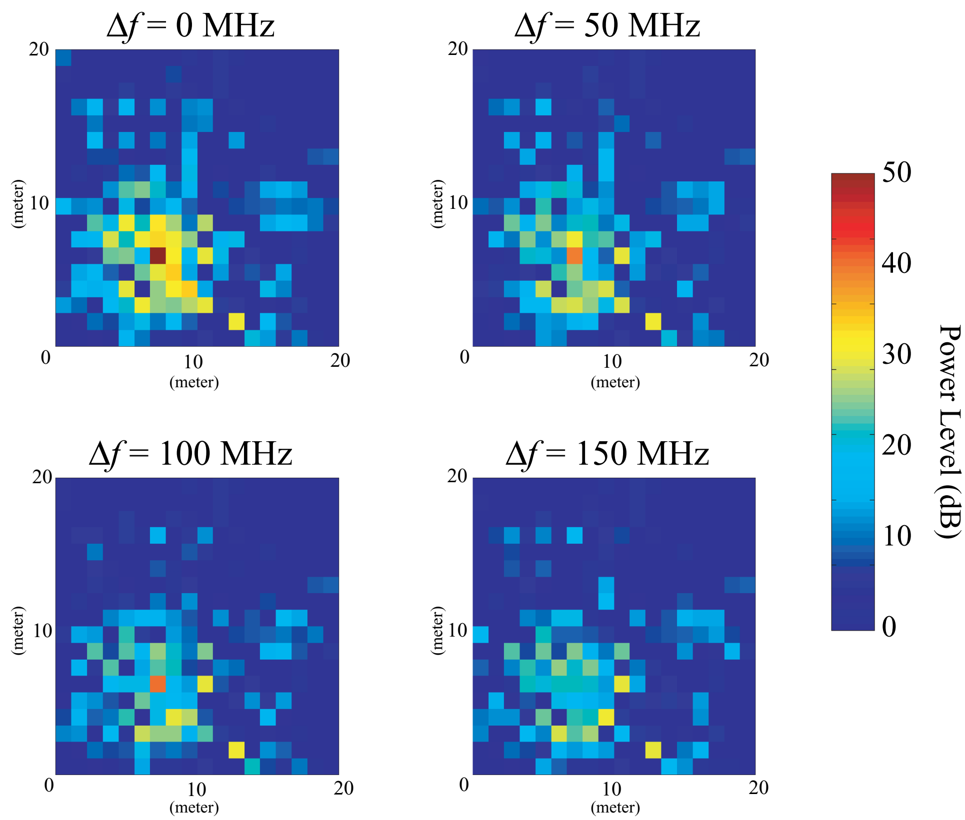

Figure 5.35: Reduction in focused power due to frequency shift.

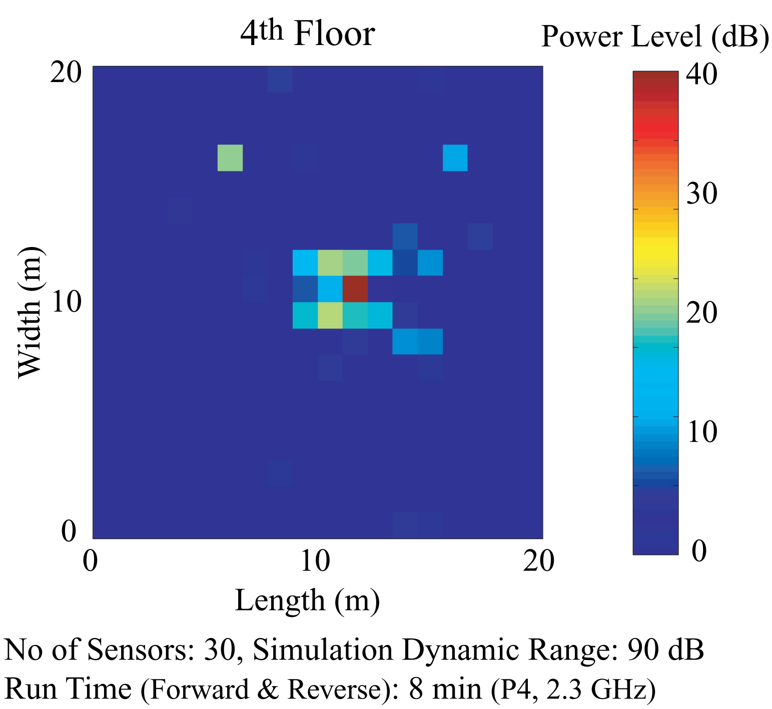

Figure 5.36: Focused power is reduced by decreasing number of sensors.

CHAPTER 6

Propagation Measurements and Model Validation

In this chapter, using the SPMS, different channel parameters for a few scenarios are measured and compared with predicted values, generated by the 3D physics-based channel simulator described in the previous chapter. Different urban scenarios are setup with the reconfigurable scaled building blocks and their relative locations are determined before field measurements. We start with simple scenarios composed of few building blocks and increase the environment complexity as the previous cases are examined and verified.

The first step is system calibration in the absence of any building or scatterers. This setup is necessary for examining the purity of system impulse response as well as establishing calibration factor for determination of pathloss. The XY-table, its support structure and other objects in the lab that are in close proximity of the probes can create significant multi-path. Although the effect of their multi-path can be gated out using the time domain capability of the VNA, they can potentially reduce the system dynamic range by raising the noise floor in the time domain. MM-wave absorber are used to cover the XY-table support structure as well as blocking the passage of rays outside the region of interest. These absorber also help to suppress the unwanted incoming signals from outside of the desired propagation environment.

For calibration the ground is also covered with absorbers to minimize the ground reflection. Figure 6.1 shows the time domain response of the system transfer function in

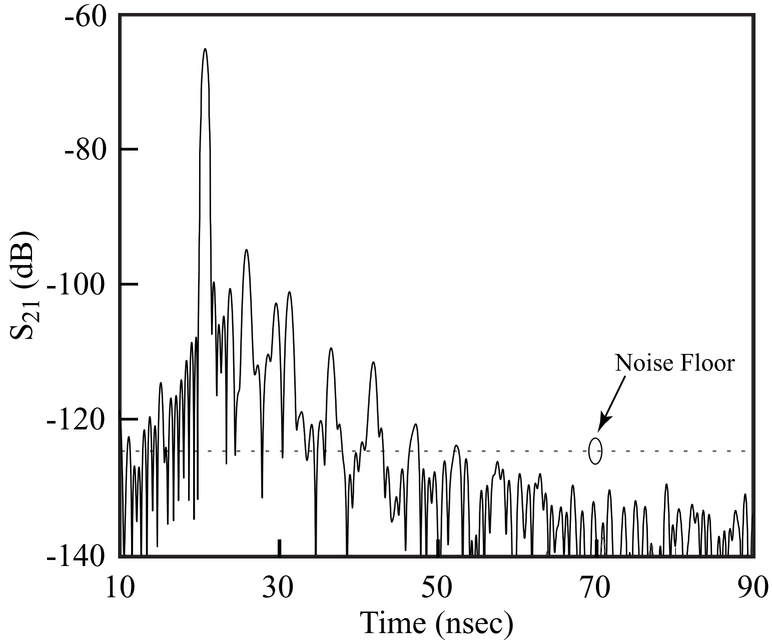

Figure 6.1: Time domain response of the SPMS for a through case in the absence of scatterers.

the absence of scatterers. This measurement is used to calibrate the frequency response. The first peak is correspond to direct propagation path between the transmitter and receiver probe and the smaller peaks as explained in chapter 4 are the artifacts of multi-path mainly caused by mismatches in receiver probe.

Representing the calibration signal in the absence of scatterers in the frequency domain by E_c^f, it can be shown that:

$$E_c(f,R_c) = T(f)\frac{e^{\frac{-j2\pi f R_c}{c}}}{R_c} \tag{6.1}$$

where R_c is the distance between the transmitter and receiver probes during the calibration and $T(f)$ is the composite transfer function of network analyzer, cables, amplifiers, and the probes. In the actual measurements the frequency response of channel can be written as:

$$T_c(f) = \frac{E_r(f,R)}{T(f)} \tag{6.2}$$

where $E_r(f,R)$ is the received signal.

6.1 Channel Measurement

The first example of urban scenario we consider is a simple scenario composed of two buildings as shown in Figure 6.2. A solid block, building *A*, and the second object, building *B*, is a two story hollow building with wall thickness of 1cm (0.4in). Building dimensions and their relative positions are give in Figure 6.2. The RF frequency range is set at 90.6-92.1 GHz and receiver is moved along a straight path shown in Figure 6.2 in steps of 2mm. The transmitter and receiver heights are set at 11cm and 12cm respectively.

Figure 6.3 shows the measured frequency response of the received signal at the start, middle and end points along the receiver path, shown in Figure 6.2. The measured and simulated pathloss are compared at $f_{RF} = 91.8GHz$ and shown in Figure 6.4. The simulation are carried out at higher resolution of 1mm. Figure 6.4 shows very good agreement between simulation and measurement results for major part of the path. There are a number of factors responsible for observed discrepancies between measurement and simulation. This include lack of accurate knowledge of the dielectric constant and conductivity of ground, reflections from absorbers which are isolating the measurement scene from the surrounding area, etc. It should also be noted that as distance between adjacent sample points is larger than half wavelength fast fading behavior of the pathloss is not properly demonstrated in the measured results.

A more complex scenario is shown in Figure 6.5. The wall thickness for all buildings is 1cm for this scenario. Transmitter and receiver heights are similar to those of the previous example. Figure 6.6 shows the measured frequency response of the receive signal for the start, middle and end points along the receiver path, shown in Figure 6.5. In Figure 6.7 the measured and simulated pathloss are again compared for $f_{RF} = 92.1GHz$. Except for points around $d = 6-7cm$ a good agreement between the simulation and measurements is seen.

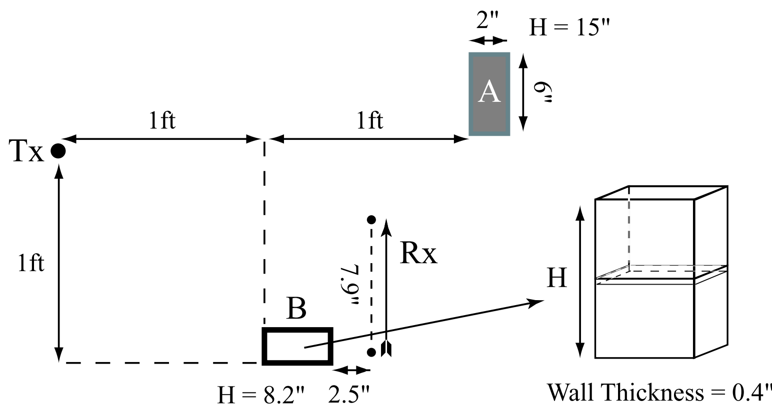

Figure 6.2: Top view of a simplified scenario considered for measurement.

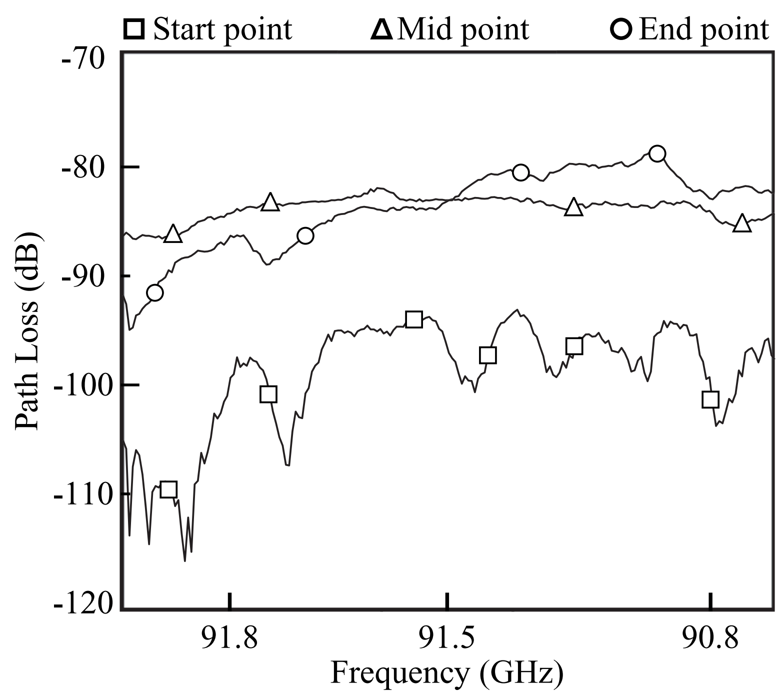

Figure 6.3: Measured frequency response for different points on the receiver path shown in Figure 6.2.

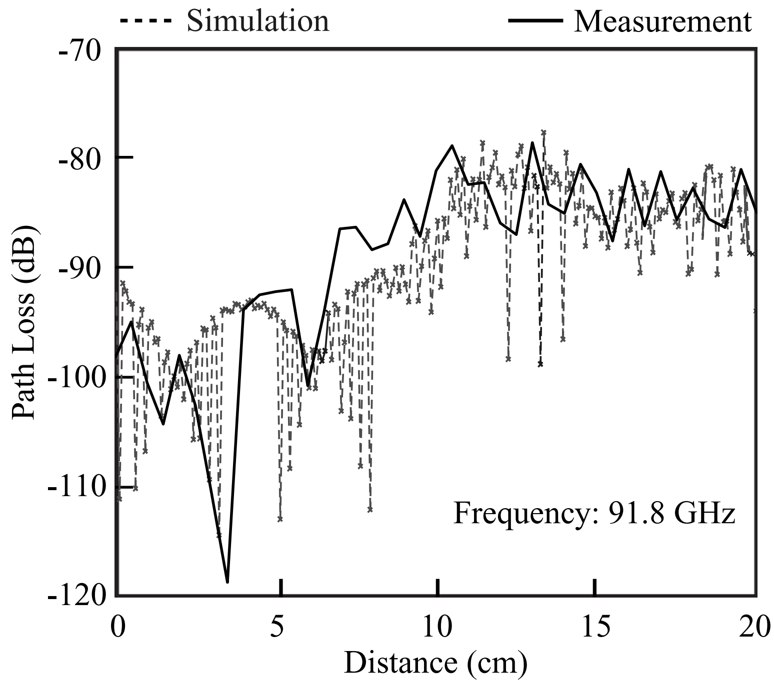

Figure 6.4: Measured and simulated pathloss for receiver path shown in Figure 6.2.

Possible explanation for the difference in levels in the $d = 6 - 7cm$ range between the simulated and measured results is that the sampling distance is grater than a half wavelength, which could result in missing null and peak points.

Another scenario is shown in Figure 6.8, which includes seven two story building blocks with different heights. The measured pathloss at different frequencies, for the receiver path in Figure 6.8, are shown in Figure 6.9. The measured and simulated pathloss for $f_{RF} = 91.8GHz$ are compared in Figure 6.10. Again a reasonable agreement between measured and simulated results can be seen.

The last scenario considered in this section is shown in Figure 6.11 which includes seven two stories building blocks with different heights. Measured and simulated pathloss for $f_{RF} = 91.8GHz$ are compared in Figure 6.12. As it can be seen the average difference between measured and simulated results is only 5dB over major part of the path. In order to evaluate the SPMS stability, the last measurement for scenario shown in Figure 6.11 was repeated and comparison between two measurement is shown in Figure 6.13. As it can be

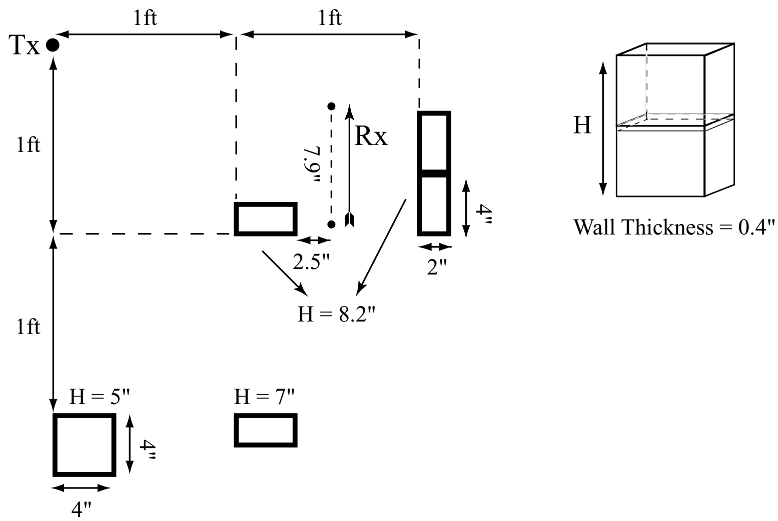

Figure 6.5: Top view of a scenario with five two stories building.

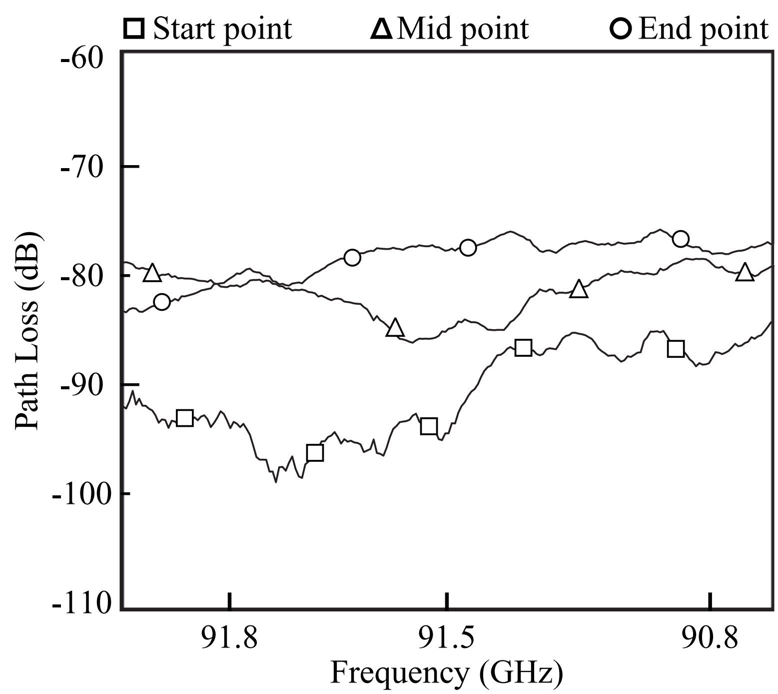

Figure 6.6: Measured frequency response for different points on the receiver path shown in Figure 6.5.

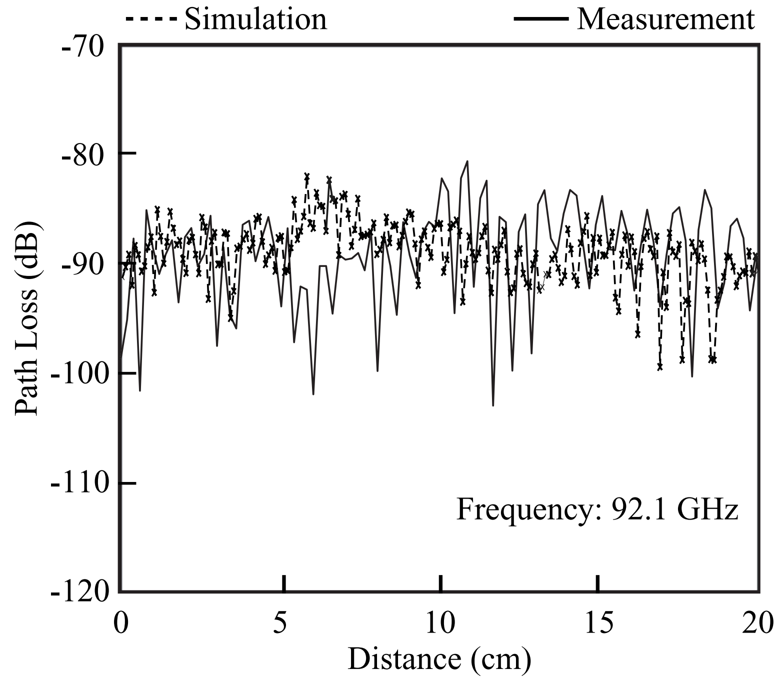

Figure 6.7: Measured and simulated pathloss for receiver path shown in Figure 6.5.

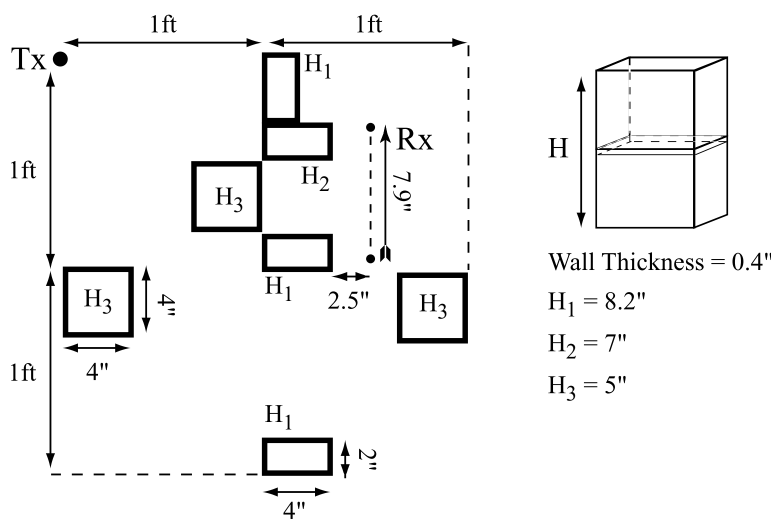

Figure 6.8: Top view of a scenario with seven two stories building.

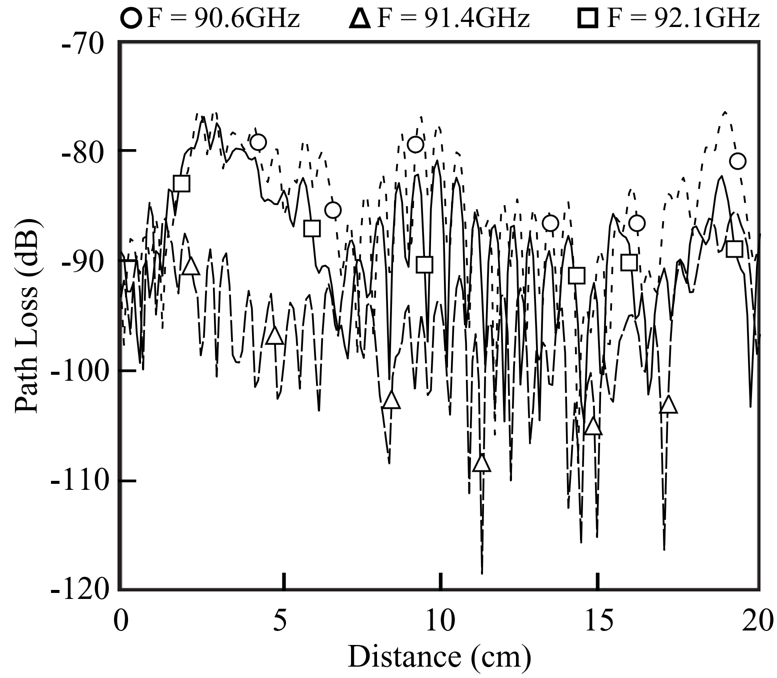

Figure 6.9: Measured pathloss at different frequencies for receiver path shown in Figure 6.8.

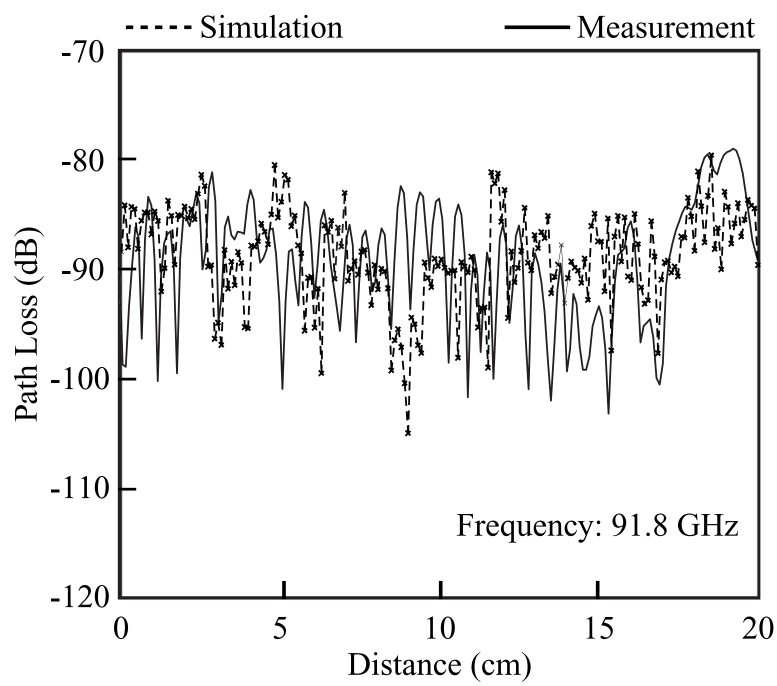

Figure 6.10: Measured and simulated pathloss for receiver path shown in Figure 6.8.

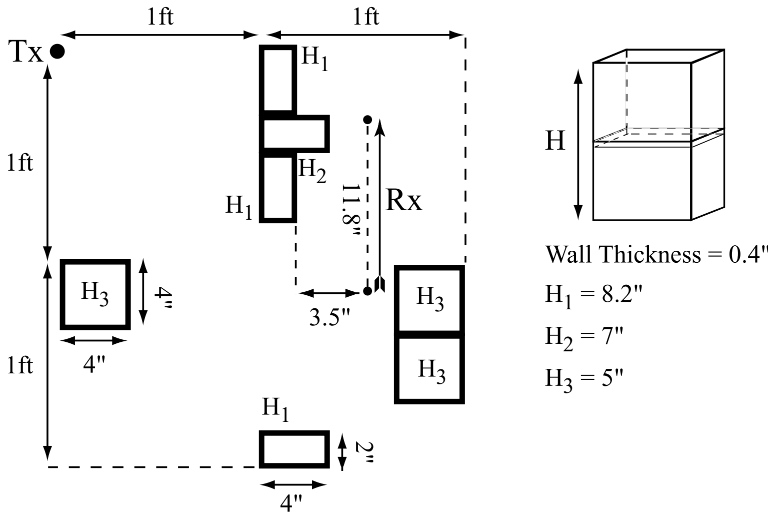

Figure 6.11: Top view of a scenario with seven two stories building.

seen the results are very similar for most of the path and major differences are related to the depth of captured fading which is very sensitive to the position.

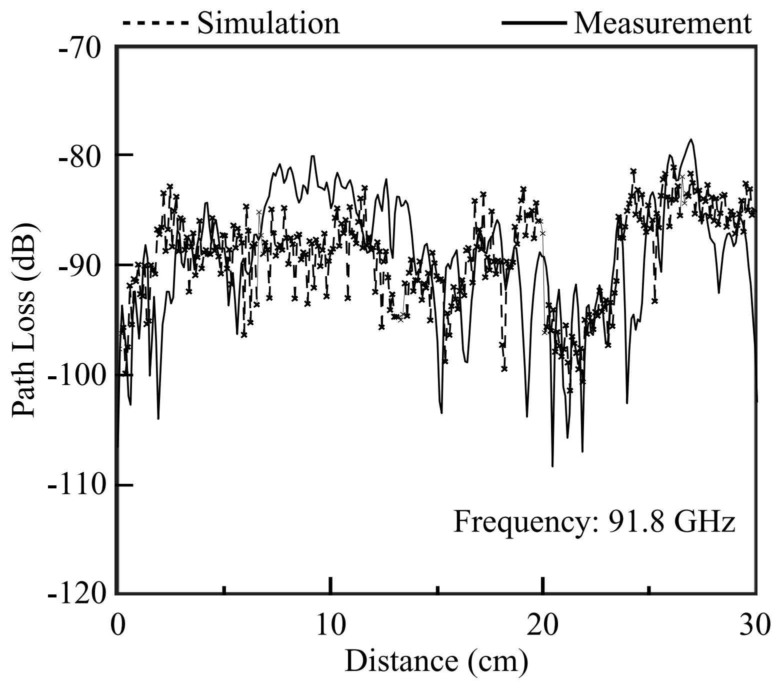

Figure 6.12: Measured and simulated pathloss for receiver path shown in Figure 6.11.

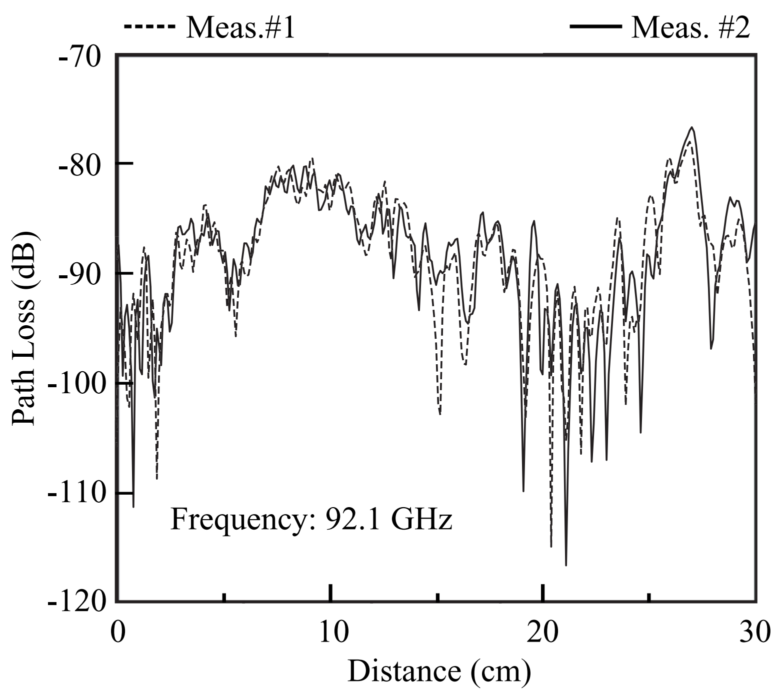

Figure 6.13: Two independent pathloss measurement for scenario shown in Figure 6.11 shows the SPMS stability.

CHAPTER 7

Conclusions, Applications and Future Work

7.1 Conclusions

A millimeter-wave scaled propagation measurement system (SPMS) as an alternate approach to the time consuming and expensive outdoor measurements was designed, fabricated and tested. Confining the desired range of frequency to systems operating at UHF to L-Band (0.5-2 GHz), dimensions of scatterers and terrain features in the scaled propagation channel are reduced by a factor of 50-200 for the proposed SPMS that operates at around 100 GHz. This reduction brings the size of building from few meters to few centimeters so a scaled model of city block can easily fit in a laboratory, and measurements can be done quickly, accurately, and cost effectively. This system allows accurate measurement of well defined channels under a controlled laboratory environment.

The system includes an x-y-z probe positioner, scaled model of a city block, miniaturized W-band transmitter and receiver probes, and a vector network analyzer. As the operating frequency of the network analyzer (L-band) is different from the required SPMS frequency (W-band), an up- and down-converter was designed and fabricated as part of the transmitter and receiver probes respectively.

The network analyzer in the SPMS was used for signal processing and data acquisition. Therefore the setup was configured to characterize the propagation channel in a manner similar to the standard S_{21} measurement. The network analyzer allows for coherent and broadband path loss measurement with a wide dynamic range. It was shown that with this system a signal as low as -125dBm, and a maximum pathloss of 100dB (dynamic range $\cong 65dB$) can be measured accurately. Also the time domain features of the network analyzer allow for measuring the power delay profile which makes the SPMS unique in channel modelling. Delay profile resolution of 0.5ns corresponding to 2GHz system bandwidth were measured at W-band.

The design, fabrication, and performance of individual circuit elements of SPMS were demonstrated in chapter 2. Construction of scaled buildings and different techniques used for characterization of building's material were described in chapter 3. XY table, which is an automatic positioner for receiver probe with the required accuracy and its specifications were also explained in chapter 3. The system calibration and overall system specifications were presented in chapter 4. Chapter 5 explained a physics based site specific channel model using 3D ray-tracing with few examples for indoor, outdoor and suburban areas. Also in this chapter the application of 3D ray-tracer simulator for a novel through wall imaging method based on space-time focusing technique were demonstrated. Chapter 6 presented few sample measurements of path-loss, coverage and power delay profile (PDP) using SPMS, and result was also verified by comparison between theory and measurement. Good agreement between simulation and measurements indicated the high accuracy of both the measurement system and the ray-tracing simulation model.

7.2 Applications and Future Work

The proposed system offers unique capabilities, including polarimetric and coherent path loss measurements, over a large dynamic range, accurate determination of fast and slow fading statistics, and characterization of the channel time delay profile. This research can be continued and applied for many applications, including: 1) Verifying the accuracy of existing wave propagation channel simulators, developing scattering models and macro-models for different types of buildings and complex objects and use them for physics-based wave propagation simulators, 2) Data collection for wireless communication using extensive inexpensive measurement for different scenarios, 3) Improving SPMS performance by reducing its operating frequency to lower W-band (70 GHz) where a variety of active devices such as LNAs and power amplifiers with output power in range of watts instead of mwatts are available, increasing bandwidth for higher range resolution, and multi-stage up- and down-conversion for reducing spurious, 4) Extending the physics based site specific channel model and its application such as scattering from more complex objects and through wall imaging, which its result will be used in the development of novel radar-based detection algorithms.

APPENDICES

Appendix A

Coherent approach for calculating reflectivity from multi-layer dielectric slabs

Coherent reflectivity $\Gamma_c(\theta_1)$ from interface of dielectric slab and air shown in Figure A.1 is defined as:

$$\Gamma_c(\theta_1) = |R_e(\theta_1)|^2 \tag{A.1}$$

where $R_e(\theta_1)$ is effective field reflection coefficient at the boundary 1. In coherent approach $R_e(\theta_1)$ accounts for the both amplitude and phase of the reflections in the media. In Figure A.1 if layer 3 extend from $\zeta = d$ to $\zeta = \infty$, the input impedance of the media looking from media one is obtained by

$$Z_{in} = Z_2 \left[\frac{1 + R_2 e^{-j2\gamma_2' d}}{1 - R_2 e^{-j2\gamma_2' d}} \right] \tag{A.2}$$

where

$$R_2 = (-1)^n \left(\frac{Z_3 - Z_2}{Z_3 + Z_2} \right); n = \begin{cases} 0 & for\ h\ polarization \\ 1 & for\ v\ polarization \end{cases} \tag{A.3}$$

$$\gamma_2' = \gamma_2 \sec\theta_2 \tag{A.4}$$

$$\gamma_2 = \frac{2\pi}{\lambda_0} \sqrt{\varepsilon_2} \tag{A.5}$$

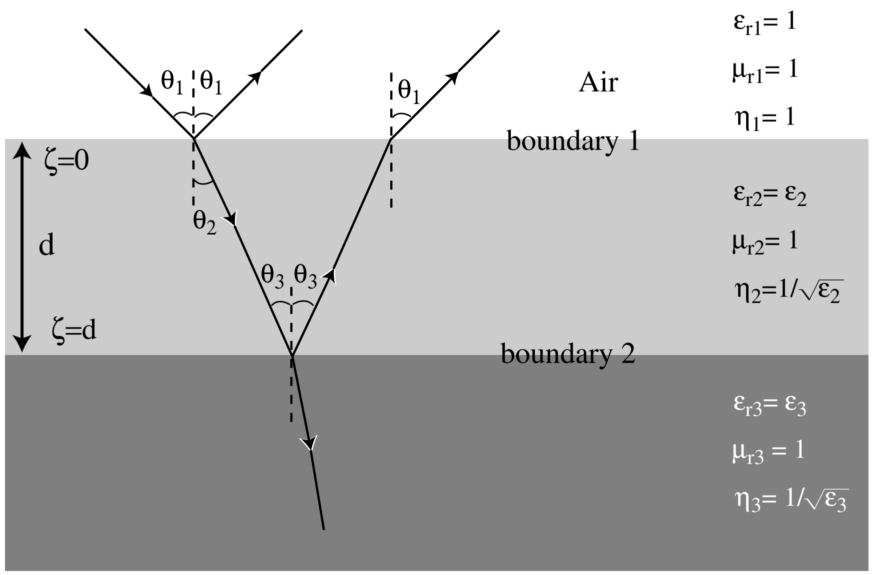

Figure A.1: Multi-layer dielectric slab.

Here R_2 is the reflection coefficient for a wave in medium 2 incident upon boundary2;, Z_1,Z_2, and Z_3 are defined by (A.6); and λ_0 is the free space wavelength.

$$Z_i = \begin{cases} \eta_i \sec\theta_i & for\ h\ polarization \\ \eta_i \cos\theta_i & for\ v\ polarization \end{cases} \tag{A.6}$$

For a lossy medium, ε_2 is complex, therefore γ_2 is complex:

$$j\gamma_2 = j\beta_2 + \alpha_2 \tag{A.7}$$

where

$$\alpha_2 = \frac{2\pi}{\lambda_0}\left|\mathrm{Im}\left(\sqrt{\varepsilon_2}\right|\right) \tag{A.8}$$

$$\beta_2 = \frac{2\pi}{\lambda_0}\mathrm{Re}\left(\sqrt{\varepsilon_2}\right) \tag{A.9}$$

Equation (A.2) can be rewritten as:

$$Z_{in} = Z_2\left[\frac{1 + R_2/L_2 e^{-j2\beta_2' d}}{1 - R_2/L_2 e^{-j2\beta_2' d}}\right] \tag{A.10}$$

where $\beta_2' = \beta_2 \sec\theta_2$ and $L_2 = e^{2\alpha_2 d \sec\theta_2}$. To calculate Z_{in}, we need the angles θ_2 and θ_3 which can be found by applying Snell's law:

$$\sin\theta_3 = \sqrt{\frac{\varepsilon_2}{\varepsilon_3}} \sin\theta_2 \tag{A.11}$$

$$\sin\theta_2 = \sqrt{\frac{1}{\varepsilon_2}} \sin\theta_1 \tag{A.12}$$

For low loss media such that $\varepsilon_2''/\varepsilon_2' \ll 1$ and $\varepsilon_3''/\varepsilon_3' \ll 1$, the imaginary parts of ε_2 and ε_3 can be neglected in computation of θ_2 and θ_3. After computing Z_{in}, $R_e(\theta_1)$ is obtained from:

$$R_e(\theta_1) = (-1)^n \left(\frac{Z_{in} - Z_1}{Z_{in} + Z_1}\right); n = \begin{cases} 0 & for\ h\ polarization \\ 1 & for\ v\ polarization \end{cases} \tag{A.13}$$

Inserting (A.10) into (A.13) and simplifying leads to

$$R_e = \frac{R_1 + \frac{R_2}{L_2} e^{-j2\beta_2' d}}{1 + \frac{R_1 R_2 e^{-j2\beta_2' d}}{L_2}} \tag{A.14}$$

and the coherent reflectivity Γ_c is given by:

$$\Gamma_c(\theta_1) = \left(\frac{\Gamma_1 + \frac{\Gamma_2}{L_2^2} + \frac{2\sqrt{\Gamma_1\Gamma_2}}{L_2}\cos(2\beta_2' d + \phi_1 - \phi_2)}{1 + \frac{\Gamma_1\Gamma_2}{L_2^2} + \frac{2\sqrt{\Gamma_1\Gamma_2}}{L_2}\cos(2\beta_2' d - \phi_1 - \phi_2)}\right) \tag{A.15}$$

where $\Gamma_1 = |R_1|^2$, $\Gamma_2 = |R_2|^2$, and ϕ_1 and ϕ_2 are the phase of R_1 and R_2. For metal back dielectric slab $\varepsilon_3 = 0 - j\infty$ and $R_2 = -1$.

Appendix B

Characterization of semi-lumped CPW elements for mm-wave filter design

In this appendix two accurate models for interdigital capacitors and shunt inductive stubs in CPW structures are presented and validated over the entire W-band frequency range. Using these models, a novel bandpass filter and a miniaturized highpass filter are designed and fabricated. By inserting interdigital capacitors in bandpass filter resonators, an out of band transmission null is introduced which improves rejection level up to 17dB over standard designs of similar filters. A highpass filter is also designed, using semi-lumped element models in order to miniaturize the filter structure. It is shown that a 5^{th} order highpass filter can be built with a maximum dimension of less than $\lambda_g/3$. Great agreement between simulated and measured responses of these filters is demonstrated.

B.1 Introduction

Microwave filters have been studied extensively using both lumped and distributed elements. However the literature concerning planar mm-wave filters, especially at W-band frequencies, is scarce. There are few difficulties involved in filter design and fabrication at mm-wave frequencies and above. Most parasitic elements, usually can be ignored at lower frequencies. However, their effects become significant at mm-wave frequencies. The parasitic elements and their effects usually cannot be considered as design parameters. Hence they have to be accurately modelled and compensated for. To avoid dealing with the parasitic effects, use of structures with minimal parasitic features can be considered. CPW line discontinuities are well characterized at microwave frequencies [28–30] and have been studied to some extent at higher frequencies, up to 50 GHz [31–33]. However modelling and characterization of such discontinuities at W-band frequencies is rather limited. Calibration accuracy at W-band is one of the major difficulties in characterizing parasitic capacitances and inductances, which can be as small as a fraction of a fF and a pH, respectively. Another problem is that the dimensions of typical lumped elements become comparable with the wavelength and require more complicated models to achieve reasonable accuracy. This paper provides accurate models for semi-lumped elements, which facilitate a systematic approach for filter design at mm-waves. Furthermore using a parasitic component of the proposed model as a design parameter, an out-of-band transmission null in a BPF response is introduced.

In the next section an accurate model for series interdigital capacitors in CPW lines is introduced and validated over a wide range of physical dimensions. Then in section B.3 an existing model for shunt inductive stubs [42] is modified to be valid at W-band frequencies. In sections B.4 and B.5, design, fabrication and measurements of a novel bandpass filter and a miniaturized highpass filter are presented, which make use of the semi-lumped elements.

B.2 Interdigital Capacitors in CPW lines

Interdigital capacitors are used either far below their resonant frequencies [62–65] or as quarter wavelength series open stubs [29, 33] to ensure the accuracy of simple existing models (lumped capacitor and open stub respectively). For the quarter wavelength open

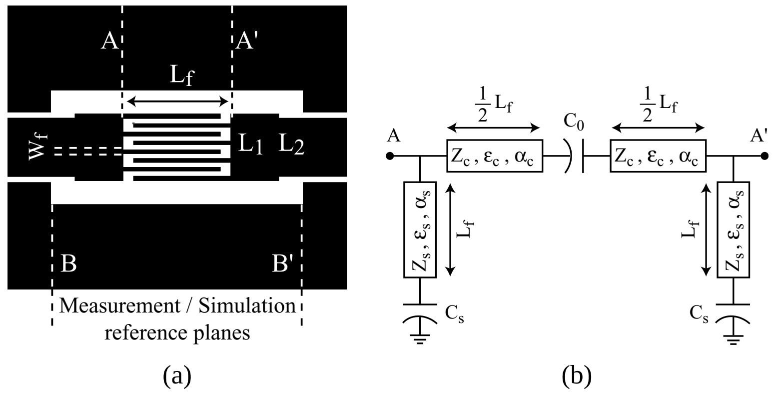

Figure B.1: Interdigital capacitor; (a) Layout, (b) Circuit model.

stub case, complicated models for capturing the behavior of parasitic elements have been considered, to increase the accuracy of the stub model [28, 66]. However, the large number of parameters introduced in these models limits their applicability. Despite the complexity, the accuracy of these models is still insufficient for applications in W-band frequencies.

Due to limitations in width of the center conductor of CPW lines (for preventing transversal mode radiation) and minimum achievable gap size (limited by the fabrication process), large capacitances can only be achieved by increasing capacitor finger length. Therefore, a complete model which can accurately represent interdigital capacitor behavior over a wide range of finger lengths, and with a minimum number of parameters, is needed to facilitate design procedure.

In this section a new physics based model is introduced and validated over the entire W-band frequency range for different capacitor finger length values. Figs. B.1(a) and B.1(b) show the layout and circuit model of the interdigital capacitor, respectively. In order to extract the capacitor model, the effect of extra lines between A and B as well as A' and B' are de-embedded. The discontinuity between lines L_1 and L_2 is negligible because the impedance change is only about 3%. For a fixed CPW line geometry, finger width (W_f), which is selected to be equal to gap width, determines the effective dielectric constants (ε_c, ε_s), the attenuation constants (α_c, α_s), and the characteristic impedances (Z_c, Z_s) of the series and shunt line segments of the circuit model. C_0 and C_s are functions of finger length

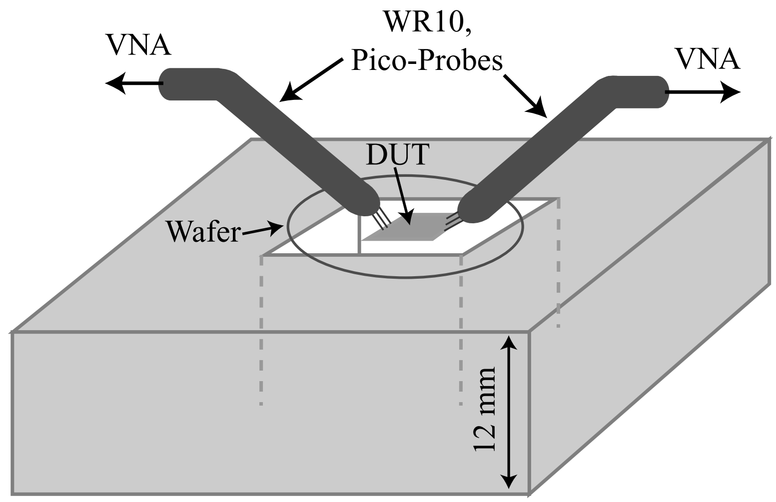

Figure B.2: Wafer holder with a cavity under DUT.

(L_f) only.

The dimensions of a typical CPW line and interdigital capacitor finger length and gap width are given in Table B.1. The capacitor shown in Figure B.1(a) has been fabricated with different lengths ranging from 100 to 400 μm on a 10 mil thick Quartz wafer. The S-parameter measurements for these capacitors in W-band (75-110 GHz) were realized using a probe station (for on wafer measurements), HP-8510C network analyzer, and HP-W85104A mm-wave test setup.

The probe station chuck, which holds the wafers, changes a CPW line to a conductor-backed CPW line, and thus, it affects the phase constant of the line [67] and the values of the parasitic elements. In order to eliminate these effects, a supporting structure with a cavity in the middle (shown in Figure B.2) is built and placed on top of the probe station's chuck. Method of Moment (MOM) and circuit simulations are performed using the Agilent Advanced Design System (ADS). For the dimensions given in Table B.1, the effective dielectric constants, the attenuation constants, and the characteristic impedances of the circuit model are extracted by comparing the measured and simulated S parameters (magnitude and phase) for 11 different cases (100 to 350 μm). These are provided in Table B.2. The values of C_0 and C_s are only dependent on normalized finger length ($l_f = L_f/L_{f0}$) and

Table B.1: CPW Line and Interdigital Capacitor Dimensions

W_{Line}	G_{Line}	W_{Finger}	G_{Finger}
$115\mu m$	$40\mu m$	$7.5\mu m$	$7.5\mu m$

Table B.2: Model Parameters for Interdigital Capacitor

$Z_c(\Omega)$	$Z_s(k\Omega)$	ε_c	ε_s	$\alpha_c(dB/cm)$	$\alpha_s(dB/cm)$
96	5.4	2.5	3.4	2.5	3.7

are given by:

$$C_0 = C_{00}(-0.12l_f^2 + 1.19l_f - 0.09) \tag{B.1}$$

$$C_s = C_{s0}(0.6 + 0.4l_f) \tag{B.2}$$

where $C_{00} = 15.9fF$ and $C_{s0} = 0.1fF$ are values of C_0 and C_s at $L_{f0} = 100\mu m$ respectively. The relation between the capacitance value and its physical length for short lengths is following a linear behavior, hence these equations are expected to be also valid for length values smaller than 100 μm. The maximum error is less than 4% over the mentioned range.

Figure B.3 compares the series capacitance (C_0) value, given by (B.1), with its measured value. As shown, for finger length values above $250\mu m$, capacitance does not increase linearly with finger length. To capture capacitance behavior for higher length values, a second order term is provided in (B.1). Figs. B.4, B.5 and B.6 compare the measured S-parameters (magnitude and phase) with the MOM and circuit model simulation results for three different capacitor finger length values of $100\mu m$, $250\mu m$ and $300\mu m$. The circuit model results show excellent agreement with the measurements in all situations. The circuit results show an even a better agreement with the measurement than the MOM result. The reason is that MOM simulations in ADS for CPW structures are based on magnetic current modelling and, thus, cannot handle metallic losses.

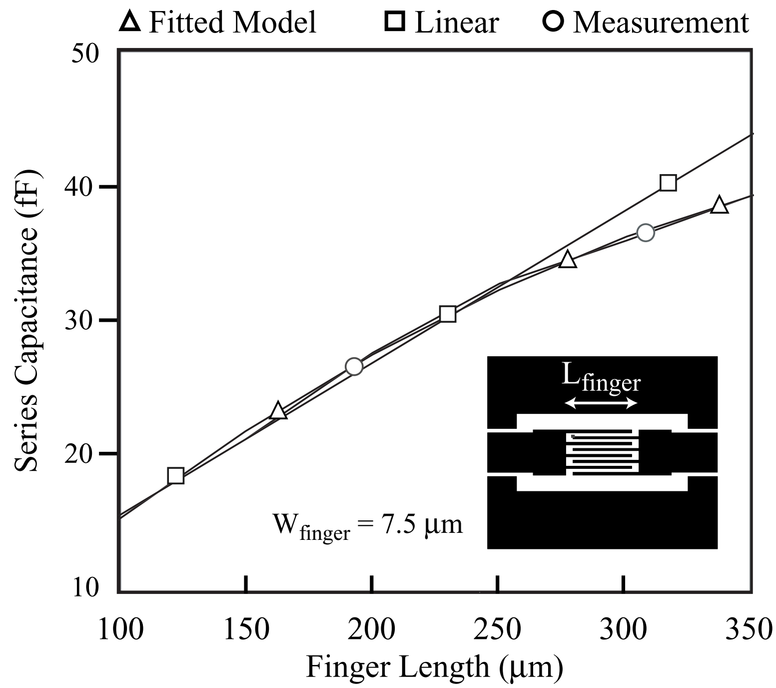

Figure B.3: Series capacitance of interdigital capacitors in CPW lines.

B.3 Shunt Inductors in CPW Lines

In this section short circuit stubs, shown in Figure B.7(a), which are often used as inverters in filter designs [42, 43], are characterized at W-band for different stub length and width values. As the accuracy of the closed form equation for inductance [42] is quite poor at W-band frequencies (errors often greater than 100%), inductance values have been extracted by comparison between simulation results for the circuit model shown in Figure B.7(b) and measured data for 20 different cases. The inductance values versus inductor lengths for two different inductor widths are shown in Figure B.8. As demonstrated, the inductance has a linear relation with the stub length within the selected range. This relationship can be described by:

$$L_{ind}(pH) = \begin{cases} L_{w1}(0.49l_1 + 0.5) & W_{ind} = 30\mu m \\ L_{w2}(1.76l_2 - 0.75) & W_{ind} = 25\mu m \end{cases} \tag{B.3}$$

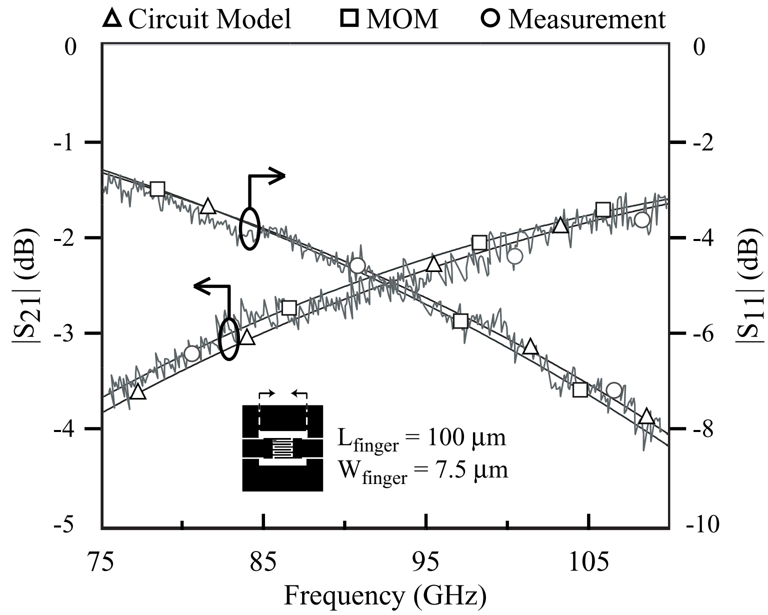

(a)

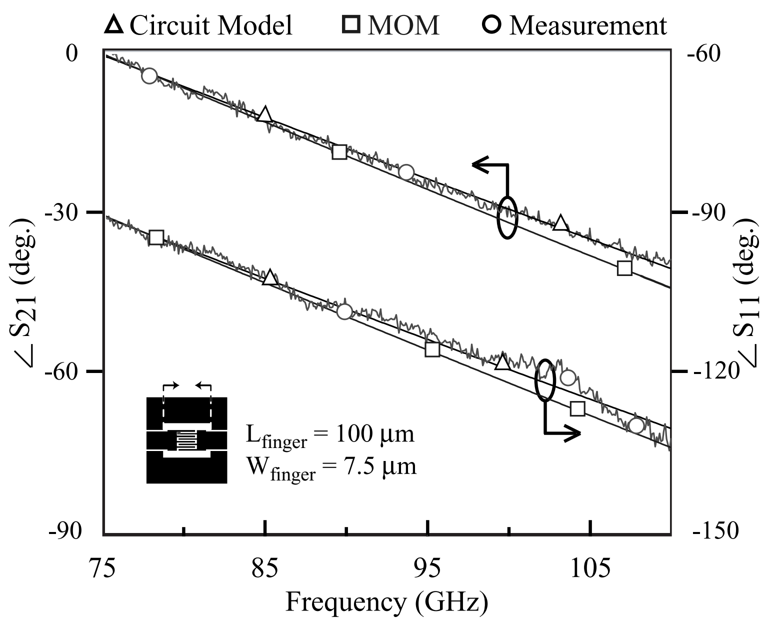

(b)

Figure B.4: Measured and simulated S-parameters of interdigital capacitor, $L_f = 100\mu m$; (a) Magnitude, (b) Phase.

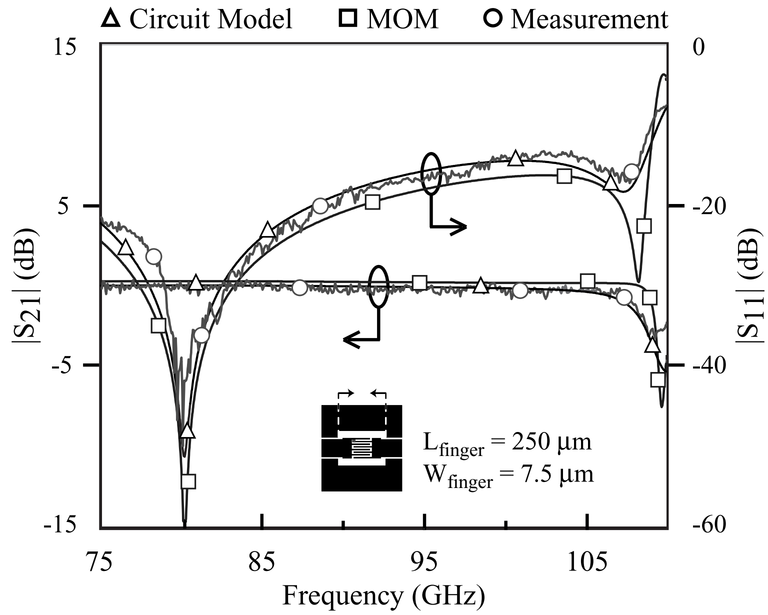

(a)

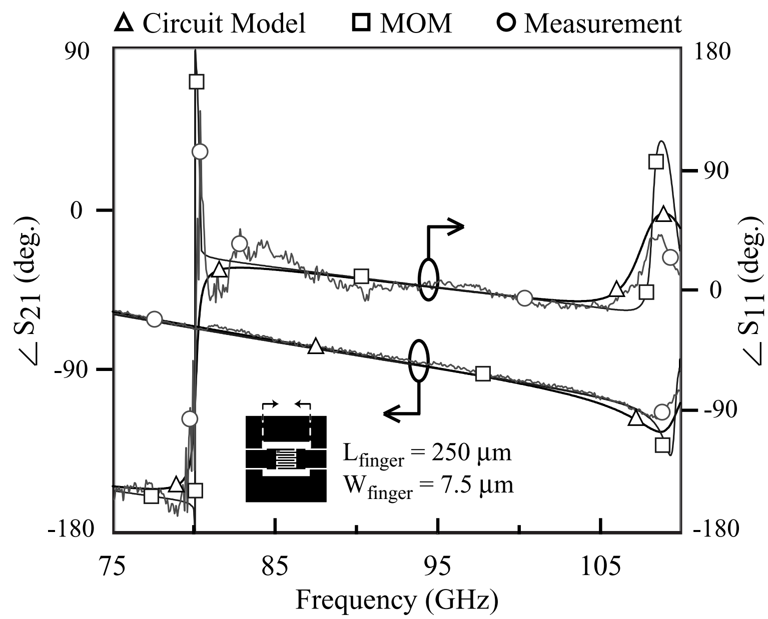

(b)

Figure B.5: Measured and simulated S-parameters of interdigital capacitor, $L_f = 250\mu m$; (a) Magnitude, (b) Phase.

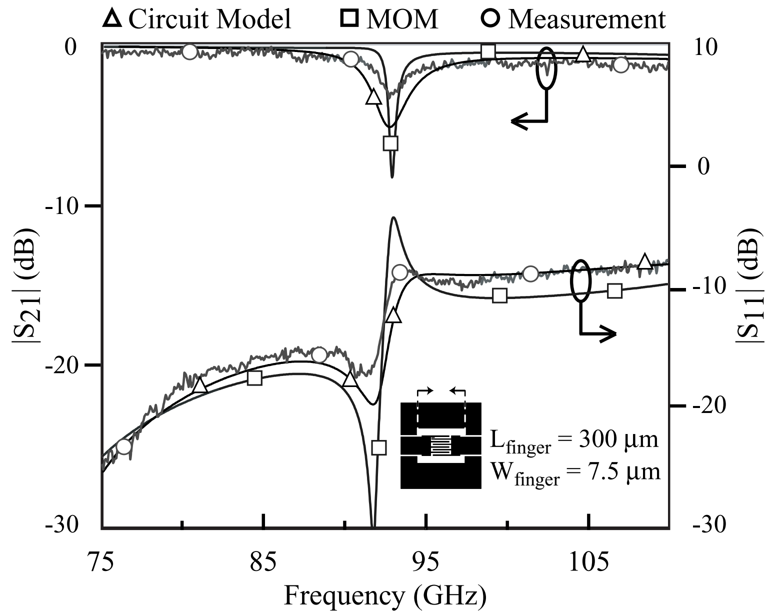

(a)

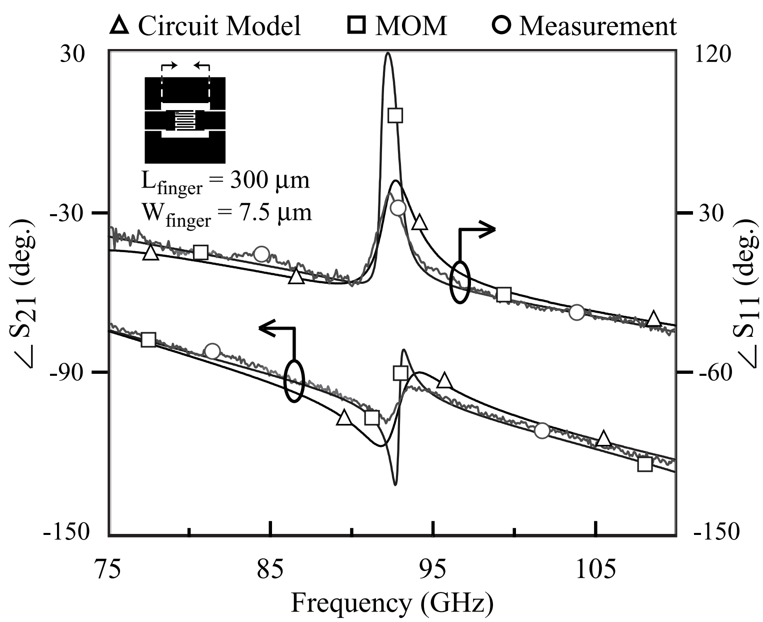

(b)

Figure B.6: Measured and simulated S-parameters of interdigital capacitor, $L_f = 300\mu m$; (a) Magnitude, (b) Phase.

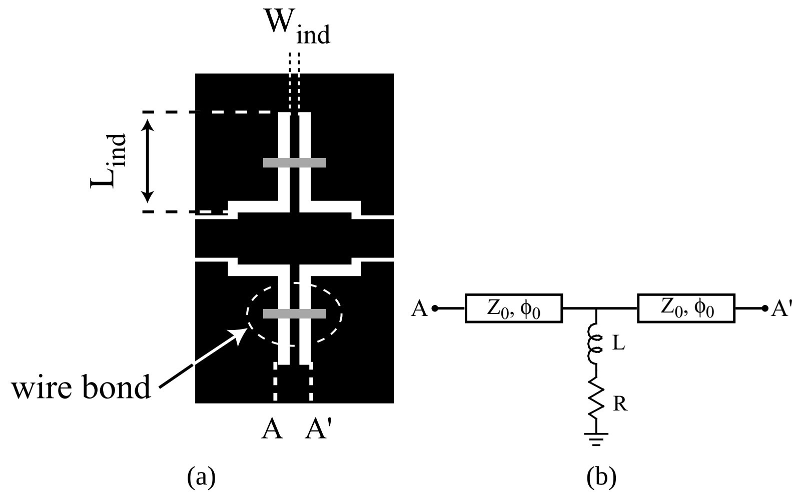

Figure B.7: Characterization of effective inductance and resistance for short stubs in CPW line; (a) Inductor layout, (b) Circuit model.

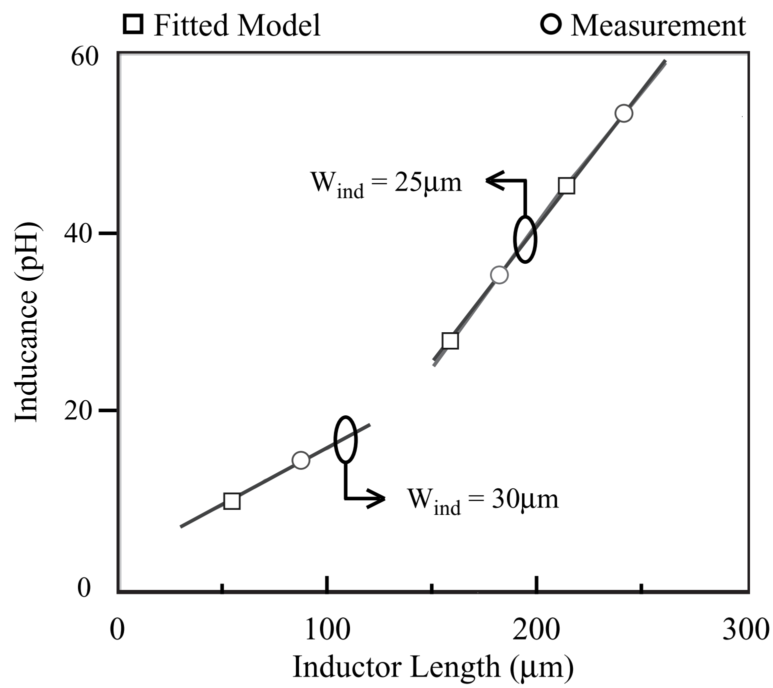

Figure B.8: Inductance of short circuit stubs in CPW lines.

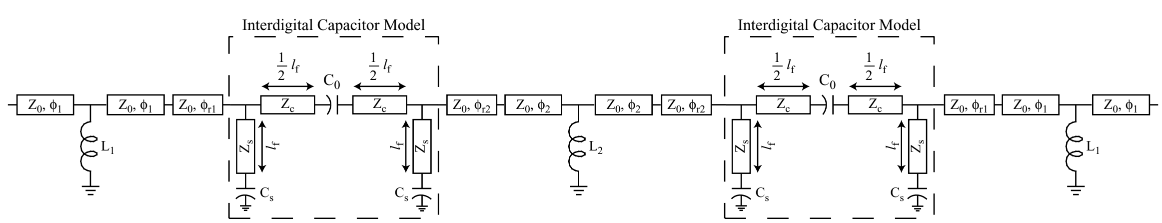

Figure B.9: New inductive coupled resonator bandpass filter circuit model.

where $L_{w1} = 7.7pH$ and $L_{w2} = 25.4pH$ are inductance values at $l_{10} = 30\mu m$ and $l_{20} = 150\mu m$ respectively, and $l_1 = L_{ind}/l_{10}$, $l_2 = L_{ind}/l_{20}$.

B.4 Bandpass Filter

In this section we demonstrate the usefulness of the accurate models of the semi-lumped elements introduced in the previous sections. A standard inductive coupled resonator bandpass filter [42], is modified by placing an interdigital capacitor in each resonators section, as shown in Figure B.9 and B.10. The equivalent shunt loaded stubs of the interdigital capacitors (Figure B.1(b)) provide a transmission null, and this is used to improve the out-of-band rejection response. The position of the null can be controlled simply by the length of the interdigital capacitor fingers. Figure B.11 compares simulation results for the new filter with a standard one. As shown, the 3dB bandwidth of the new filter is slightly (10%) less than the standard filter, while the rejection at a desired frequency can be improved by 20 dB. Due to minor radiation loss from the interdigital capacitors, the quality factor (Q) of the resonators is slightly decreased in comparison with their values for the standard resonators. Consequently, the measured results of this filter shows 0.5 dB more insertion loss. This filter was fabricated on a 10 mil thick Quartz wafer using standard lithography and wet etching on $3\mu m$ electroplated gold. Figure B.12 shows good agreement between the measured and simulated results of the circuit model. In Figure B.12 the nonphysical MOM response around 104 GHz occurs because of MOM simulator failure.

B.5 Miniaturized Highpass Filter

The main goal of modelling semi-lumped elements is to use them as lumped elements in filter design. Lumped element filters have very compact size which can be beneficial in many applications. Using a ladder network of three series capacitors and two shunt

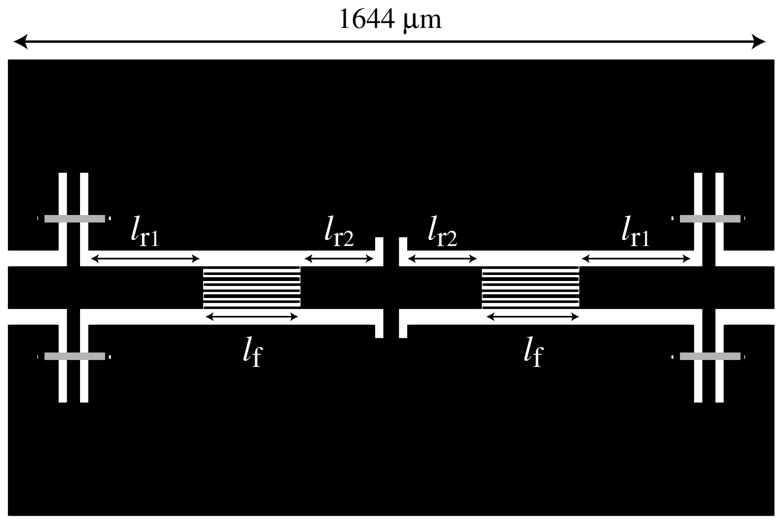

Figure B.10: New inductive coupled resonator bandpass filter layout.

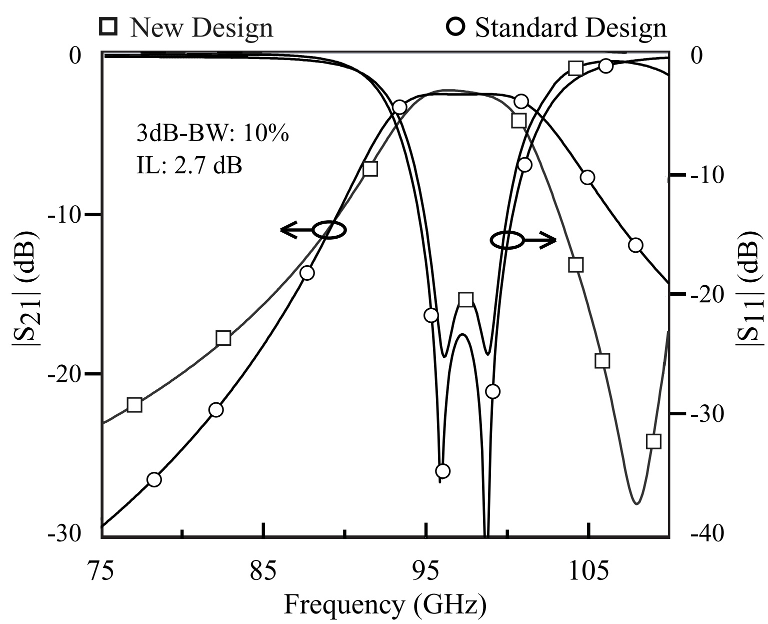

Figure B.11: Simulation results for the new inductive coupled resonator bandpass filter vs standard type of this filter.

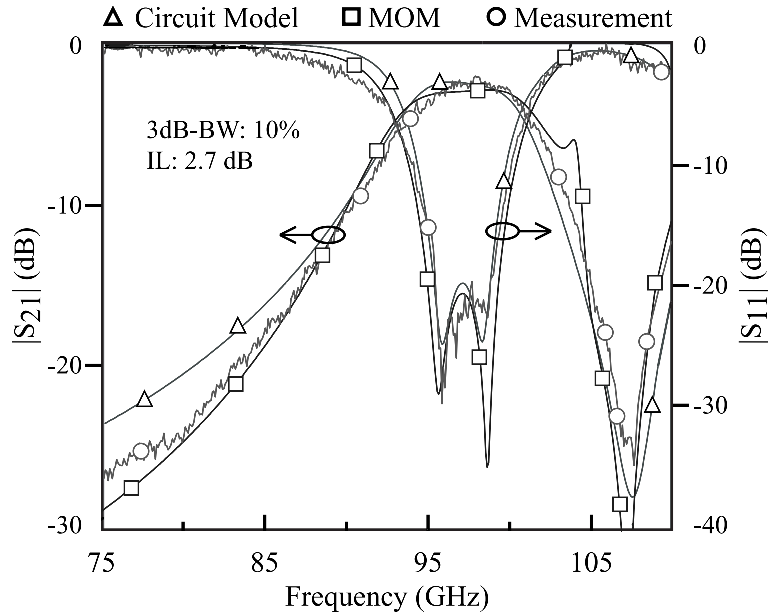

Figure B.12: Simulation and measurement results for the new inductive coupled resonator bandpass filter.

inductors, which were modelled and described in sections B.2 and B.3, a miniaturized highpass filter, shown in Figure B.13, is designed. As can be seen, the total length of the filter is only 750μm, which is less than $\lambda_g/3$ at the cutoff frequency of the filter. This filter was also fabricated on a Quartz wafer, and its measured and simulated results are compared in Figure B.14. It can be seen that the circuit model results have good agreement with both the MOM and measurement results. There are second order effects such as interactions between inductors and capacitors that cannot be estimated by the circuit model and these can be a source for degrading return loss. However it should be noted the circuit model is still working as good as MOM.

B.6 Conclusion

Simple and accurate models for two semi-lumped CPW elements were presented and validated at W-band frequencies for different dimensions. The simulation results of the extracted models show good agreement with the measured results. The models greatly

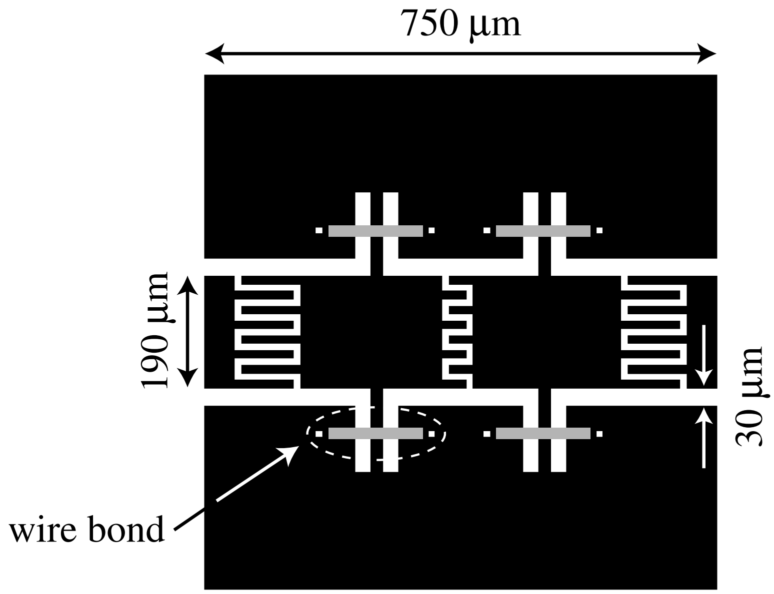

Figure B.13: Miniaturized highpass filter layout.

simplify the process of filter design at W-band and higher frequencies. The semi-lumped elements were used for designing two mm-wave filters, a bandpass and a highpass, and helped to improve filter response in the first case and miniaturization in the second case.

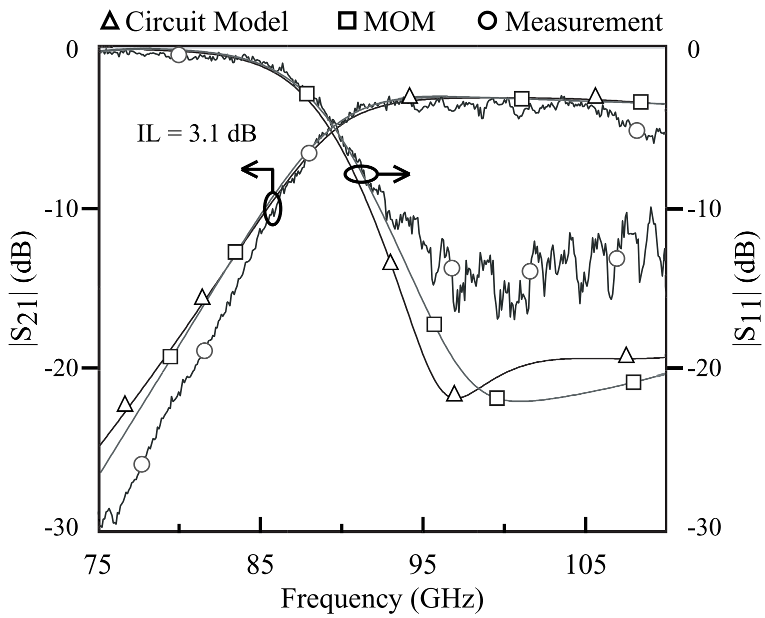

Figure B.14: Simulation and measurement results for the miniaturized highpass filter.

BIBLIOGRAPHY

BIBLIOGRAPHY

[1] D. Dinis and J. Fernandes, “Provision of sufficient transmission capacity for broadband mobile multimedia: A step toward 4G,” *IEEE Commun. Mag.*, vol. 39, pp. 46–54, August 2001.

[2] B. G. Evans and K. Baughan, “Visions of 4G,” *Electron. Commun. Eng. J.*, vol. 12, no. 6, pp. 293–330, December 2000.

[3] D. Parker, “Microwave industry outlook-deffense applications,” *IEEE Trans. Microwave Theory and Tech.*, vol. 50, no. 3, pp. 1039–1041, March 2002.

[4] Y. Okumara, E. Ohmori, T. Kawano, and K. Fukuda, “Field strenght variability in VHF and UHF land mobile service,” *Rev. Elect. Comm. Lab.*, vol. 16, no. 9-10, pp. 825–873, September-October 1968.

[5] M. Hata, “Emprical formula for propagation loss in land mobile radio services,” *IEEE Trans. on Vehicular Tech.*, vol. 29, pp. 317–325, August 1980.

[6] A. G. Longley and P. L. Rice, “Prediction of tropospheric radio transmission loss over irregular terrain-a computer method,” *Institute for Telecommun. Sci., Environmental Sci.*, vol. 16, no. 9-10, pp. Technical Report ERL 79–ITS 67, July 1968.

[7] S. Y. Seidel and T. S. Rappaport, “Site-specific propagation prediction for wireless in-building personal communication system design,” *IEEE Trans. on Vehicular Tech.*, vol. 43, pp. 879–891, November 1994.

[8] S. Chen and S. Jeng, “An SBR/image approach for radio wave propagation in indoor environments with metallic furniture,” *IEEE Trans. Antennas and Propag.*, vol. 45, pp. 98–106, January 1997.

[9] F. Aryanfar and S. Safavi-Naeini, “Electromagnetic modeling of radio wave propagation in micro- and pico-cellular environments,” *IEEE Conf. on Antennas and Propag. for Wireless Commun.*, vol. 43, pp. 25–28, November 1998.

[10] C. Yang, B. Wu, and C. Ko, “A ray-tracing method for modeling indoor wave propagation and penetration,” *IEEE Trans. Antennas and Propag.*, vol. 46, pp. 907–919, June 1998.

[11] G. E. Athanasiadou, A. R. Nix, and J. P. McGeehan, “A microcellular ray-tracing propagation model and evaluation of its narrow-band and wide-band predictions,” *IEEE Trans. Antennas and Propag.*, vol. 18, no. 3, pp. 322–335, March 2000.

[12] R. P. Rossi and Y. Gabillet, “A mixed ray launching/tracing method for full 3D UHF propagation modeling and comparison with wide-band measurements,” *IEEE Trans. Antennas and Propag.*, vol. 50, no. 4, pp. 517–523, April 2002.

[13] A. L. Martin and T. Vu-Dinh, “A statistical characterization of point-to-point microwave links using biased rayleigh distributions,” *IEEE Trans. Antennas and Propag.*, vol. 45, no. 5, pp. 806–821, May 1997.

[14] J. Kivinen, X. Zhao, and P. Vainikainen, “Empirical characterization of wideband indoor radio channel at 5.3 GHz,” *IEEE Trans. Antennas and Propag.*, vol. 49, no. 8, pp. 1192–1203, August 2001.

[15] R. A. J, N. Amitay, G. J. Owens, and R. R. Roman, “Radio propagation at microwave frequencies for line-of-sight microcellular mobile and personal communications,” *IEEE Trans. on Vehicular Tech.*, vol. 40, pp. 203–210, February 1991.

[16] W. Honcharenko, H. L. Bertoni, and J. L. Dialing, “Bilateral averaging over receiving and transmitting areas for accurate measurements of sector average signal strength inside buildings,” *IEEE Trans. Antennas and Propag.*, vol. 43, no. 5, pp. 508–512, May 1995.

[17] K. Kalliola, H. Laitinen, P. Vainikainen, M. Toeltsch, J. Laurila, and E. Bonek, “3-D double-directional radio channel characterization for urban macrocellular applications,” *IEEE Trans. Antennas and Propag.*, vol. 51, no. 11, pp. 3122–3133, November 2003.

[18] D. M. Pozar, *Microwave Engineering*. Addison-Wesley, 1990.

[19] P. J. Meier, J. A. Calviello, and P. R. Bie, “Wide-band subharmonically pumbed W-band mixer in single-ridge fin-line,” *IEEE Trans. Microwave Theory and Tech.*, vol. 30, no. 12, pp. 2184–2189, December 1982.

[20] S. Raman and G. M. Rebeiz, “A 94 GHz uniplanar subharmonic mixer,” *IEEE MTT-S International Microwave Symposium Digest*, vol. 1, pp. 385–388, June 1996.

[21] S. Raman, F. Rucky, and G. M. Rebeiz, “A high-performance W-band uniplanar subharmonic mixer,” *IEEE Trans. Microwave Theory and Tech.*, vol. 45, no. 6, pp. 955–962, June 1997.

[22] Y. L. Kok, P. Huang, W. Huei, B. R. Allen, R. Lai, M. Sholley, T. Gaier, and I. Mehdi, “120 and 60 GHz monolithic InP-based HEMT diode sub-harmonic mixer,” *IEEE MTT-S International Microwave Symposium Digest*, vol. 3, pp. 1723–1726, June 1999.

[23] I. Mehdi, S. M. Marazita, D. A. Humphrey, L. Trong-Huang, R. J. Dengler, J. E. Oswald, A. J. Pease, S. C. Martin, , W. L. Bishop, T. W. Crowe, and P. H. Siegel, “Improved 240-GHz subharmonically pumped planar Schottky diode mixers for space-borne applications,” *IEEE Trans. Microwave Theory and Tech.*, vol. 46, no. 12, pp. 2036–2042, December 1998.

[24] Y. L. Kok, H. W. R. Lai, M. Barsky, M. Sholley, and B. Allen, “A 180-GHz MMIC sub-harmonic mixer based on InGaAs/InAlAs/InP HEMT diodes,” *GaAs Integrated Circuit Symp.*, pp. 113–115, October 1999.

[25] G. P. Gauthier, J. P. Raskin, and G. M. Rebeiz, “A 140170-GHz Low-Noise Uniplanar Subharmonic Schottky Receiver,” *IEEE Trans. Microwave Theory and Tech.*, vol. 48, no. 8, pp. 1416–1419, August 2000.

[26] K. S. von Behren, D. Pienkowski, T. Mueller, M. Tempel, and G. Boeck, “77 GHz harmonic mixer with flip-chip Si-Schottky diode,” *Microwaves, Radar and Wireless Commun. (MIKON)*, vol. 3, pp. 743–746, May 2002.

[27] Y. J. Hwang, C. H. Lien, H. Wang, M. W. Sinclair, R. G. Gough, H. Kanoniuk, and T. H. Chu, “A 78114 GHz monolithic subharmonically pumped GaAs-based HEMT diode mixer,” *IEEE Microwave and Wireless Component Letters*, vol. 12, no. 6, pp. 209–211, June 2002.

[28] N. I. Dib, L. P. B. Katehi, G. E. Ponchak, and R. N. Simons, “Theoretical and experimental characterization of coplanar waveguide discontinuities for filter applications,” *IEEE Trans. Microwave Theory and Tech.*, vol. 39, no. 5, pp. 873–882, May 1991.

[29] A. K. Rayit and N. J. McEwan, “Coplanar waveguide filters,” *IEEE MTT-S International Microwave Symposium Digest*, vol. 3, pp. 1317–1320, June 1993.

[30] W. Menzel, W. Schwab, and G. Strauss, “Investigation of coupling structures for coplanar bandpass filters,” *IEEE MTT-S International Microwave Symposium Digest*, vol. 3, pp. 1407–1410, May 1995.

[31] S. D. Gedney, P. Petre, M. Matloubian, and R. T. Kihm, “Simulation and performance of passive millimeter wave coplanar waveguide circuit devices,” *IEEE Wireless Commun. Conf.*, pp. 27–31, August 1997.

[32] P. M. Watson and K. C. Gupta, “Design and optimization of CPW circuits using EM-ANN models for CPW components,” *IEEE Trans. Microwave Theory and Tech.*, vol. 45, no. 12, pp. 2515–2523, December 1997.

[33] G. E. Ponchak and L. P. B. Katehi, “Open- and short-circuit terminated series stubs in finite-width coplanar waveguide on silicon,” *IEEE Trans. Microwave Theory and Tech.*, vol. 45, no. 6, pp. 970–976, June 1997.

[34] T. Weller, “Edge-coupled coplanar waveguide bandpass filter design,” *IEEE MTT-S International Microwave Symposium Digest*, vol. 1, pp. 335–338, June 2000.

[35] T. M. Weller, “Edge-coupled coplanar waveguide bandpass filter design,” *IEEE Trans. Microwave Theory and Tech.*, vol. 48, no. 12, pp. 2453–2458, December 2000.

[36] K. Hettak, N. Dib, A. Omar, G. Y. Delisle, M. Stubbs, and S. Toutain, “A useful new class of miniature CPW shunt stubs and its impact on millimeter-wave integrated circuits,” *IEEE Trans. Microwave Theory and Tech.*, vol. 47, no. 12, pp. 2340–2349, December 1999.

[37] S. V. Robertson, L. P. B. Katehi, and G. B. Rebeiz, “Micromachined W-band filters,” *IEEE Trans. Microwave Theory and Tech.*, vol. 44, no. 4, pp. 598–606, April 1996.

[38] E. Rius, G. Prigent, H. Happy, G. Dambrine, S. Boret, and A. Cappy, “Wide- and narrow-band bandpass coplanar filters in the W-frequency band,” *IEEE Trans. Microwave Theory and Tech.*, vol. 51, no. 3, pp. 784–791, March 2003.

[39] A. Tessmann, S. Kudszus, T. Feltgen, M. Riessle, C. Sklarczyk, and W. H. Haydl, “Compact single-chip W-band FMCW radar modules for commercial high-resolution sensor applications,” *IEEE Trans. Microwave Theory and Tech.*, vol. 50, no. 12, pp. 2995–3001, December 2002.

[40] K. W. Chang, H. Wang, G. Shreve, J. G. Harrison, M. Core, A. Paxton, M. Yu, C. H. Chen, and G. S. Dow, “Forward-looking automotive radar using a W-band single-chip transceiver,” *IEEE Trans. Microwave Theory and Tech.*, vol. 43, no. 7, pp. 1659–1668, July 1995.

[41] K. Kawakami, H. Ikematsu, T. Kashiwa, K. Matsuo, Y. Isota, and O. Ishida, “A millimeter-wave pulse transmitter with a harmonic mixer,” *IEEE Microwave Conf., Asia-Pacific*, pp. 85–88, December 2000.

[42] J. K. A. Everard and K. K. M. Cheng, “High performance direct coupled bandpass filters on coplanar waveguide,” *IEEE Trans. Microwave Theory and Tech.*, vol. 41, no. 9, pp. 1568–1571, September 1993.

[43] A. Vogt and W. Jutzi, “An HTS narrow bandwidth coplanar shunt inductively coupled microwave bandpass filter on $LaAlO_3$,” *IEEE Trans. Microwave Theory and Tech.*, vol. 45, no. 4, pp. 492–497, April 1997.

[44] S. A. Maas, *Microwave mixers*. Boston: Artech House Publishers, 2003.

[45] *Agilent 8719D, 8720D, and 8722D network analyzers data sheet*. Agilent Technology.

[46] F. T. U. R. Moore and A. Fung, *Microwave Remote Sensing Active and Passive*. Norwood: Arthech House, 1982.

[47] *E4491A RF impedance/material analyzer data sheet*. Agilent Technology, 2003.

[48] *HP 85071E material measurement software, technical overview*. Agilent Technology, 2003.

[49] J. B. Keller, “Geometrical theory of diffraction,” *J. Opt. Soc. Amer.*, vol. 52, p. 116130, 1962.

[50] R. G. Kouyoumjian and P. H. Pathak, “A uniform geometrical theory of diffraction for an edge in a perfectly conducting surface,” *IEE Proceedings*, vol. 62, p. 14481461, November 1974.

[51] W. D. Burnside and K. Burgener, “High frequency scattering by thin lossless dielectric slab,” *IEEE Trans. Antennas and Propag.*, vol. 31, no. 1, p. 104110, January 1983.

[52] R. J. Luebbers, “Finite conductivity unifrom GTD versus knife edge diffraction in prediction of propagation path loss,” *IEEE Trans. Antennas and Propag.*, vol. 32, no. 1, pp. 70–76, January 1984.

[53] ——, “Propagation prediction for hilly terrain using GTD wedge diffraction,” *IEEE Trans. Antennas and Propag.*, vol. 32, no. 9, p. 951955, September 1984.

[54] ——, “Comparison of lossy wedge diffraction coefficients with application to mixed path propagation loss prediction,” *IEEE Trans. Antennas and Propag.*, vol. 36, no. 7, p. 10311034, July 1988.

[55] W. Zhang, “A wide-band propagation model based on UTD for cellular mobile radio communications,” *IEEE Trans. Antennas and Propag.*, vol. 45, no. 11, pp. 1669–1678, November 1997.

[56] P. L. Perini and C. Holloway, “Angle and space diversity comparisons in different mobile radio environments,” *IEEE Trans. Antennas and Propag.*, vol. 46, no. 6, pp. 764–775, June 1998.

[57] J. T. Hviid, J. B. Andersen, J. Toftgard, and J. Bojer, “Terrain-based propagation model for rural area-an integral equation approach,” *IEEE Trans. Antennas and Propag.*, vol. 43, no. 1, pp. 41–46, January 1995.

[58] S. R. Broadstone and R. M. Arthur, “Determination of time-of-flight surfaces using the method of moments,” *IEEE Trans. Medical Imaging*, vol. 10, no. 2, pp. 173–179, June 1991.

[59] D. G. Beetner and R. M. Arthur, “Generation of synthetic focus images from pulse echo ultrasound using difference equations,” *IEEE Trans. Medical Imaging*, vol. 15, no. 5, pp. 665–672, October 1996.

[60] M. Xu and L. V. Wang, “Time domain reconstruction for thermoacoustic tomography in a spherical geometry,” *IEEE Trans. Medical Imaging*, vol. 21, no. 7, pp. 814–822, July 2002.

[61] F. Aryanfar, I. Koh, and K. Sarabandi, “Physics based ray-tracing propagation model for sub urban areas,” *IEEE Antennas and Propag. Sypm.*, vol. 4, pp. 903–906, June 2003.

[62] D. F. Williams and S. E. Schwarz, “Design and performance of coplanar waveguide bandpass filters,” *IEEE Trans. Microwave Theory and Tech.*, vol. 31, no. 7, pp. 558–566, July 1983.

[63] K. Yoshida, K. Sashiyama, S. Nishioka, H. Shimakage, and Z. Wang, “Design and performance of miniaturized superconducting coplanar waveguide filters,” vol. 9, no. 2, pp. 3905–3908, June 1999.

[64] H. Kanaya, T. Shinto, K. Yoshida, T. Uchiyama, and Z. Wang, “Miniaturized HTS coplanar waveguide bandpass filters with highly packed meanderlines,” vol. 11, no. 1, pp. 481–484, March 2001.

[65] Y.-K. Kuo, C.-H. Wang, and C. H. Chen, “Novel reduced-size coplanar-waveguide bandpass filters,” *IEEE Microwave and Wireless Component Letters*, vol. 11, no. 2, pp. 65–67, February 2001.

[66] F. L. Lin, C. W. Chiu, and R. B. Wu, “Coplanar waveguide bandpass filter- a ribbon-of-brick-wall design,” *IEEE Trans. Microwave Theory and Tech.*, vol. 43, no. 7, pp. 1589–1596, July 1995.

[67] D. F. Williams, “On-Wafer measurement at millimeter wave frequencies,” *IEEE MTT-S International Microwave Symposium Digest*, vol. 3, pp. 1683–1686, June 1996.